To the Graduate Council:
I am submitting herewith a dissertation written by Su-Ann Chong entitled "A High Rate Pixelated Neutron Detector for Neutron Reflectometry at the Spallation Neutron Source." I have examined the final paper copy of this dissertation for form and content and recommend that it be accepted in partial fulfillment of the requirements for the degree of Doctor of Philosophy, with a major in Nuclear Engineering.

Jason P. Hayward, Major Professor

We have read this dissertation
and recommend its acceptance:

Richard Riedel

Lawrence Heilbronn

Nicole McFarlane

Accepted for the Council:

Dixie L. Thompson

Vice Provost and Dean of the Graduate School

A High Rate Pixelated Neutron Detector for Neutron Reflectometry at the Spallation Neutron Source

A Dissertation Presented for the

Doctor of Philosophy

Degree

The University of Tennessee, Knoxville

Su-Ann Chong

May 2022

© by Su-Ann Chong, 2022
All Rights Reserved.

Acknowledgements

I would like to thank my dissertation committee, which includes Dr. Jason Hayward, Dr. Richard Riedel, Dr. Lawrence Heilbronn and Dr. Nicole McFarlane for the support they have provided me throughout my graduate studies.

I am immensely grateful to my research advisor, Dr. Richard Riedel, for his consistent support, insightful discussions and valuable guidance over the last five years. His incredible breadth of knowledge and experiences meant that I was always learning, and it has genuinely been a great pleasure and honor working with him on this project.

I owe my special thanks to the dedicated support of the Detector Group at the Spallation Neutron Source, Oak Ridge National Laboratory: Bruce Hannan, Cornelius Donahue, Theodore Visscher, Christopher Montcalm, Justin Beal, Loren Funk, Dr. Yacouba Diawara and Kevin Berry. They have always been there for me during the highs and lows of my graduate studies: they were there to celebrate every little milestone I achieved and encouraged me when I had my moments of doubt.

I would like to express my gratitude to Dr. Jason Hayward for serving as my academic advisor for my Ph.D. degree, and for being so caring, supportive and responsive throughout the entire process, especially during the challenging times of a global pandemic. I would also like to thank Dr. Xianfei Wen for his valuable feedback and insightful discussion about my project.

None of this would have been possible without the unconditional love and unwavering support from my family, my close friends and my significant other.

This work is supported by the U.S. Department of Energy, Office of Sciences, Office of Basic Energy Sciences under Contract Numbers DE-AC05-00OR22725 and DE- SC0022292.

Abstract

This work presents the development of a high-rate ^{6}Li-based pixelated neutron detector for neutron reflectometry instruments at the Spallation Neutron Source (SNS), Oak Ridge National Laboratory. The current detector technology falls short on the instrument requirements, particularly on the counting rate capability. This detector was designed specifically to overcome the limitation in counting rate by having a fully pixelated design from neutron conversion layer to photodetector and readout system. For the neutron converting layer, a ^{6}Li-based neutron scintillator was used. Each scintillator element was coupled to a photodetector, in this case a silicon photomultiplier (SiPM). The output of each SiPM was read out independently. This design has been demonstrated to have a significantly higher rate capability compared to other charge-sharing designs due to the fact that each pixel is fully functional on its own, without relying on adjacent pixels. An experimental prototype was constructed and characterized using various standardized tests such as counting rate, neutron detection efficiency, spatial resolution, γ sensitivity, crosstalk and uniformity. Lastly, neutron reflectivity experiments were conducted using the detector prototype to demonstrate the performance and capability of the detector in practice.

Table of Contents

1 Introduction **1**

1.1 Spallation Neutron Source 1

1.1.1 How SNS works 1

1.1.2 Spallation Source vs Reactor Source 3

1.2 Neutron Scattering 5

1.2.1 Advantages of Neutron Scattering 5

1.2.2 Theory of Neutron Scattering 9

1.3 Neutron Reflectometry 12

1.3.1 Theory of Neutron Reflectometry 12

1.3.2 Reflectivity Experiment 17

1.3.3 Application of Neutron Reflectometry 17

1.4 Motivation 19

1.4.1 Limitation of Current Detectors 19

1.4.2 Instrument Requirements 21

1.5 Prior Similar Work 23

1.5.1 ^{10}B-based Detectors 23

1.5.2 ^{6}Li-based Detectors 25

1.6 Original Contributions 25

2 Detector Design and Construction **29**

2.1 Overview of Scintillator Detectors 29

2.1.1 Scintillators 29

2.1.2 Silicon Photomultipliers . . . 30
2.2 First Detector Prototype . . . 35
2.2.1 Neutron Scintillator . . . 35
2.2.2 Silicon Photomultiplier . . . 39
2.2.3 Readout Electronics . . . 43
2.2.4 Full Assembly . . . 47
2.3 Second Detector Prototype . . . 51
2.3.1 Major Changes Implemented . . . 51
2.3.2 Silicon Photomultiplier . . . 53
2.3.3 Readout Electronics . . . 53
2.3.4 Full Detector Assembly and Operational Settings . . . 58

3 Detector Characterization **66**
3.1 First Detector Prototype . . . 66
3.1.1 Neutron Detection Efficiency . . . 66
3.1.2 Counting Rate and Linearity . . . 67
3.1.3 Crosstalk . . . 68
3.1.4 Spatial Resolution and Uniformity . . . 70
3.1.5 Gamma Sensitivity . . . 72
3.1.6 Summary . . . 74
3.2 Second Detector Prototype . . . 76
3.2.1 Neutron Detection Efficiency . . . 78
3.2.2 Counting Rate and Linearity . . . 78
3.2.3 Crosstalk . . . 80
3.2.4 Spatial Resolution . . . 80
3.2.5 Gamma Sensitivity . . . 84
3.2.6 Summary . . . 84

4 Neutron Reflectivity Experiment **87**
4.1 Counting Rate Test . . . 87

4.1.1 Experimental Setup and Procedure . . . 87
4.1.2 Results and Analysis . . . 89
4.1.3 Conclusion . . . 91
4.2 Neutron Reflectivity Experiment . . . 91
4.2.1 Experimental Setup and Procedure . . . 94
4.2.2 Data Acquisition and Reflectivity Analysis . . . 94
4.2.3 Results and Discussion . . . 99

5 Summary and Conclusion 107
5.1 Summary of Research Findings . . . 108
5.2 Recommendations for Future Work . . . 110

Bibliography 112

Appendix 124

A Printed Circuit Board (PCB) 125
A.1 KiCAD electronic design automation software . . . 125
A.2 Mounting Board for First Detector Prototype . . . 126
A.3 Custom FEB/S for Second Detector Prototype . . . 129

B Time-of-Flight (ToF) Measurements from Reflectivity Experiment 134

Vita 143

List of Tables

1.1 Components of a neutron scattering instrument [66] 4
1.2 Basic properties of neutrons [12, 78]. 6
1.3 Detector requirement for the reflectometry instruments at the First Target Station of the Spallation Neutron Source (FTS-SNS) 22
1.4 Detector requirement for next-generation neutron reflectometry at the Second Target Station of the Spallation Neutron Source (STS-SNS) [27, 23] 22
1.5 Isotopes suitable for neutron detection and their thermal neutron capture/fission reactions. 24
1.6 Operating parameters for detectors currently used at SNS first target station [27]. 26

2.1 Characteristics of a scintillator [31]. 31
2.2 Characteristics of SiPMs [61] 34
2.3 GS20 properties [72] 36
2.4 Characteristics of SensL SiPM (ArrayC-10035064P-BGA). Values are quoted for 1 mm sensor size, microcell size of 35 μm and overvoltage of 2.5 V [54]. 40
2.5 Characteristics of Hamamatsu S13361-2050AE-08 MPPC [60]. 55
2.6 Differences in specification between SensL ArrayC-10035064P-BGA SiPM (shortened as SensL SiPM) and Hamamatsu S13361-2050AE-08 MPPC array (shortened as Hamamatsu MPPC) [54, 60]. 55

2.7 Changes made in the second detector prototype 65

3.1 Summarized result for performance evaluation of first detector prototype. 77
3.2 Summarized result for performance evaluation of first and second detector prototype. 86

4.1 These 7 instrument configurations were used in the direct beam measurements at SNS BL-4B. 95
4.2 These 7 instrument configurations were used in the reflected beam measurements at SNS BL-4B. 95
4.3 Layer model for the iridium sample. 101
4.4 Layer model for the quartz sample. 101
4.5 The thickness, SLD, roughness and χ^2 goodness of fit for the quartz sample 106
4.6 The thickness, SLD, roughness and χ^2 goodness of fit for the iridium sample 106

5.1 Comparison between the performance of detector prototypes and instrument requirements. 109

List of Figures

1.1 The layout of SNS consists of an ion source, a linear accelerator, an accumulator ring, a target and an instrument hall [73]. 2

1.2 SNS neutron scattering instrument hall layout [73]. 4

1.3 A plot of peak neutron brightness vs average neutron brightness for neutron sources around the world. 6

1.4 A plot of neutron brightness as a function of time for SNS and HFIR. 7

1.5 Illustration of the Bragg's Law. 11

1.6 Reflection on an infinite planar surface [14]. 13

1.7 Reflectivity curve of a homogenous substrate (Si) with a single interface. 16

1.8 Reflectivity curve of a Fe thin film on a Si substrate with two interfaces. 16

1.9 Typical setup for horizontal neutron reflectometer [53]. 18

2.1 Scintillation mechanism: conversion, energy transfer and luminescence. 31

2.2 (a) A typical structure of a SiPM (b) All of the microcells are connected in parallel, and each SiPM has an anode and a cathode [61]. 32

2.3 Photoluminescence spectrum of GS20 scintillator glass for optical excitation wavelengths in 325 - 400 nm range [29] 36

2.4 The area of high intensity are presumably neutron events and any other surrounding data points are unwanted events from noise and γ-rays. . 37

2.5 (a) Irradiation of γ-rays shows a linear response from γ events and a constant response from noise (b) Irradiation of both neutrons and γ-rays shows a combination of linear response from gamma events, a constant response from noise in addition to the neutron events. 38
2.6 A plot of photon detection efficiency (PDE) versus wavelength, with a peak wavelength at 420 nm [54]. 40
2.7 (a) PDE versus overvoltage (b) Gain versus overvoltage (c) Dark current versus voltage. The voltage used for our detection system is 27.5 V, including an overvoltage of 3.0 V [54]. 41
2.8 (a) An 8×8 array of SiPM with a pitch of 2 mm (b) Magnified view of the sensor elements with an active area of 1 mm $\times$ 1 mm. [54]. . . 42
2.9 Signal flow diagram in FPGA-based data acquisition system. FPGA is interposed between the input and the output, such as analog-to-digital converters (ADCs), digital-to-analog converters (DACs), and the communication bus with the host. 44
2.10 Photos of (a) front view and (b) back view of the AVNET MicroZed development board [5]. 45
2.11 This GUI is the interface allows users to specify input parameters to the FPGA and obtain real time results on the detector. 46
2.12 Photos of (a) an array of Scintillator cubes and (b) a single cube with dimensions added. 48
2.13 SiPM array with the associated electronics. 49
2.14 Photos of (a) back view, (b) front view and (c) side view of our detector prototype. 50
2.15 Characteristics of Hamamatsu MPPC [60]. 54
2.16 The PETsys TOFPET2 ASIC evaluation kit consists of two FEM128, one FEB/D board, firmware and software [20]. 56

2.17 PETsys FEB/D consists of a communication mezzanine (in blue), a bias voltage mezzanine (in red) and data acquisition board equipped with Kintex7 FPGA (in green) [21]. 57
2.18 PETsys graphical user interface for data acquisition controls [21] . . . 57
2.19 Photos show (a) the front view and (b) the side view of the scintillator array. 59
2.20 (a) A customized aluminum fixture is used to center each scintillator element to each SiPM and hold them in place. (b) A zoom-in view of the pixel shows that the scintillator elements are centered at each individual SiPM. 60
2.21 Photos show (a) the front view and (b) the side view of the custom sensor array designed to connect four 8×8 Hamamatsu S13361-2050AE-08 SiPM arrays to the PETsys SiPM readout system. 62
2.22 Photos show (a) the exterior and (b) the interior of the complete detector assembly. 63

3.1 (a) Counting rate test at PSD, MURR (b) Counting rate test at CG-1A. HFIR. 69
3.2 Crosstalk measurement results over pixel (a) 28 (b) 29 (c) 36 (d)37. 71
3.3 Simulated result versus experimental result for linear scan measurement 73
3.4 Time-over-Threshold spectrum of neutron peak and gamma peak obtained using (a) 1 mm SiPM (b) 6 mm SiPM. 75
3.5 Plot of the count rate of the pixelated detector as a function of attenuator thickness. The equation of fit is $y = 221.51\ e^{-0.39x}$, and the $R^2 = 0.9997$. 79
3.6 Crosstalk measurement over pixel 170. 81
3.7 (a) The 2-D histogram and (b) cross-sectional profile of the measurements when a 1.5 mm slit was positioned at the center of a pixel. 82

3.8 (a) The 2-D histogram and (b) cross-sectional profile of the measurements when a 1.5 mm slit was positioned slightly off the center of a pixel. 83

4.1 The pixelated neutron detector installed at the Liquid Reflectometer (BL-4B) for a neutron reflectivity experiment. 88

4.2 The graph shows the time-averaged count rate of the pixelated detector is plotted against the time-averaged count rate of the beam monitor. The pixelated detector shows a linear response in increasing count rate up to the maximum available flux. The equation of fit is $y = 18.1x - 0.307$ and the R^2 of the linear fit is 0.99995. 90

4.3 The (a) Time-of-Flight (ToF) measurement and (b) the area plot of the detector count rate for the highest neutron flux setting. 92

4.4 The quartz sample at the sample stage. 93

4.5 (a) Unshifted and (b) shifted ToF spectrum for a direct beam measurement (run #5). 96

4.6 The data collected during acquisition includes (a) the time-of-flight (ToF) measurement, (b) the area plot and (c) the cross-section profile of the detector count rate. 98

4.7 Plots show the reflectivity curves for (a) iridium and (b) quartz samples using the pixelated detector. 100

4.8 Plots show the reflectivity curves for iridium samples using (a) the pixelated detector and (b) MWPC. 103

4.9 Plots show the reflectivity curves for quartz samples using (a) the pixelated detector and (b) MWPC. 104

4.10 Plots show the scattering length density profile for (a) iridium and (b) quartz samples using both the pixelated detector and MWPC. 105

A.1 (a) Schematic and (b) PCB layout of the SiPM mounting board for the first detector prototype. 127

A.2 (a) Front view and (b) back view of the SiPM mounting board generated using the KiCAD 3D viewer. 128
A.3 Schematic and PCB layout of the custom FEB/S (direct connection) for the second detector prototype. 130
A.4 Front view and back view of the custom FEB/S (direct connection) generated using the KiCAD 3D viewer. 131
A.5 Schematic and PCB layout of the custom FEB/S (ribbon connection) for the second detector prototype. 132
A.6 Front view and back view of the custom FEB/S (ribbon connection) generated using the KiCAD 3D viewer. 133

B.1 Direct beam measurement: (a) run #1 and (b) run #2. 135
B.2 Direct beam measurement: (a) run #3 and (b) run #4. 136
B.3 Direct beam measurement: (a) run #5 and (b) run #6. 137
B.4 Direct beam measurement: run #7. 138
B.5 Reflected beam measurement (iridium sample): (a) run #1 and (b) run #2. 139
B.6 Reflected beam measurement (iridium sample): (a) run #3 and (b) run #4. 140
B.7 Reflected beam measurement (iridium sample): (a) run #5 and (b) run #6. 141
B.8 Reflected beam measurement (iridium sample): run #7. 142

Chapter 1

Introduction

1.1 Spallation Neutron Source

The Spallation Neutron Source (SNS) facility at Oak Ridge National Laboratory (ORNL) is a 1.4 MW accelerator-based neutron source facility that delivers short intense neutron pulses at 60 Hz [77, 46, 30]. The SNS operates as a user facility that enables researchers from all over the world to conduct a broad range of scientific research using neutron scattering techniques [46].

1.1.1 How SNS works

The SNS consists of an ion source, a linear accelerator, a proton accumulator ring, a liquid mercury target and a neutron scattering instrument hall as shown in Figure 1.1 [77].

The ion source produces negatively charged hydrogen (H^-) ions that are accelerated to an energy of 2.5 MeV [73]. The beam is then injected into a large linear accelerator (linac), which further accelerates the H^- beam from 2.5 MeV to 1 GeV. The linac consists of copper cavities and superconducting niobium cavities inside cryomodules that accelerate the ion beam [73, 15]. The intense H^- beam from the linac has a macro-pulse length of 1 ms which is chopped into a number

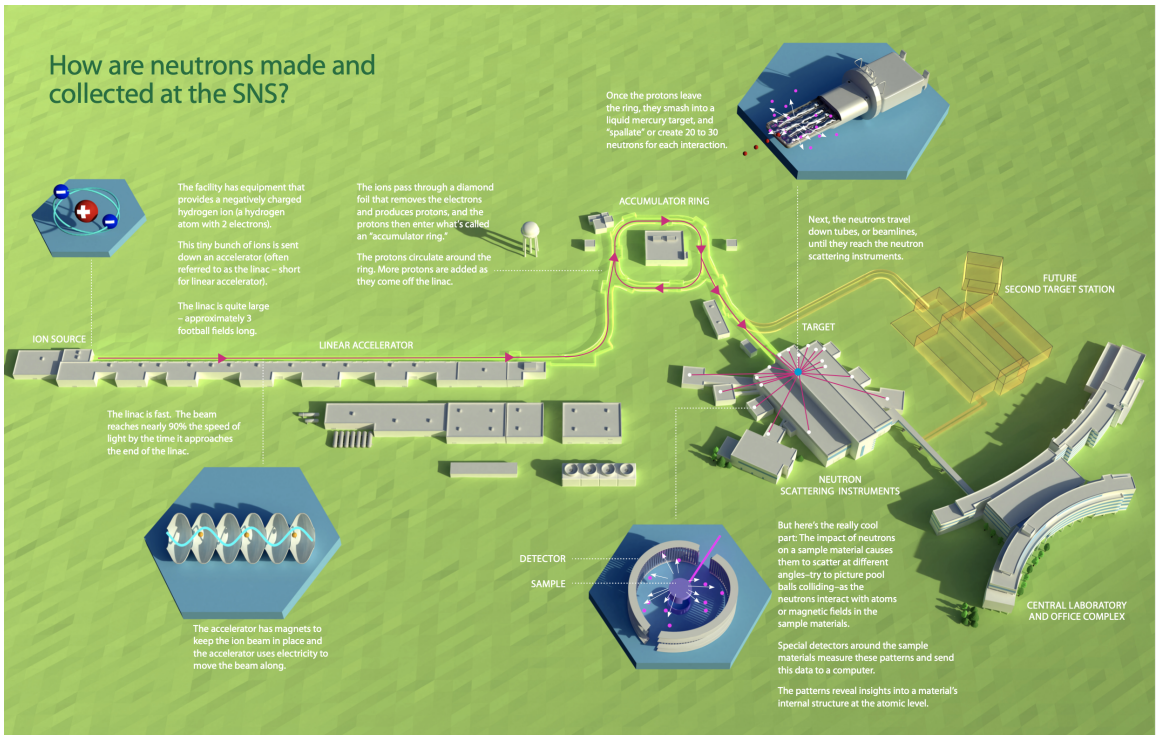


Figure 1.1: The layout of SNS consists of an ion source, a linear accelerator, an accumulator ring, a target and an instrument hall [73].

of mini-pulses and injected into the proton accumulator ring [73, 15]. The beam is wrapped into the ring through a diamond stripper foil. The diamond stripper foil strips the electrons from the H^- to produce protons (H^+) beam [73]. The short intense proton pulses produced by the proton accumulator ring are directed to a target vessel. The target vessel is a steel structure containing liquid mercury. Very intense short pulses of neutrons are produced by the process of spallation when high-energy protons impinge on the mercury target [73]. Several moderators slow these neutrons to thermal or sub-thermal energies using water or liquid hydrogen for material science research [73, 15]. These neutrons are then guided to the instrument hall where a suite of neutron scattering instruments is located [73]. The target station has 18 shutters that will be able to support 24 neutron instruments. Currently, the instrument hall has 19 state-of-the-art neutron scattering instruments in operation as shown in Figure 1.2. Typically, a neutron scattering instrument involves several components listed in Table 1.1.

1.1.2 Spallation Source vs Reactor Source

Neutron sources for neutron scattering experiments are typically based on one of the two principles: fission and spallation [45]. Traditional nuclear reactors make use of the production of neutrons for maintaining the chain reaction [45]. Excess neutrons are then utilized for neutron scattering. Spallation neutron sources accelerate protons to the GeV regime so that the proton beam can split heavy nuclei with a large neutron surplus, creating free neutrons among the reaction products [45]. Figure 1.3 shows the comparisons between existing neutron sources and next-generation sources. Although reactor-based neutron sources generally have a higher average neutron brightness than spallation-based neutron sources, spallation-based neutron sources typically have a higher peak neutron brightness than reactor-based neutron sources. This distinction can be further illustrated in Figure 1.4 that shows the time-dependent neutron brightness profile for both reactor-based and spallation-based neutron sources where the High Flux Isotope Reactor (HFIR) is a reactor-based neutron source and

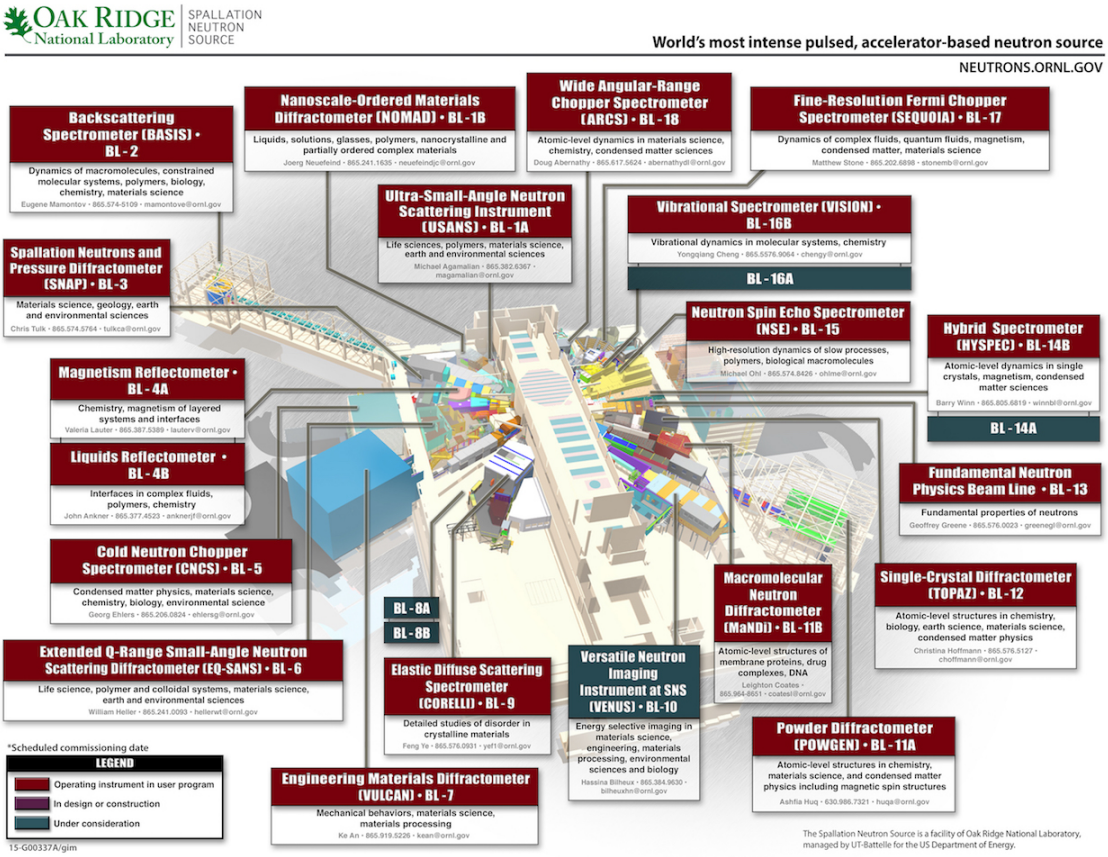


Figure 1.2: SNS neutron scattering instrument hall layout [73].

Table 1.1: Components of a neutron scattering instrument [66]

Component	Description
Monochromators	monochromate or analyze the energy of a neutron beam
Collimators	define the direction of travel of the neutron
Guides	allow neutrons to travel large distances without suffering intensity loss
Detectors	see and detect neutron events
Choppers	define a short pulse or pick out a small band of neutron energies
shielding	minimize background and radiation exposure to users

the First Target Station (FTS) of the SNS is a spallation-based neutron source. It is important to note that the rate requirement for a neutron scattering instrument at spallation-based sources depends heavily on the peak neutron brightness as opposed to the average neutron brightness because spallation-based neutron sources produce pulsed neutron beams instead of steady-state neutron beams.

1.2 Neutron Scattering

Neutron scattering is a highly efficient probe to study the dynamic and structural properties of condensed matter on the atomic level. The assets of neutron scattering lie on the intrinsic properties of neutrons as summarized in Table 1.2. Neutrons have zero charges, one-half spin and nonzero magnetic moment [24].

1.2.1 Advantages of Neutron Scattering

There are five general advantages of using neutron scattering techniques [9, 45]:

1. **Transparency:** Because neutrons are neutral in electric charge and have essentially zero electric dipoles, they can penetrate materials deeply, experiencing little to no Coulomb scattering by the electrons around the nucleus or the nucleus itself [9, 45]. Therefore, neutrons can penetrate far better than charged particles such as electrons. This allows the investigation of the interior of materials, rather than the surface layers probed by techniques such as X-ray scattering, electron microscopy or optical methods [45].

2. **Magnetism:** Neutrons also can reveal the microscopic magnetic structure and dynamics of material via magnetic scattering due to their non-zero magnetic moment. The magnetic moment of neutrons (due to having a spin of $\frac{1}{2}$) can couple directly to spatial and temporal variations of the magnetization of the material on an atomic scale [45].

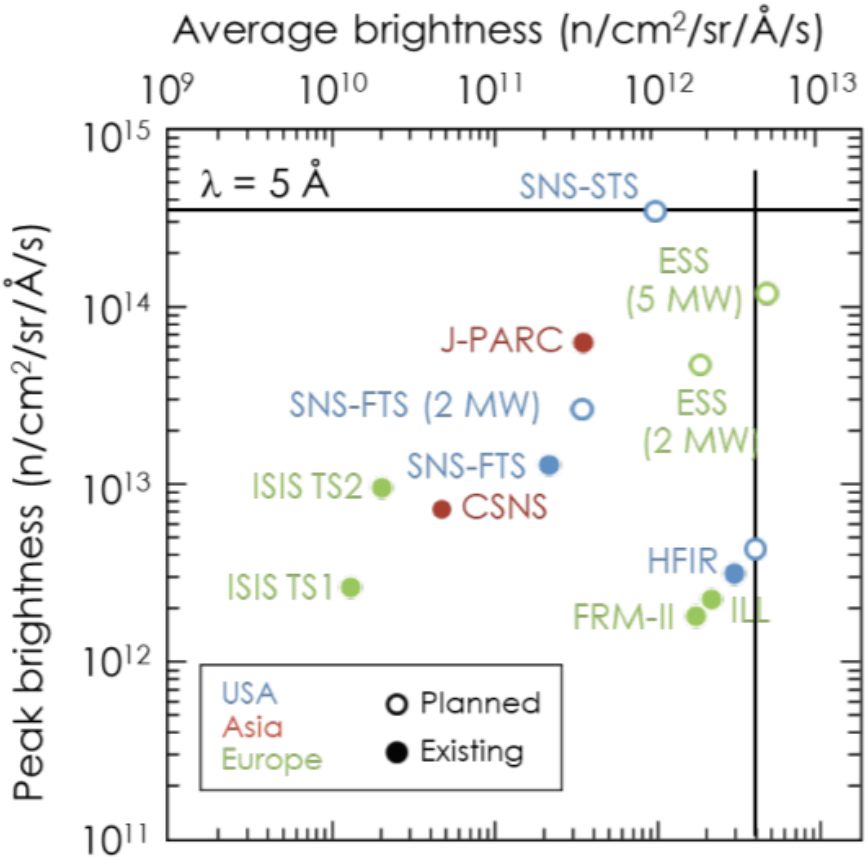


Figure 1.3: A plot of peak neutron brightness vs average neutron brightness for neutron sources around the world.

Table 1.2: Basic properties of neutrons [12, 78].

charge	mass (kg)	lifetime (s)	magnetic moment, μ_n (J/T)	gyromagnetic ratio, γ_n (s^{-1}/T)	g-factor g_n
0	1.67492×10^{-27}	882 ± 2	-0.96623×10^{-26}	-1.83246×10^{8}	3.82609

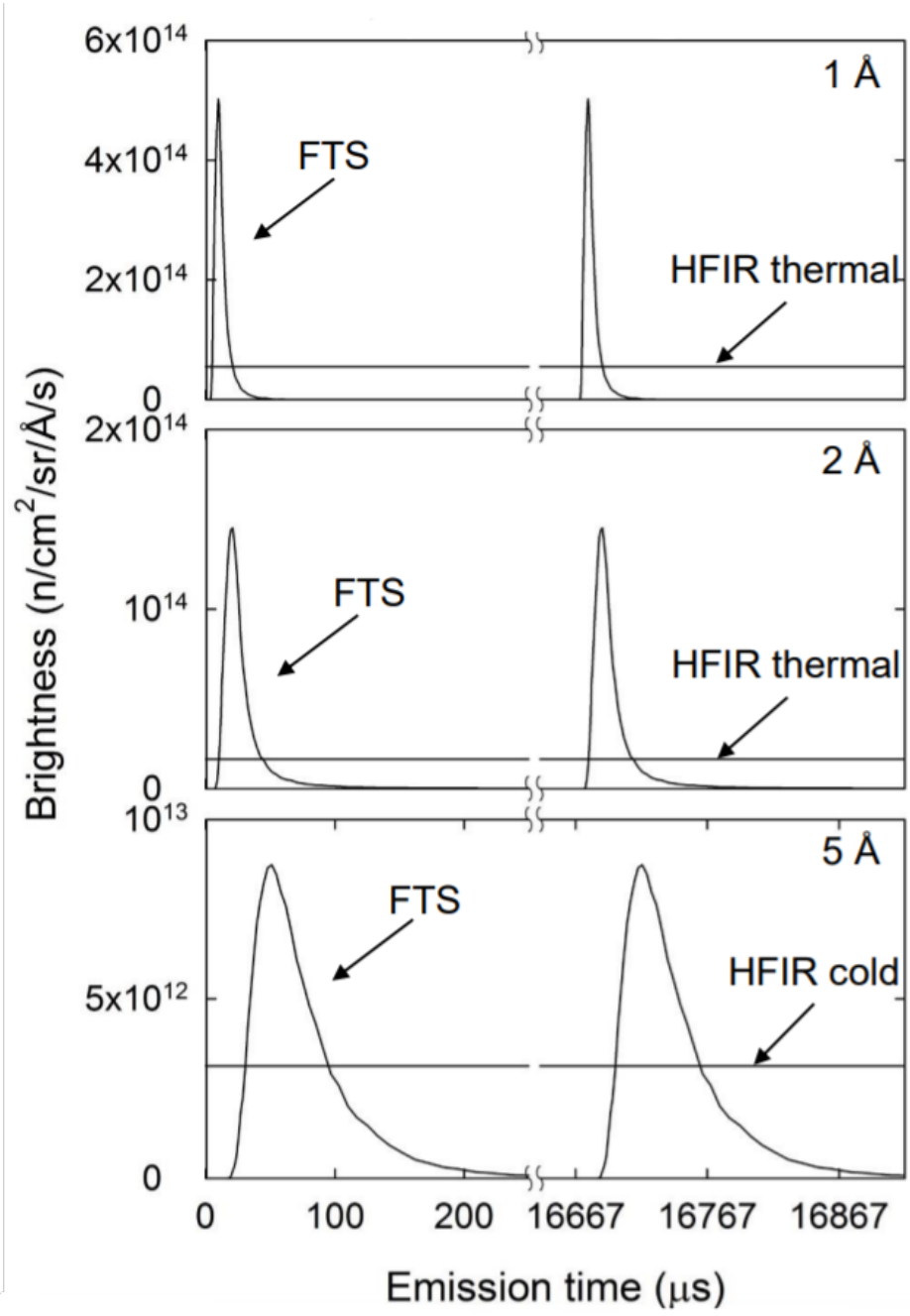


Figure 1.4: A plot of neutron brightness as a function of time for SNS and HFIR.

3. **Isotopes and light elements:** Neutron scattering length varies wildly with the atomic number Z and mass number A. The strength of the interaction of the neutron-nucleus system is defined by the scattering length, b [24]. Neutron scattering length is a quantity that depends on the details of the nuclear interaction [24]. It is related to neutron cross-section, σ as follows:

$$\sigma = 4\pi b^2 \tag{1.1}$$

Techniques such as x-ray scattering and electron microscopy have a higher sensitivity to materials that have a higher atomic number (e.g. Pb), hence they are usually less sensitive or insensitive to low Z material (e.g. H) [66]. However, neutron scattering is more sensitive to low Z materials instead of high Z materials. Moreover, neutrons are also sensitive to materials with different A but the same Z (e.g. ^{1}H and ^{2}H), making neutron scattering have isotopic sensitivity [66]. For example, neutrons have a negative neutron scattering length for ^{1}H, but have a positive neutron scattering length for ^{2}H [66]. The isotopic sensitivity of neutron allows for contrast variation, which is a labeling technique using isotopic substitution [66].

4. **Energy and wavelength:** Neutrons used in scattering experiments are typically in the range of cold neutrons and thermal neutrons. Thermal neutrons have a wavelength of around 1.8 Å. Such wavelength is a distance comparable to interatomic spacings in solids and dense fluids, making neutrons suited for studies of the atomic structure of condensed matter [24]. Additionally, thermal neutrons have an energy of around 25 meV, which is similar to elementary excitations in solids. Therefore, information on the structure and dynamics of materials can be obtained [45].

5. **Quantitative experiments:** Neutron scattering data can be used to compare to theoretical models with high precision as neutrons interact with matters

rather weakly and weak interaction with matter also diminishes higher-order effects [45].

Neutron scattering techniques are often complementary to other scattering techniques such as x-ray scattering, electron microscopy and nuclear magnetic resonance since the nature of the interactions between the probe and the sample are different. In general, neutrons interact more strongly with nuclei whereas x-rays and electrons interact more readily with the electrons in matter. Therefore, in many cases, neutron scattering when coupled with the other scattering techniques can help to understand the full range of structures and dynamics of condensed matter.

1.2.2 Theory of Neutron Scattering

Neutrons exhibit particle-wave duality [45]. In neutron scattering experiments, neutrons behave like particles in a nuclear process but act as interfering waves when they are scattered. The wave nature of a neutron allows the kinetic energy, E_n, of a neutron to be expressed in *de Broglie* wavelength, λ_n or wavevector, k_n. It can also be expressed in terms of the temperature of the moderating medium, T [78, 45]:

$$E_n = \frac{1}{2} m_n v_n^2 = \frac{h^2}{2 m_n \lambda_n^2} = \frac{\hbar^2 k_n^2}{2 m_n} = k_B T \tag{1.2}$$

where h is Planck's constant, m_n is the mass of a neutron, and k_B is Boltzmann's constant [24]. The neutron wavelength and its wave vector are usually measured in Å and Å^{-1}. Rewriting Equation 1.2 in a more practical fashion [78]:

$$E_n = 5.22704 \times 10^{-6}\ v_n^2 = 2.07212\ k_n^2 = \frac{81.8042}{\lambda_n^2} \tag{1.3}$$

where E_n is in meV, v_n in m/s, k_n in Å^{-1}, and λ_n in Å. Neutron scattering is described by conservation of momentum and energy between the incident and scattered neutron and the scattering object:

$$
\begin{aligned}
\boldsymbol{Q} &= \boldsymbol{k_i} - \boldsymbol{k_f} \\
Q &= ||\boldsymbol{k_i} - \boldsymbol{k_f}|| = \frac{4\pi}{\lambda} sin\ \theta \\
E &= E_{\eta_f} - E_{\eta_i} = \frac{\hbar^2 k_i^2}{2m_n} - \frac{\hbar^2 k_f^2}{2m_n}
\end{aligned}
\tag{1.4}
$$

where $\boldsymbol{Q}$ is the momentum transfer, E is the energy transfer and η_i and η_f are the initial and final states of the scatterer [24]. Neutrons can be scattered elastically or inelastically. Elastic neutron scattering is when the scattering of neutrons happens with no change in the energy of the incident neutron. In other words, the wave vector of the neutron changes its direction but not its magnitude [66]. One application of elastic neutron scattering is neutron diffraction, which reveals the static structure of crystalline solids, gases, liquids or amorphous materials. The basis of elastic neutron scattering is fundamentally the same as elastic x-ray scattering. It obeys Bragg's law [66].

$$
n\lambda_n = 2d\ sin\theta \tag{1.5}
$$

where n is the diffraction order, d is the interatomic spacing and θ is the angle measured from the surface normal. Bragg's law is illustrated in Figure 1.5. The diffraction pattern of scattered neutrons unveils the structural information about the material.

Inelastic neutron scattering happens when there is an exchange of energy and momentum between the incident neutron and sample, which causes both the direction and the magnitude of the wave vector to change [66]. The energy transfer of the scattered neutrons reveals the fundamental dynamics of atoms and molecules. When a neutron is scattered by a crystalline solid, it can absorb or emit an amount of energy equal to a quantum of phonon energy, $h\nu$ [78]. Most solids have phonon energies of a few meV. Because neutrons and phonons have energies in the meV range, scattering by a phonon can cause a significant change in neutron energy, thereby allowing for an accurate measurement of phonon frequencies [78]. One application of inelastic

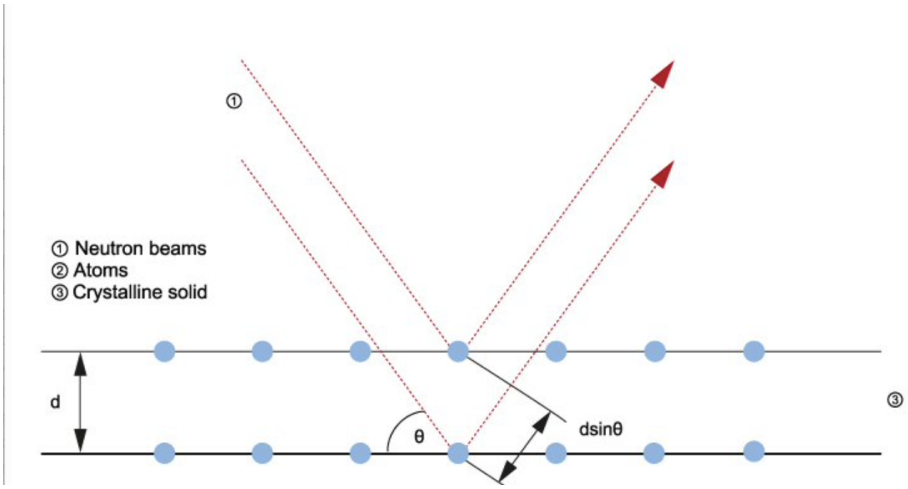


Figure 1.5: Illustration of the Bragg's Law.

neutron scattering is spectroscopy where the energy of the neutron is analyzed to study the dynamical motions of atoms and molecules. Studies of vibrational motion in atoms and molecules include diffusional motions of atoms, rotational modes of molecules, magnetic and quantum excitation or structural changes that occur during a phase transition [78].

1.3 Neutron Reflectometry

Neutron reflectometry (NREF) is a powerful neutron diffraction technique that probes the structures of surfaces and thin films. It enables the measurements of the neutron scattering length density profile (SLD) perpendicular to the plane of a surface or an interface [14]. The SLD provides information on the thickness and the chemical composition of one or several thin layers at a surface or an interface. As discussed in the previous section, neutrons can penetrate deeply into matter because neutrons only weakly interact with matter. It may seem counterintuitive for neutrons to be sensitive to surfaces or interfacial structures. However, neutrons are in fact sensitive to surfaces and interfacial structures when they impinge on the surface at sufficiently low glancing angles. For smooth surfaces, a perfect reflection of neutrons occurs at glancing angles less than a critical angle [66].

1.3.1 Theory of Neutron Reflectometry

The reflection of neutrons follows the same fundamental principle as the reflection of light, as shown in Figure 1.6, except with different refractive indices [17].

$$\theta_{incident} = \theta_{reflected} \tag{1.6}$$

Figure 1.6 shows a neutron beam reflecting at a flat surface with an incident angle θ with respect to the plane at depth $z = 0$ [14].

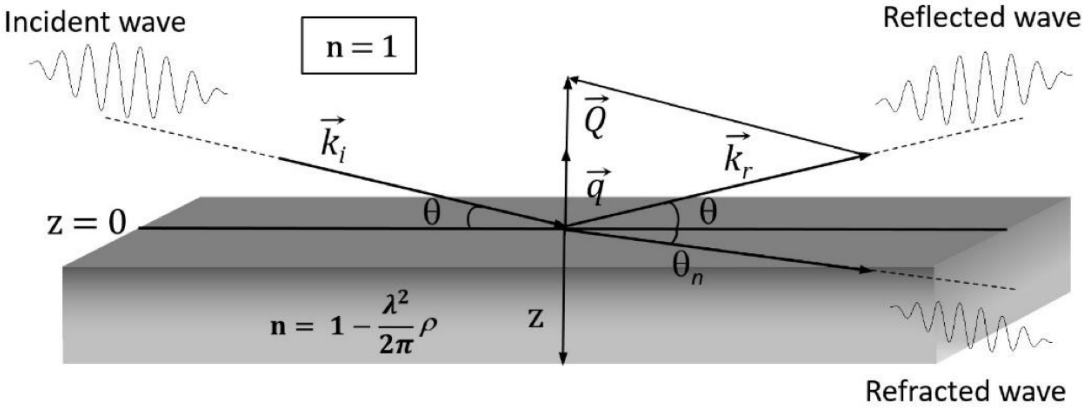


Figure 1.6: Reflection on an infinite planar surface [14].

$$k_t^2 = k_i^2 - 4\pi Nb \tag{1.7}$$

where k_t is the wave vector of the transmitted neutron, k_i is the wave vector of the incident neutron, N is the number of atoms per volume unit and b is the neutron scattering length. To express the refractive index n of a medium, we need to define the ratio of wave vectors in material and in a vacuum [14, 58]:

$$n^2 = \frac{k_t^2}{k_i^2} = 1 - \frac{\lambda^2}{\pi} Nb \tag{1.8}$$

Since the neutron refractive index is always very close to 1, therefore reflection for neutrons can only occur at very grazing angles (on the order of 1^o). Since n is very close to 1, Equation 1.8 can be approximated as Equation 1.9 where $\rho = Nb$ is the neutron scattering length density [14].

$$n \approx 1 - \frac{\lambda^2}{2\pi} \rho \tag{1.9}$$

The refraction of neutrons is described by the Snell-Descartes law [14, 57]:

$$cos\ \theta = n\ cos\ \theta_n \tag{1.10}$$

where the θ and θ_n are depicted in Figure 1.6. The critical angle for total reflection θ_c ($\theta_n = 0$) is defined as [14, 57]:

$$cos\ \theta_c = n \tag{1.11}$$

In the event when $n > 1$, total reflection cannot occur. Plugging Equation 1.8 into Equation 1.11, the critical angle becomes [14]:

$$sin\ \theta_c = \sqrt{\frac{\rho}{\pi}} \lambda \tag{1.12}$$

The reflectivity is a function of the scattering vector Q defined by Equation 1.4 [14]. The reflection coefficient R is the ratio of the intensity of the reflected beam, B to the intensity of the incident beam A. The reflection coefficient can also be expressed in terms of the project of the scattering vector on z, $\boldsymbol{q} = \boldsymbol{Q}/2$ [17, 58].

$$R = \frac{|B|^2}{|A|^2} = \left| \frac{1 - \left(1 - \left(\frac{q_c}{q}\right)^2\right)^{1/2}}{1 + \left(1 - \left(\frac{q_c}{q}\right)^2\right)^{1/2}} \right|^2 \tag{1.13}$$

where q_c and q are obtained from:

$$q_c = \sqrt{16\pi\rho} \qquad q = 2k_i sin\ \theta_i \tag{1.14}$$

q_c is the critical scattering vector. Total reflection occurs below q_c and partial reflection occurs above q_c. When $q >> q_c$, this reduces to the reflectivity used in the Born approximation [17].

$$R \approx \frac{16\pi^2}{q^4}\rho^2 \tag{1.15}$$

By recursively using Equation 1.13, the whole reflectivity of the system can be calculated. This method is described by Parratt [56]. Another method is described by Born [10] and Wolf from the work of Abelès [1]. Both methods are identical mathematically.

Figure 1.7 shows the reflectivity curve of a homogeneous silicon substrate. When the interface between two layers is smooth, there is a sharp discontinuity of SLD at the critical scattering angle q_c when passing from one layer to another. In practice, interfaces are never so abrupt because of roughness and/or inter-diffusion [14]. Figure 1.8 shows the reflectivity curve of a thin layer of iron on a silicon substrate. The two reflected waves from iron and silicon interfere with one another and form interference fringes. The interference fringes are also known as Kiessig fringes. The fringes spacing is related to the thickness of the layer as follows:

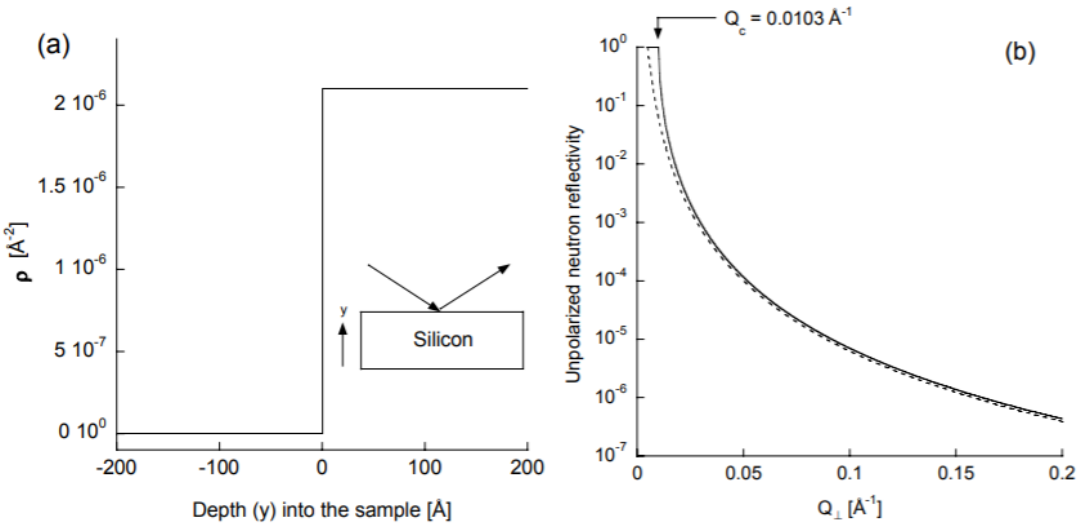


Figure 1.7: Reflectivity curve of a homogenous substrate (Si) with a single interface.

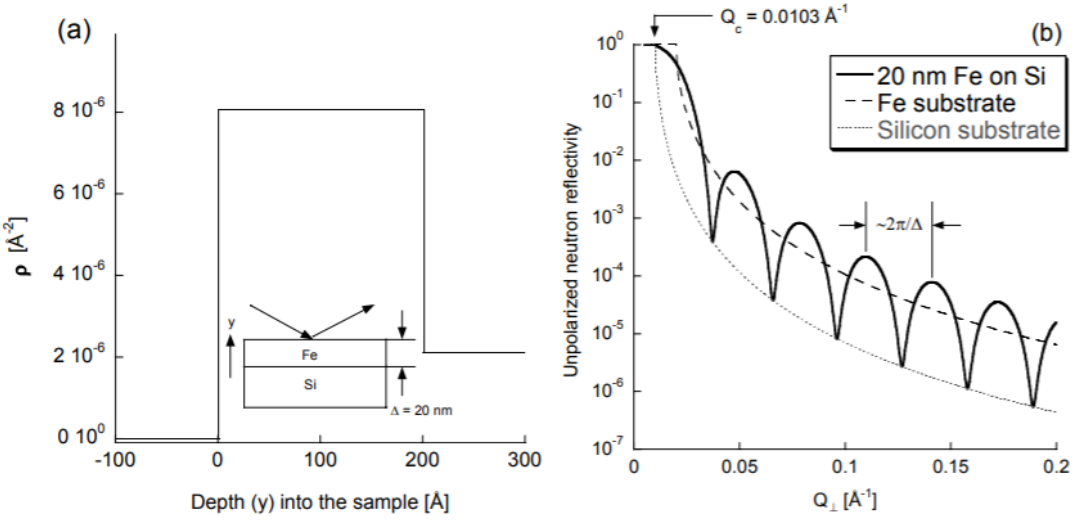


Figure 1.8: Reflectivity curve of a Fe thin film on a Si substrate with two interfaces.

$$\Delta q = \frac{2\pi}{d} \tag{1.16}$$

1.3.2 Reflectivity Experiment

The typical setup for a (horizontal) neutron reflectometer is shown in Figure 1.9.

There are two ways to measure the reflectivity of a sample as a function of the scattering vector Q. It is either by varying θ at fixed λ ($\theta - 2\theta$ mode)or by varying λ at fixed θ (time-of-flight mode) [14]. For the $\theta - 2\theta$ mode, to fix λ, the neutron beam goes through a chopper, a rotating disk that has a neutron transparent window, which allows only neutrons with a specific energy bandwidth to be selected [14]. Then the neutron beam is collimated using collimation slits and sent to the sample at grazing incidence. To vary θ, the angle of the sample θ_s is rotated by θ and the angle of the detector θ_d is varied by 2θ by geometry [14]. For the time-of-flight mode, the neutron beam (white beam or beam with an energy bandwidth) is sent to the sample at a fixed θ [14]. Because neutrons travel at a finite speed, and neutron speed ν is related to wavelength λ [14]:

$$\nu = \frac{h}{m\lambda} \tag{1.17}$$

where h is the Planck constant and m is the mass of a neutron. Therefore, neutrons with different wavelengths can be separated by their speed $\nu = \frac{t}{l}$ where $t = t_d - t_0$ is the time of flight of neutron from the source (at t_0) to the detector (at t_d) and L is the distance from the source to the detector. Measurement of the reflectivity is simply taking the ratio of the reflected beam over the direct beam for every λ value.

1.3.3 Application of Neutron Reflectometry

NREF has a broad range of applications in science and technology, ranging from material science, polymers and soft matter, thin-film magnetism, chemistry and biology. For instance, in material science, NREF is often performed in in-situ

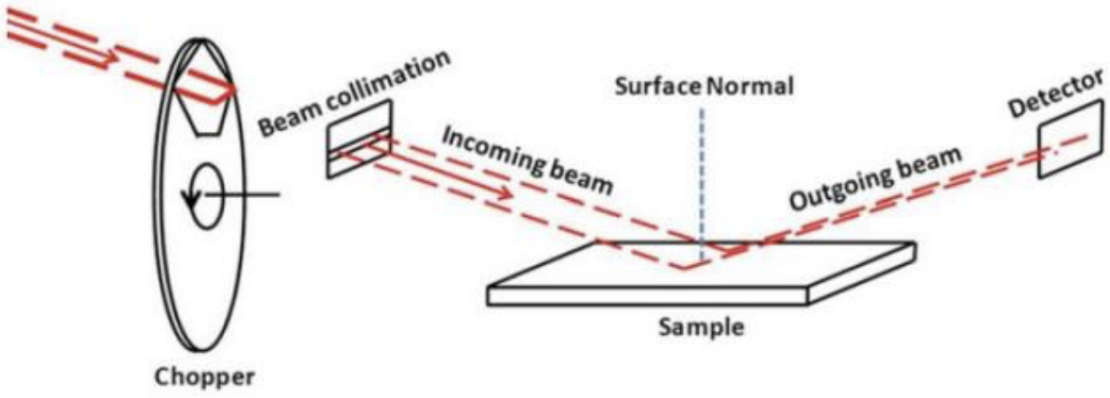


Figure 1.9: Typical setup for horizontal neutron reflectometer [53].

electrochemical experiments to study aqueous corrosion, the influence of interfacial electrical fields on the adsorption/desorption of surfactants and thin organic films, and electric charge storage devices [59]. In magnetic thin films, measurements of the magnetic depth profile using NREF at a surface and at the interfaces of magnetic and non-magnetic layers can provide valuable information on surface magnetization and the transfer of the magnetic moment across boundaries [59]. In many other cases, real-time NREF is essential to study the kinetics of inter-diffusion in polymer films, in film drainage, and foam stability, where non-equilibrium processes are dominant [59]. Such reaction kinetic studies call for continuous improvements in NREF instruments and more powerful neutron sources [59].

1.4 Motivation

The recent development of the next-generation neutron sources such as the European Spallation Source (ESS) and the Second Target Station (STS) of the Spallation Neutron Source (SNS) is anticipated to provide unprecedented neutron brightness that can enable new scientific capabilities in neutron science [15].

1.4.1 Limitation of Current Detectors

New technologies are required to exceed the scientific capabilities of previous detectors, as imposed by future instrument upgrades and upcoming research facilities [37]. The cutting-edge neutron scattering instruments set high requirements for the detectors that could otherwise become the bottleneck of the instrument's scientific performance [37]. Unfortunately, the performance of the neutron reflectometers such as SNS Liquid Reflectometer and Magnetism Reflectometer is limited by the current detector technology. The most challenging aspect of detector performance for neutron reflectometers is the rate requirement [47]. The state-of-the-art detector technology, ^{3}He-based Multi-Wire Proportional Chamber (MWPC), is reaching its performance limits, and sometimes barely fulfills the scientific needs [34]. In general, ^{3}He-based

gaseous neutron detectors are favored as they offer high sensitivity to neutrons paired with low sensitivity to gamma radiation. The ^3He-based MWPC with 3 atm propane pressure and 7 atm ^3He pressure with a 1.5 cm detector depth has a γ-sensitivity of $10^6 - 10^8$ [7]. The neutron detection efficiency is $\geq 80\%$ (2 Å) [7, 26] and the spatial resolution is 1.5 mm [7, 67]. However, when the criterion of design requires a high detection rate, the counting rate of ^{3}He-based gaseous detectors becomes a major setback [13]. The detection rate of ^{3}He gaseous detectors is predominantly limited by the comparatively slow drift velocity of ions within a reasonable range of operating pressure for gaseous detectors [13]. The maximum count rate for the MWPC was capped around $1 - 1.5$ $kcps$ (due to electronic dead time), which is lower than the count rate of a single ^3He tube detector. The count rate of a single ^3He tube peaks around $30 - 50$ $kcps$ [34, 51]. As a result, alternative high-rate detector technology is highly sought after to fulfill the unmet requirement in rate capability.

The unprecedented neutron brilliance will unleash the potential of neutron reflectivity techniques to probe smaller samples and more complex structures [59]. This is especially important as novel materials are often difficult to synthesize in large quantities and possibly with more complicated compositions [59]. The sample size is frequently required to be at least 1 - 10 cm^2 at the existing instruments, which is sometimes hard to prepare for rare materials [59]. Therefore, an adequate high rate detector will allow probing smaller and novel samples easier. Moreover, detector advancement in counting rate capability can allow reaction kinetic studies on non-equilibrium processes [59], which will expand the capacity of neutron reflectivity technique to time-resolved reflectivity measurements, making studies on the kinetics and dynamics of thin-film samples possible. Another significant contribution of a sufficiently high-performing detector can lead to a significant speed-up of current reflectivity measurements from hours, the typical time for present-day reflectivity experiments, to minutes [59]. This will reduce the precious beam time, and as a result, reduce the cost and expenses of such experiments.

1.4.2 Instrument Requirements

Although all neutron reflectometers have some basic common requirements, it is pertinent to know the detection needs of each neutron reflectometer as the detector requirement may vary based on the instrument design and instrument capability. Table 1.3 shows the detector requirement for neutron reflectometers at the First Target Station (FTS) at SNS as well as the capability of the current state-of-the-art ^{3}He detector technology.

It should be noted that the requirement on the rate capability assumes 10% dead time on the overall detection system. At SNS, two of the neutron scattering instruments are designed for neutron reflectometry, namely the Liquids Reflectometer (LIQREF) [4] and the Magnetism Reflectometer (MAGREF) [3]. The liquid reflectometer is designed to investigate the reflectivity of horizontal surfaces. It is useful for interfacial studies in polymers and surface chemistry involving thin layers of surfactants or other materials on the surfaces of liquids [46]. The magnetic reflectometer is designed to study the reflectivity and high-angle diffraction of magnetic thin films, superlattices and surfaces [46].

Table 1.4 shows the detector requirement for the next-generation neutron reflectometers anticipated to be built at STS-SNS. They are the Magnetism-Second Target Advanced Reflectometer (M-STAR), Quite Intense Kinetics Reflectometer (QIKR) and the Variable Beam Profile Reflectometer (VBPR). M-STAR is a polarized neutron reflectometer optimized for studies of magnetism and structure in magnetic heterostructure [27, 23]. QIKR is a versatile multi-purpose reflectometer with horizontal sample geometry, offering a broad "single-shot" Q-range for structural and kinetic studies of solid, solid/liquid, and free liquid surfaces and interfaces [27, 23]. VBPR is a horizontal geometry neutron reflectometer capable of delivering a variable beam profile onto a sample to study the surface and interfacial phenomena of nontraditional materials that do not meet the conventional neutron reflectivity criteria of a large, homogeneous surface area [27, 23].

Table 1.3: Detector requirement for the reflectometry instruments at the First Target Station of the Spallation Neutron Source (FTS-SNS)

Requirement	LIQREF	MAGREF	^{3}He-based MWPC
Rate capability	1 MHz	1 MHz	30 kHz
Detector efficiency (2 Å)	$\geq$ 60%	$\geq$ 60%	$\geq$ 90%
Active area	20 $\times$ 20 cm^2	20 $\times$ 20 cm^2	20 $\times$ 20 cm^2
Gamma rejection	1×10^{-6}	1×10^{-6}	1×10^{-7}
Spatial resolution	1 - 2 mm	1 - 2 mm	1.5 mm
Neutron wavelength	2.5 Å- 17 Å	1.8 Å- 14 Å	-

Table 1.4: Detector requirement for next-generation neutron reflectometry at the Second Target Station of the Spallation Neutron Source (STS-SNS) [27, 23]

Requirement	M-STAR	QIKR	VBPR
Rate capability	10 MHz	10 MHz	10 MHz
Detector efficiency (2 Å)	$\geq$ 60%	$\geq$ 60%	$\geq$ 60%
Active area	50 $\times$ 50 cm^2	20 $\times$ 20 cm^2	20 $\times$ 20 cm^2
Gamma rejection	1×10^{-6}	1×10^{-6}	1×10^{-6}
Spatial resolution	1- 2 mm	1 - 2 mm	1.5 mm
Wavelength range	2 Å- 40 Å	2.5 Å- 26 Å	2.5 Å- 26 Å

1.5 Prior Similar Work

The last decade has witnessed the development of several alternative neutron detector technologies, as a consequence of the upcoming neutron sources and upgrades, as well the worldwide shortage of ^{3}He [38, 39, 40]. There have been numerous neutron detector developments based on ^{10}B, ^{3}He, ^{6}Li, ^{113}Cd, ^{235}U and Gd. Table 1.5 shows a list of potential isotopes suitable for neutron detection. In general, ^{10}B-based and ^{6}Li-based neutron detectors are observed to be more commonly developed for high counting rate applications in neutron science, as an alternative to ^{3}He technology [37].

1.5.1 ^{10}B-based Detectors

A number of ^{10}B-based detectors such as the Multi-Blade ^{10}B-based detector [63, 62, 64], the Boron Array Neutron detector (BAND-GEM) [50, 2], and the Boron Coated Straw (BCS) detector [42, 43, 44], have been developed for high counting rate applications such as SANS, neutron reflectometry and neutron imaging. A study has shown that BCS detectors are good candidates for SANS [34], but the rate capability is still inadequate for neutron reflectometers. The BCS are anticipated to saturate around $50 - 100$ kHz per straw [34], with each BCS straw having a diameter of 7.5 mm and a length of 100 cm. BCS has a neutron detection efficiency of $\approx 50\%$ (2 Å)[19, 37], a spatial resolution of 7.5 $mm \times 6.0$ mm [19, 37] and a γ-sensitivity of 10^{-6} [42]. The Multi-Blade ^{10}B-based detectors and BAND-GEM have been demonstrated to have met the high counting rate requirement for neutron reflectometer. Although the rate requirement is fulfilled with a 2 MHz/cm^2 rate capability [2], the BAND-GEM detector falls short on the detection efficiency with (40% at 4 Å) and spatial resolution (7 mm) [50]. BAND-GEM has a γ-sensitivity of 10^{-5} [50]. Meanwhile, the Multi-Blade demonstrated a highest measured global time-average rate of 50 kHz over a beam spot of 7×16 mm^2 with less than 2% event loss [47, 49]. The detector was able to reach an instantaneous rate of 3.4 kHz per pixel (243 kHz/cm^2) [47, 49].

Table 1.5: Isotopes suitable for neutron detection and their thermal neutron capture/fission reactions.

Isotope	Cross section σ (b)	Nuclear reaction	Energy released per MeV
^{3}He	5333	$^{3}He(n,p)t$	0.76
^{6}Li	940	$^{6}Li(n,\alpha)t$	4.8
^{10}B	3837	$^{10}B(n,\alpha)^{7}Li*$	2.3
^{155}Gd	60900	$^{155}Gd(n,\gamma)^{156}Gd$	conversion $e \approx 60keV$
^{157}Gd	254000	$^{157}Gd(n,\gamma)^{158}Gd$	conversion $e \approx 60keV$
^{235}U	680	fission	170

The Multi-Blade has a neutron detection efficiency of 56% (4.2 Å) [64], a spatial resolution of $\approx 0.5 \times 2.5\ mm$ [64], a γ-sensitivity of 10^{-7} [64].

1.5.2 ^{6}Li-based Detectors

Significant progress has been made in the ^{6}Li-based detector developments, such as the Solid-State Neutron Detector (SoNDe) [32, 33, 11, 70], the Wavelength-Shifting Fiber (WLSF) detector [16, 35, 76] and neutron Anger camera [69, 68], all coupled with ^{6}Li-loaded scintillators. The WLSF detector and the Anger camera have been installed in various diffraction instruments such as POWGEN, TOPAZ, SNAP and MANDI at the SNS [76, 69, 68]. Table 1.6 details the performance of various detectors currently used at SNS. However, the counting rate capability of these detectors is still insufficient for neutron reflectometry due to the nature of readout methods employed for these detectors [33]. Readout techniques such as charge division readout, delay line readout and Anger logic take a longer time for position determination and reconstruction. Pixel readout (1:1 channel readout), used by the SoNDe detector, is the ideal readout for high counting rate designs. The SoNDe detector is designed to cope with high count rates of about 20 MHz at 10% dead time on a 1 m^2 detector area [33]. It is demonstrated that it can achieve a counting rate of 80 kHz/cm^2 [33], which exceeds the rate requirement of the SoNDe project. Detector designs similar to the SoNDe detector seem promising for high flux applications. Hence, in this project, we aim to develop a variant of the SoNDe detector that will be able to achieve higher counting rate capability and higher spatial resolution. Similar ongoing development also takes place concurrently in Germany for a general-purpose neutron reflectometer (TREFF) at the Heinz Maier-Leibnitz Zentrum (MLZ) [41].

1.6 Original Contributions

The author led all efforts in the detector development process from ideation to detector prototyping. The author collaborated with different groups of technical

Table 1.6: Operating parameters for detectors currently used at SNS first target station [27].

Technology	Resolution	Efficiency at 2 Å	Local rate (Hz/cm^2)	Full detector rate (Hz)	Gamma sensitivity	Magnetic field sensitivity
LPSD	$5-25\ mm$	$80-90\%$	$10-20K$	$100K$	$10^{-7}-10^{-8}$	-
Multi-wire	$1.5-2\ mm$	70%	$20K$	$20K$	$10^{-7}-10^{-8}$	-
Anger camera	$1.2\ mm$	$80-90\%$	$40K$	$40K$	$10^{-5}-10^{-6}$	Requires $< 25\ G$
Wavelength shifting fiber	$5\ mm$	50%	$10K$	$10K$	$10^{-6}-10^{-8}$	Requires $< 100\ G$

personnel in different stages of detector development and testing. The final design of the detector was driven by the outcomes of the analysis, experiment and investigations performed by the author. The original contributions are listed as follows:

1. **Design and fabrication of pixelated scintillator arrays**: Pixelation was introduced to the scintillators with high rate capability in mind. By pixelating the scintillator, each scintillator element (pixel) can be fully functional on its own without interfering with adjacent pixels. In other words, when a pixel is hit, the target pixel is temporarily inactive throughout the scintillation process. However, the adjacent scintillator elements are still active since the scintillation process in the target pixel does not interfere with the adjacent pixels. Several variations of the scintillator arrays (GS20) were fabricated and tested using different surface treatments (rough vs polished) and reflective coatings (air vs titanium dioxide). From experimental testings, scintillator arrays with polished surfaces with reflective coating provide the best light output and neutron-γ discrimination among other combinations. Therefore, all scintillator surfaces were made polished and reflective coatings were applied in between scintillator elements to prevent optical crosstalk between pixels. The fabrication of the scintillator array was done in collaboration with the IRD Glass Inc.

2. **Integration of a commercial readout system**: A pixelated design was adopted for both the scintillator and the photodetector with a high rate capability in mind. Due to the pixelated design of the detector the amount of electronics increases proportionally with the number of channels. Hence, it is ideal to have a scalable readout system that can handle high density of channels. A commercial silicon photomultiplier (SiPM) readout system (PETsys) that is commonly used in positron emission tomography (PET) system has been integrated to a neutron detection system. A single readout system can handle up to 1024 channels and multiple readout systems can be connected to extend

to tens of thousands of channels. This greatly improves the scalability of the detector as the final prototype of the detector is expected to be 100 times larger.

3. **Complete construction of two detector prototypes**: Two detector prototypes were fully constructed and assembled in-house at the SNS. The construction of the detector involves the coupling of scintillator arrays to SiPM arrays, the electrical interface of the SiPM arrays to readout system and the communication connection between the readout system to a computer. The assembly of the detector focuses on the mechanical stability and robustness, mechanical and electrical safety as well as radiation damage to the detector.

4. **Characterization of the detector prototypes**: A series of standardized tests was used to characterize the performance of the detector. Various tests such as neutron detection efficiency, counting rate capability, γ-sensitivity, spatial resolution, uniformity and crosstalk were performed on the detector prototypes. The detector prototypes demonstrated a significantly higher counting rate compared to the existing detectors, proving to be a promising candidate for high flux applications.

5. **Testing of detector usability in neutron reflectivity experiments**: The detector prototype was used to perform neutron reflectivity experiments at the SNS Liquid Reflectometer. The performance of the detector was evaluated and compared to the existing detector.

Chapter 2

Detector Design and Construction

2.1 Overview of Scintillator Detectors

2.1.1 Scintillators

Scintillators are materials that can detect highly ionizing radiation, which can efficiently convert the energy of the radiation into scintillation light. The overall scintillation process can be divided into three parts, illustrated in Figure 2.1 [8]:

1. **Conversion**: the process in which the energy of the incoming radiation or particles is converted into electron-hole pairs [8]. The creation of primary electron-hole pairs cascade into secondary pairs. All the electrons move to the bottom of the conduction band and the holes move to the top of the valence band. This process typically lasts for less than a picosecond.

2. **Energy transfer**: the process in which the energy of an electron-hole pair is transferred to the luminescent ion involved [8]. After the free electron-hole pairs migrate through the material, they transfer their energy to the luminescent centers. Luminescent centers are created by doping a small number of impurities/activators to the pure crystal such that energy states are created within the band gap of the pure crystal [8]. This process lasts for $10^{-8} - 10^{-12}$ s.

3. **Luminescence**: the process in which the luminescent ion returns from an excited state to the ground state via the emission of photons [8]. Because the energy levels created by the activator within a crystal are lower than the energy level in a pure crystal, the photons emitted by a doped crystal will have lower energy than in the pure crystal. Therefore, the emission spectrum is shifted to longer wavelengths.

It is important that the scintillator has a high light output so that the scintillator has an efficiency for converting ionizing radiation into scintillation light. This gives scintillators sensitivity to the energy of the ionizing radiation. For fast signal response, it is also important that the scintillator has a short decay constant. Most scintillators are characterized by more than one decay time, so the effective decay time is considered instead. This is important for high timing resolution or high counting rate applications. It is also advantageous when the scintillator exhibits pulse shape discrimination capability, meaning that the shape of the emitted light pulses is different for different particles. This allows the scintillator to identify different particles based on the pulse shape of the signal. The pulse shape discrimination is due to the excitation of different fluorescence mechanisms by particles with different ionizing power. There are several important characteristics of scintillators summarized in Table 2.1.

2.1.2 Silicon Photomultipliers

To make use of the scintillation light produced by the scintillator, the scintillation light needs to be converted into electrical signals for further processing. Typically, this is done using a photodetector such as a photomultiplier (PMT), an avalanche photo detector (APD), a silicon photomultiplier (SiPM) or a micro-channel plate photomultiplier (MCP-PMT).

For this project, we chose silicon photomultiplier (SiPM) as the photosensor for our detector as we want to explore the potential of SiPMs in high flux applications.

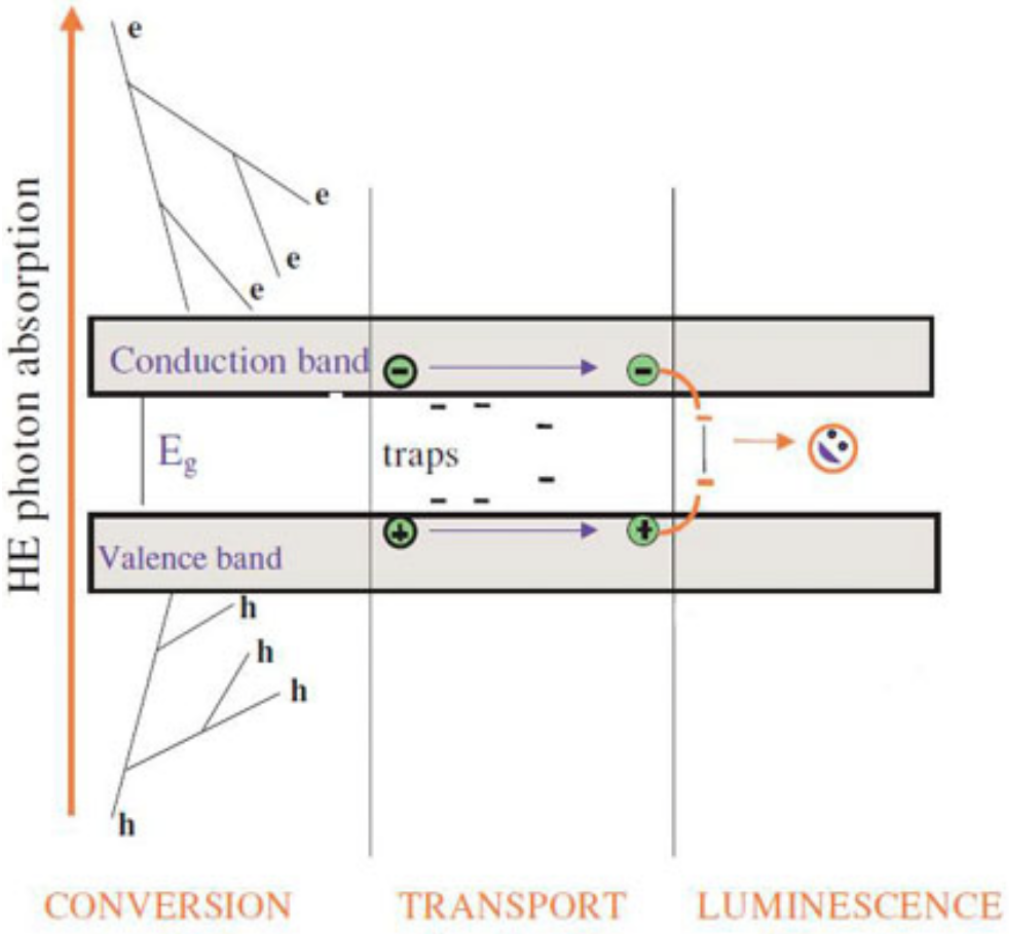
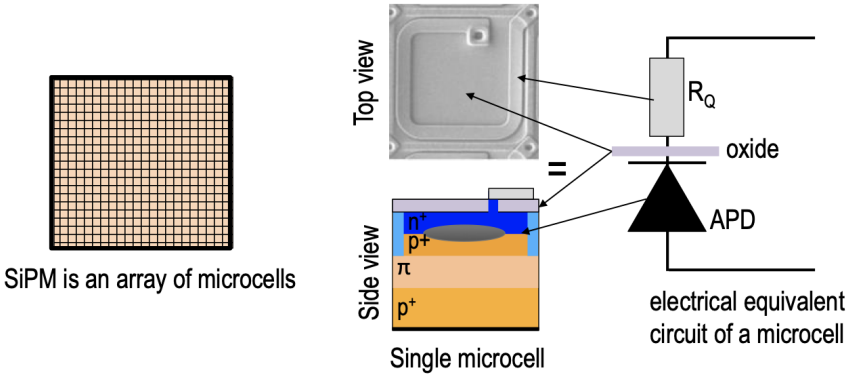


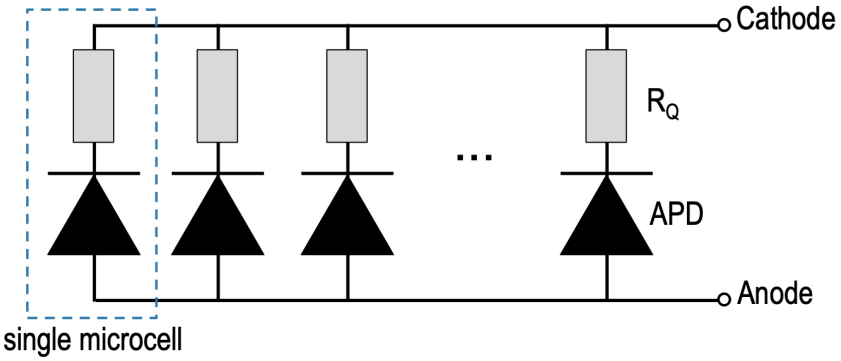
Figure 2.1: Scintillation mechanism: conversion, energy transfer and luminescence.

Table 2.1: Characteristics of a scintillator [31].

Characteristics	Descriptions
Light yield $(photons/MeV)$	Number of emitted photons per absorbed energy.
Energy resolution (%)	Ability of a material to discriminate between two radiations of slightly different energies
Decay time (s)	The time after which the intensity of light $I(t)$ has reduced to $1/e$ of its maximum, as characterized by τ.
Peak emission wavelength (nm)	The peak wavelength of the emitted photon
Stopping power	Attenuation coefficient of the absorbed radiation, for a given thickness of a material



(a)



(b)

Figure 2.2: (a) A typical structure of a SiPM (b) All of the microcells are connected in parallel, and each SiPM has an anode and a cathode [61].

The SiPM is attractive in our application because it has a relatively fast response, making it suitable for high counting capability. It is also insensitive to magnetic field unlike the photomultipliers (PMT), which is suitable for scattering instruments operated in magnetic fields such as the MAGREF and M-STAR. It is also operated under a substantially lower high voltage as compared to the PMT, which reduces the power consumption. Additionally, it can be mass-produced, hence lowering the commercial cost of SiPM. There are several important characteristics of SiPM to consider when making a selection for a specific application:

SiPMs are solid-state silicon photodetectors operating in the Geiger mode. A SiPM integrates a dense array of small, independent avalanche photodiodes (APDs), each with its own quenching resistor, R_Q. Each independently operating unit of APD and quench resistor is referred to as a microcell [61]. The structure of a SiPM is shown in Figure 2.2. A SiPM is externally biased at a voltage that is above the APD breakdown voltage, which is the key to Geiger mode operation [61]. Upon the absorption of a photon in APD, a charge carrier is created. The bias voltage applied sets up an electric field which will accelerate the charge carrier where it creates secondary charge carriers through impact ionization [61]. The self-perpetuating ionization cascade is the Geiger avalanche. The avalanche can produce 10^5 - 10^6 carriers, and this constitutes the gain. When the photocurrent flows through the microcell, the voltage across the quenching resistor drops, which reduces the voltage bias across the diode to be below the breakdown voltage. This mechanism prevents further Geiger-mode avalanches from occurring [61]. Once the current has been quenched, the voltage across the diode recharges to the nominal operating bias voltage. The time it takes for the microcell to recharge to full operating voltage is the recovering time [61].

Table 2.2: Characteristics of SiPMs [61]

Characteristics	Descriptions
Breakdown voltage, V_{br} (V)	Minimum (reverse) bias voltage V_br to initiate self-sustaining avalanche multiplication
Overvoltage, ΔV (V)	The difference between V_{bias} and V_br
Photon detection efficiency, PDE (%)	Number of detected photons over the number of incident photons
Gain, G	the number of charges generated in a Geiger discharge (typically $10^5 - 10^7$)
Recovering time (s)	Time taken between the quenching of the avalanche and when the microcell is fully ready to detect an incoming photon
Dark count rate (Hz)	Random generation of electron-hole pairs and carriers due to thermal agitation and other factors
Afterpulsing	Occurs when carriers are trapped during the avalanche multiplication and are discharged during the recovering phase
Optical crosstalk	Net effect of the secondary avalanche in adjacent microcells
Temperature characteristics	Influence of temperature on other parameters such as the breakdown voltage, gain, junction capacitance, dark counts and photon detection efficiency

2.2 First Detector Prototype

2.2.1 Neutron Scintillator

The scintillator that we use is a Ce-activated lithium aluminosilicate glass, also known as the GS20, from Scintacor (Cambridge, UK) [72]. The ^{6}Li isotope has a thermal neutron capture cross-section of 940 barns with the following nuclear reaction:

$$ {}^{1}_{1}n + {}^{6}_{3}Li \rightarrow {}^{4}_{2}\alpha\ (2.05MeV) + {}^{3}_{1}H\ (2.73MeV) \tag{2.1} $$

It has a lithium content of 6.6% by weight and isotopic enrichment of 95% ^{6}Li [74, 72]. The luminescence centers in GS20 are the Ce^{3+} ions. The ionization of the scintillating medium due to the energy imparted by the reaction products (α and triton) excites the cerium ions [74]. Upon de-excitation, the excited cerium emits isotropic light, with an emission spectrum shown in Figure 2.3. This wavelength emission spectrum is a key parameter for finding a suitable optical coupling layer and the photocathode type of a photosensor because wavelength compatibility is a requirement for efficient photon transfer.

The GS20 offers a reasonable light yield (about 6,000 photons per absorbed neutron) [71] and has a fast decay time between 50 to 70 ns due to the Ce^{3+} dipole 5d-4f transition [41]. The absorption length of an α particle is 5-10 μm and for a tritium is $40 - 150\ \mu m$ [41]. The detection efficiency of 1 mm and 2 mm of GS20 is 75% and 95 % respectively for thermal neutrons [74]. Features such as fast response, high neutron capture efficiency, reasonably sufficient light yield make GS20 a very attractive neutron converter for high counting rate applications.

Unfortunately, GS20 is also sensitive to γ-rays, which renders the n/γ discrimination capability to be more of a challenge. Since γ-rays can also interact with the scintillator and generate a scintillation signal that can be of comparable magnitude [29], this will result in poor n/γ discrimination in detection systems that only utilize pulse height discrimination to discriminate against γ-rays. Another limitation of

Table 2.3: GS20 properties [72]

Properties	GS20
Density (g/cm^3)	2.50
Coefficient of linear expand/^oC	9.23×10^{-6}
Light output relative to anthracene*	20-30%
Light yield (photons/absorbed neutron)	$\sim$ 6,000
Fast/slow/90% to 10% decay times (ns)	18/57/98
Wavelength of maximum emission (nm)	395
Refractive index at maximum emission	1.55

* Determined by thickness, increasing with decreasing thickness down to approximately 2 mm

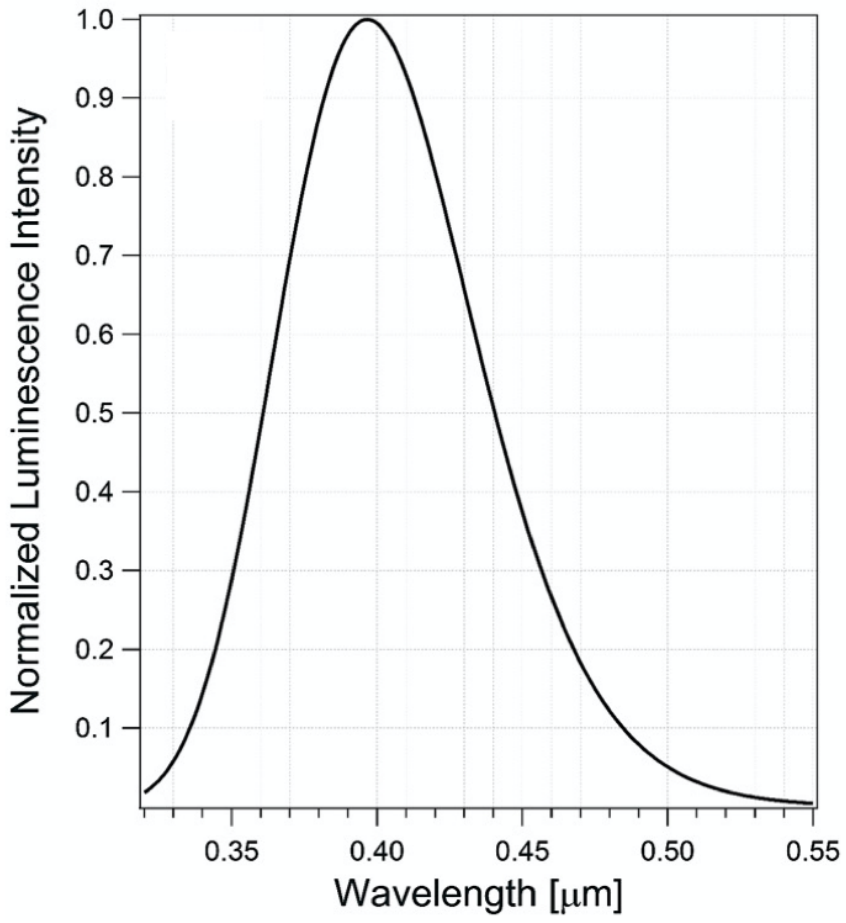


Figure 2.3: Photoluminescence spectrum of GS20 scintillator glass for optical excitation wavelengths in 325 - 400 nm range [29]

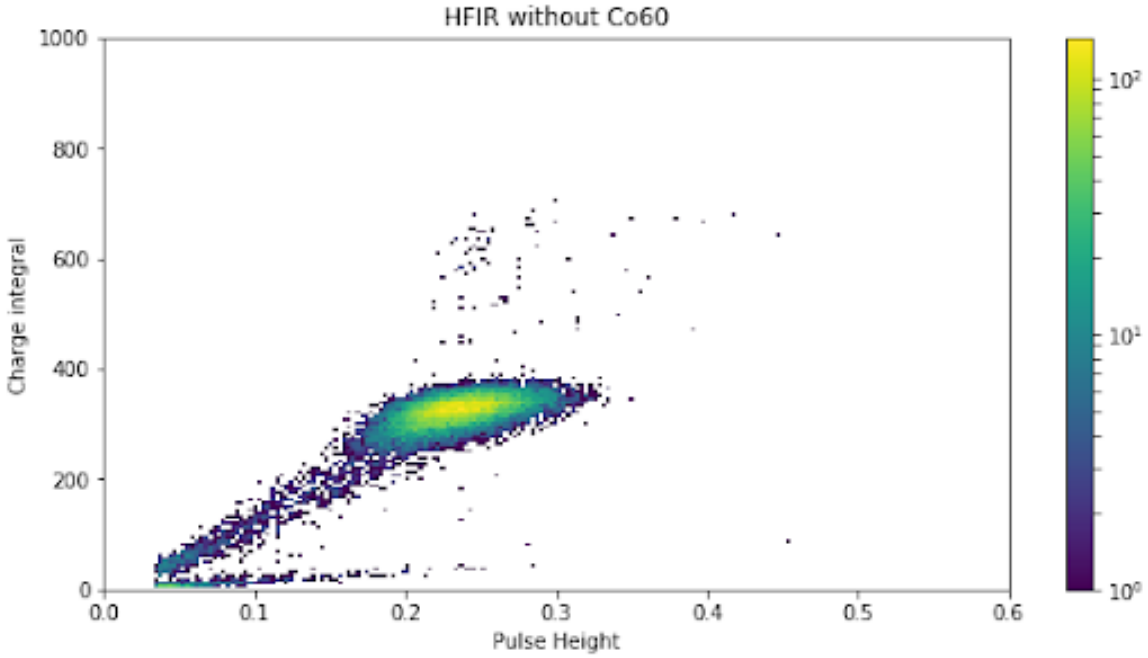
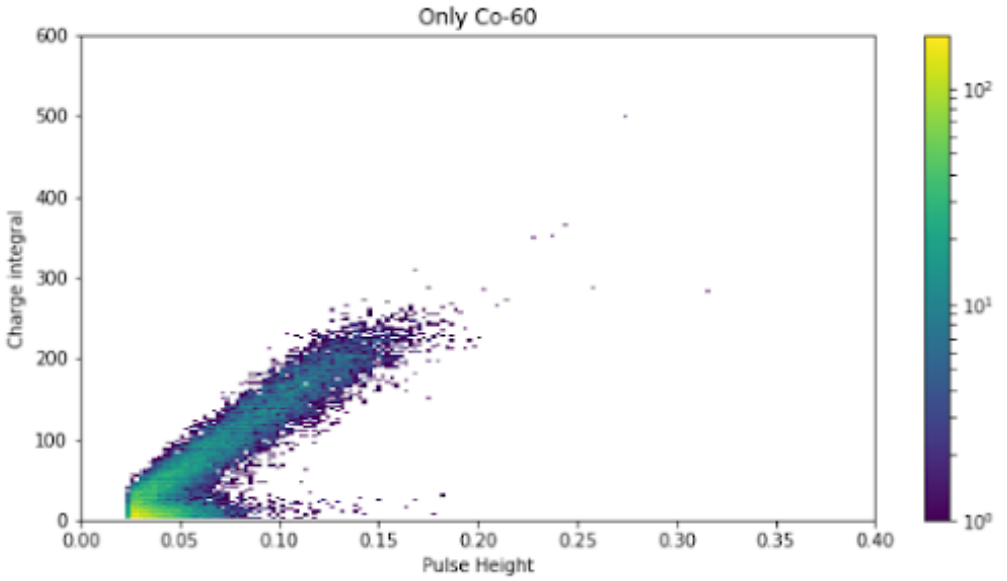
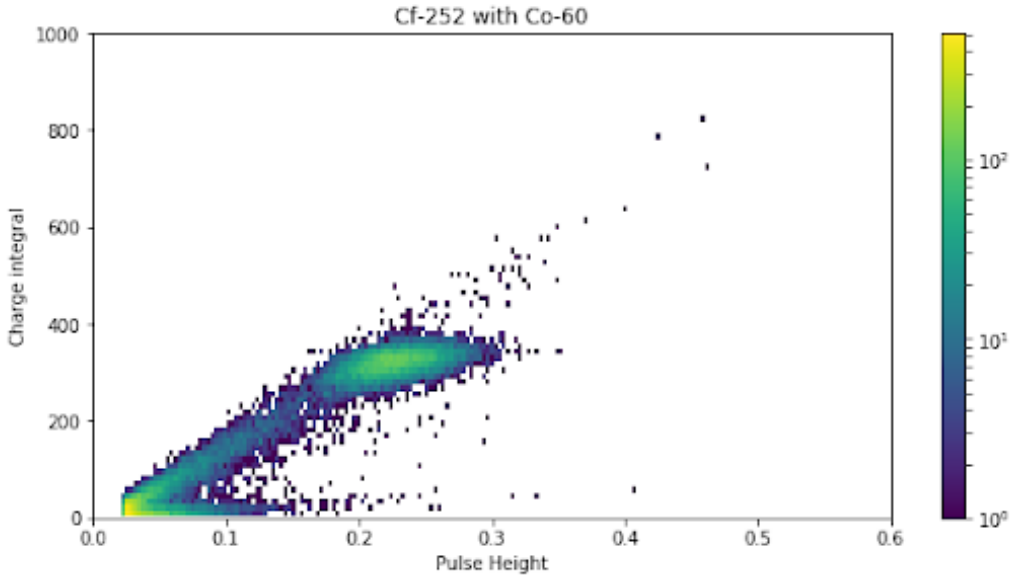


Figure 2.4: The area of high intensity are presumably neutron events and any other surrounding data points are unwanted events from noise and γ-rays.



(a)



(b)

Figure 2.5: (a) Irradiation of γ-rays shows a linear response from γ events and a constant response from noise (b) Irradiation of both neutrons and γ-rays shows a combination of linear response from gamma events, a constant response from noise in addition to the neutron events.

GS20 is that it provides the same pulse shape for both neutrons and γ events in the scintillator. If the signals from both neutrons and γ-rays have the same amplitude, they will exhibit a similar pulse response as well. Hence, it is more difficult to perform pulse shape discrimination on GS20 to discriminate neutrons against γ-rays.

The measurement in Figure 2.4 was obtained using a photomultiplier tube (Hamamatsu ET60098) with a 2" $\times$ 2" GS20 glass scintillator. The measurement was taken at the instrument development beam line CG-1A in the High Flux Isotope Reactor (HFIR), where the neutron source was relatively clean. There were some background γ-rays produced at the beam line due to the interaction of neutrons with the surrounding materials. The region with high intensity of data points was contributed by neutrons, meanwhile the data points following a linear trend were contributed by γ-rays. The constant response at low charge integral was contributed by noise. Two other measurements, shown in Figure 2.5, were made at the detector lab at the SNS. Figure 2.5a was obtained using a γ source (calibrated ^{60}Co sealed source), where the linear trend observed was predominantly contributed by the γ-rays emitted from ^{60}Co source. Meanwhile, Figure 2.5b was taken using a moderated neutron source (^{252}Cf). The ^{252}Cf source is not a clean neutron source as ^{252}Cf produced both neutrons and γ-rays, as shown in the plot.

2.2.2 Silicon Photomultiplier

The SiPM array used in the first prototype was the ArrayC-10035064P-BGA from SensL (Cork, Ireland). It is an 8 $\times$ 8 array of SiPM sensor elements (MicroFC-10035-SMT) on a printed circuit board (PCB) with individual pixel readout and ball grid array (BGA) I/O interface [54]. Each sensor element has an active area of 1 mm $\times$ 1 mm, which consists of 576 microcells with a size of 35 μm [54].

The SiPM is sensitive to the full range of the GS20 emission wavelengths, shown in Figure 2.6. At 395 nm (the maximum emission wavelength of GS20), the SiPM has a photon detection efficiency of close to 30 % with an overvoltage of 2.5 V [54]. Higher overvoltage improves the photon detection efficiency and the gain of the SiPM, but

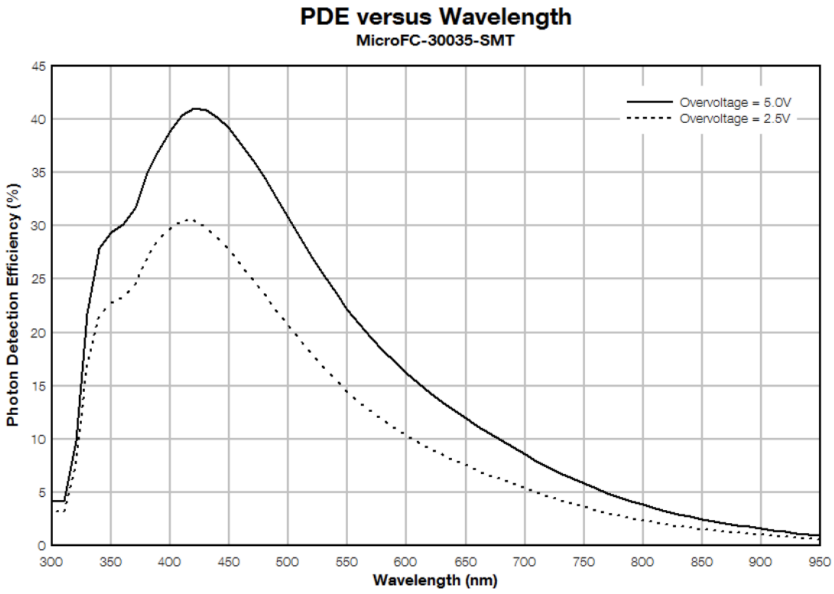


Figure 2.6: A plot of photon detection efficiency (PDE) versus wavelength, with a peak wavelength at 420 nm [54].

Table 2.4: Characteristics of SensL SiPM (ArrayC-10035064P-BGA). Values are quoted for 1 mm sensor size, microcell size of 35 μm and overvoltage of 2.5 V [54].

Properties	Nominal values
Breakdown voltage, V_{br} (V)	24.2 - 24.7
Overvoltage, ΔV (V)	1.0 - 5.0
Spectral range, λ (nm)	300 - 950
Peak wavelength, λ_p (nm)	420
Photon detection efficiency, PDE (%)	31
Dark current (nA)	15
Dark count rate, DCR (kHz)	30
Microcell recharge time constant (ns)	82
Crosstalk (%)	7
Afterpulsing (%)	0.2

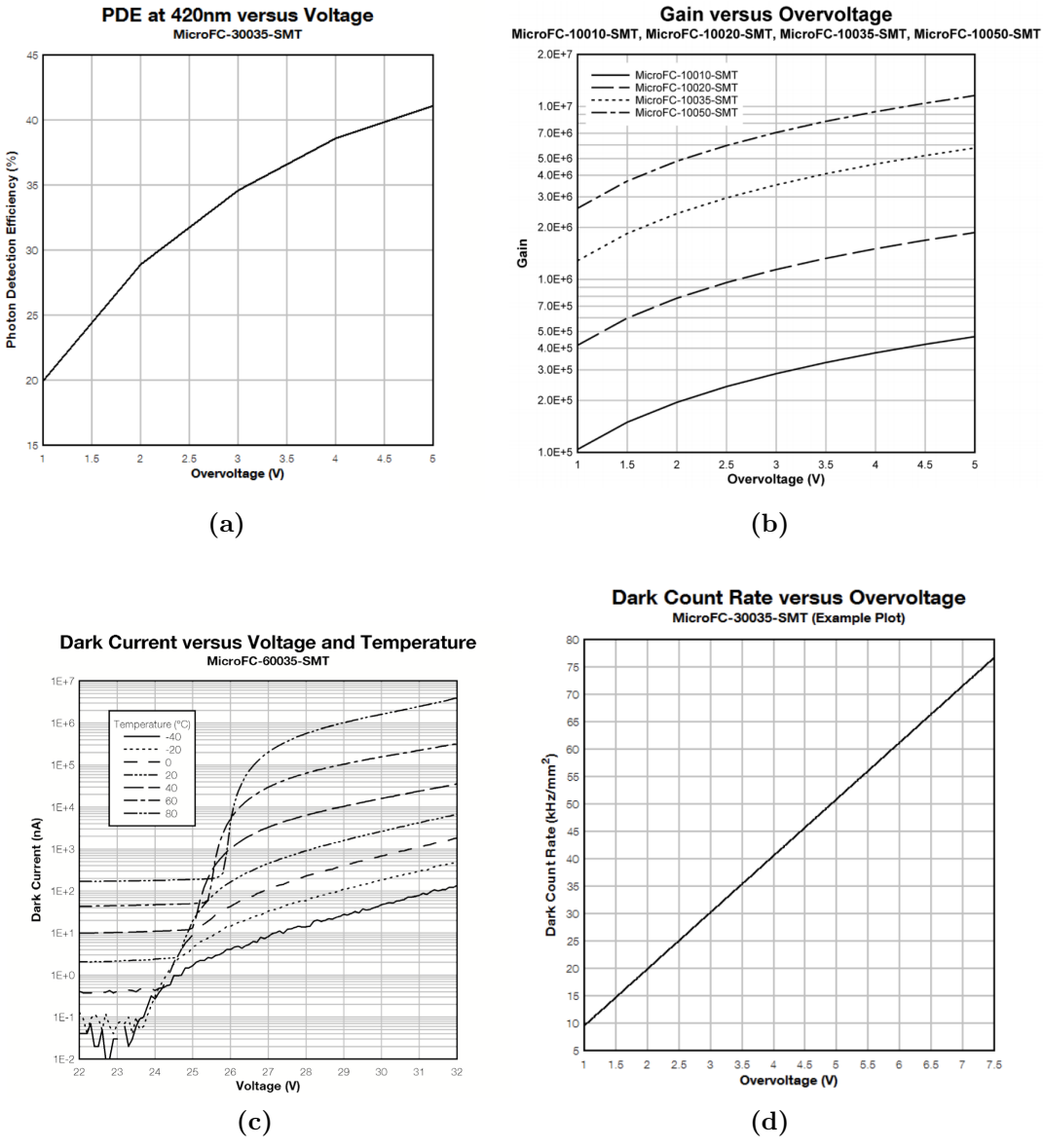
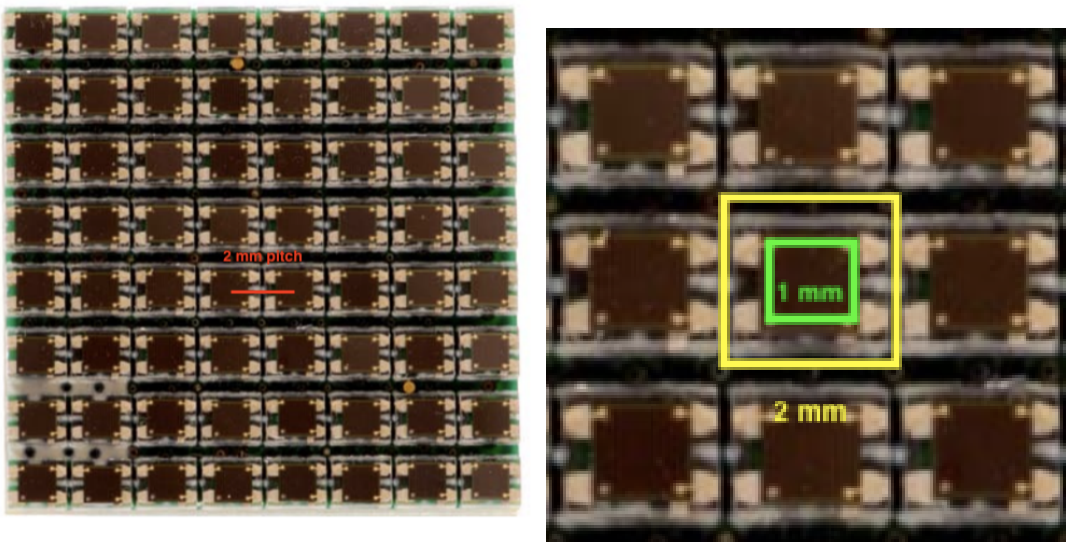


Figure 2.7: (a) PDE versus overvoltage (b) Gain versus overvoltage (c) Dark current versus voltage. The voltage used for our detection system is 27.5 V, including an overvoltage of 3.0 V [54].



(a) **(b)**

Figure 2.8: (a) An 8 × 8 array of SiPM with a pitch of 2 mm (b) Magnified view of the sensor elements with an active area of 1 mm × 1 mm. [54].

also increases the dark current of the SiPM as shown in Figure 2.7 [54]. The trade-off in detector performance depends on the overvoltage, which needs to be fine-tuned. More important properties of the SensL SiPM are tabulated in Table 2.4.

The SiPM array itself has a pitch of 2 mm, which is about $2 \times 2\ mm^2$ in size for each SiPM. However, the active area of a SiPM is $1 \times 1\ mm^2$. This means that there is actually a significant amount of dead space in each SiPM. The active area of each SiPM is only 1/4 the size of a single SiPM. In Figure 2.8, the active area of a sensor element is represented in the green box and the dead space of a sensor is the area outside of the green box within the yellow box. Because the SiPM array only comes with a BGA interface, a custom PCB was needed to mount the SiPM array to the readout system in order to process and analyze the detector signals.

2.2.3 Readout Electronics

For the readout system of the first detector prototype, we used the Channel Read-Out-Card (CROC). The CROC board consists of 64 comparators (LTC6752ISC6-1#TRMPBF) and 8 12-bit digital-to-analog converters (DAC7578). The method of detecting an event is based on pulse height discrimination (PHD) using the 64 comparators. The comparator is triggered when the amplitude of a signal exceeds a certain threshold. That is how an event is counted. Additionally, a field-programmable gate array (FPGA) was integrated into the CROC board for I/O control of the CROC board, data acquisition, digital signal processing and data transfer to a computer via an Ethernet. The signal flow diagram for the readout system is illustrated in Figure 2.9.

We used the AVNET MicroZed which is a development board based on the Xilinx ZYNQ-7000 All Programmable System on Chip [5]. The AVNET MicroZed is shown in Figure 2.10. The MicroZed contains two I/O headers that provide a connection to two I/O banks on the programmable logic (PL) side of the ZYNQ-7000 All Programmable SoC device [5]. When plugged into a carrier card, the I/Os are accessible in a manner defined by the carrier card design. The carrier card contains

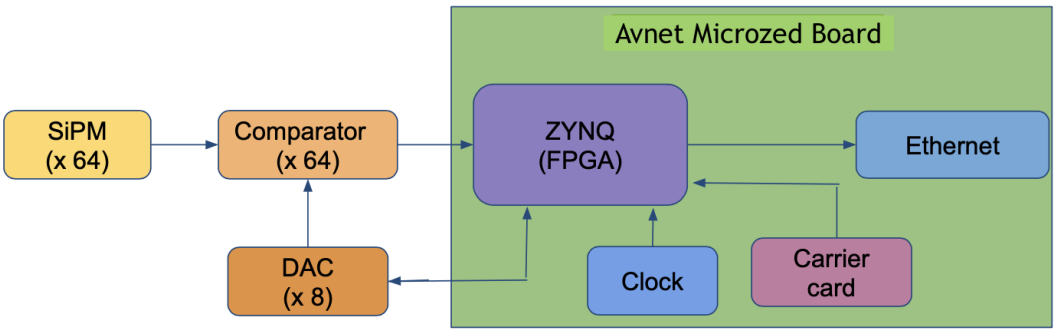
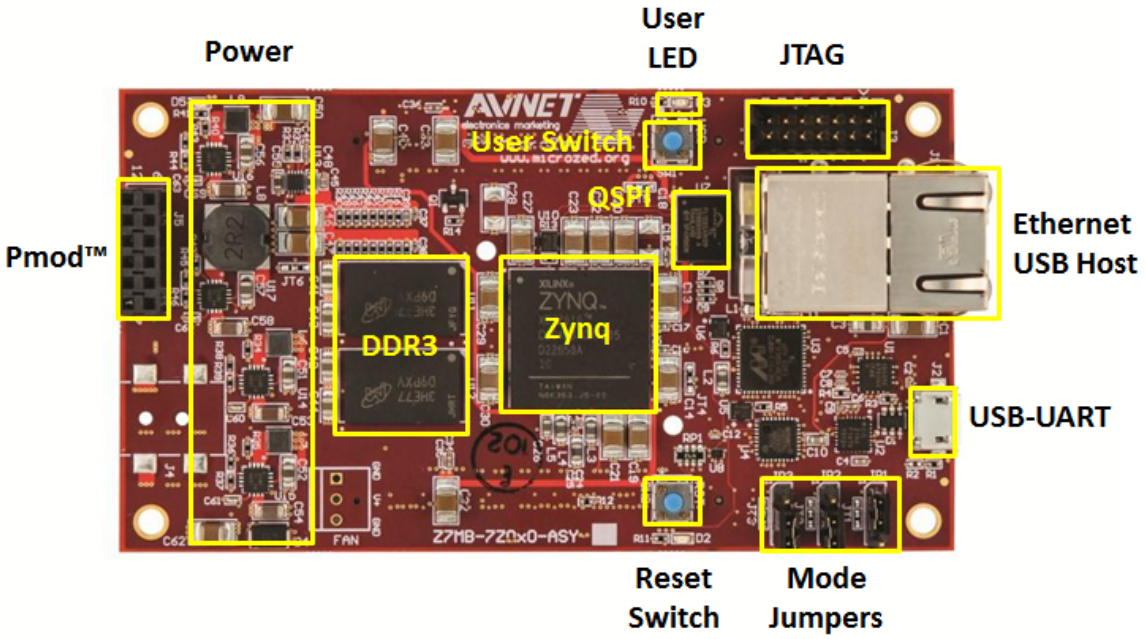
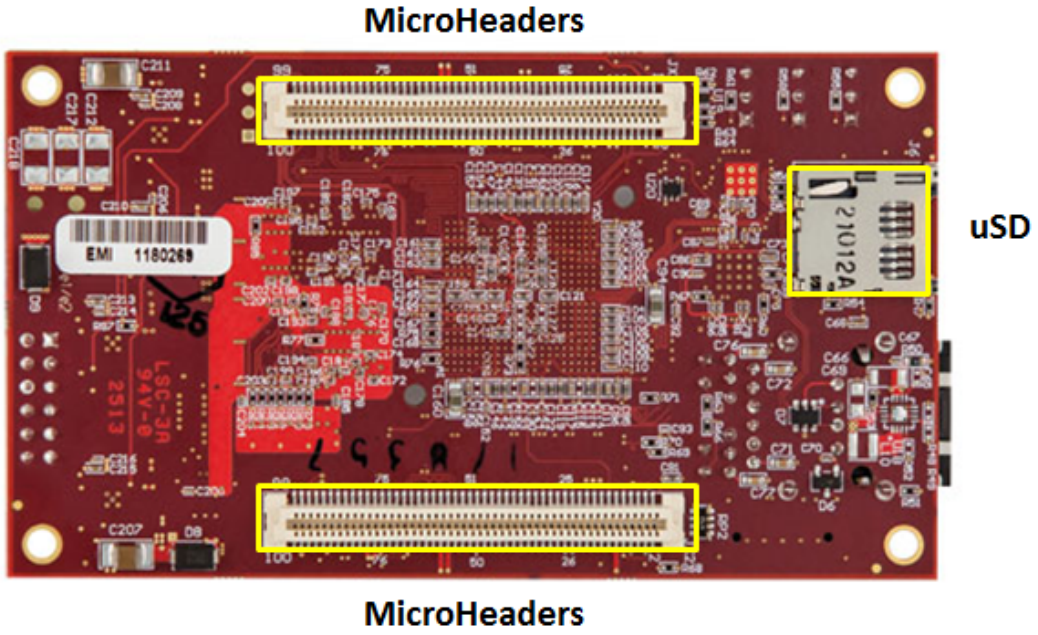


Figure 2.9: Signal flow diagram in FPGA-based data acquisition system. FPGA is interposed between the input and the output, such as analog-to-digital converters (ADCs), digital-to-analog converters (DACs), and the communication bus with the host.

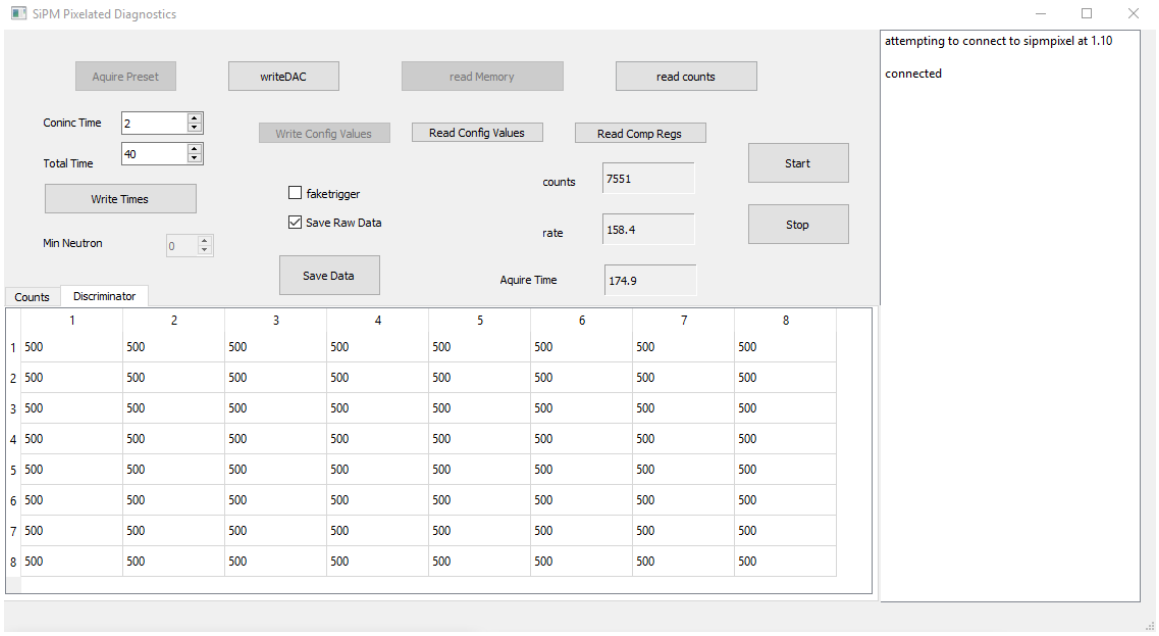


(a)

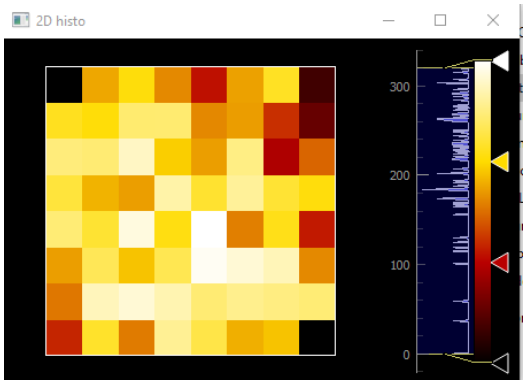


(b)

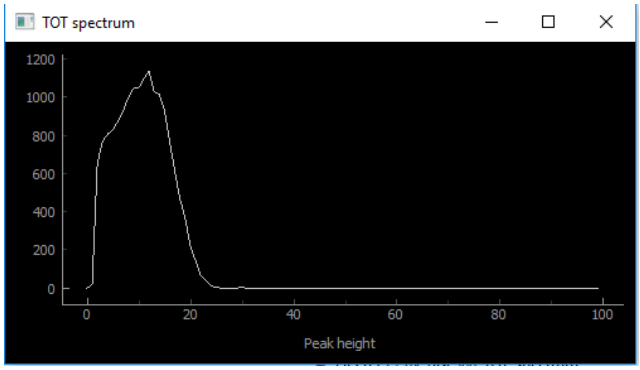
Figure 2.10: Photos of (a) front view and (b) back view of the AVNET MicroZed development board [5].



(a)



(b)



(c)

Figure 2.11: This GUI is the interface allows users to specify input parameters to the FPGA and obtain real time results on the detector.

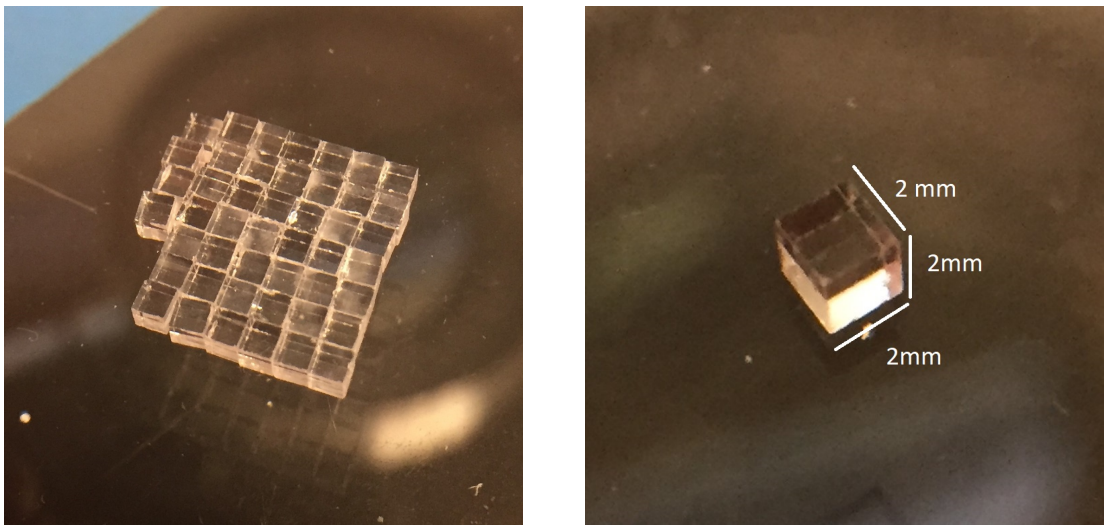
the firmware written for the data acquisition process. This includes I/O controls, event counting and digital signal processing. A Time-over-Threshold (ToT) routine was programmed into the firmware. A ToT method measures the width of a signal of which the amplitude exceeds a certain threshold [6, 25]. This routine was incorporated as part of the firmware to help improve neutron-γ discrimination of the detector. A Transmission Control Protocol (TCP)-based communication program was written in Python to allow users to specify configurable parameters on the FPGA and receive data from the FPGA. The program provides a graphical user interface (GUI) to controls, data reporting and plot visualization as shown in Figure 2.11.

2.2.4 Full Assembly

For the first prototype, we developed a proof-of-concept of the high rate detector with an active area of 16 $mm \times 16$ mm and 64 independent channels using GS20 neutron scintillator, SensL ArrayC-10035064P-BGA SiPM and the CROC board made in-house as the readout system.

A 2" $\times$ 2" piece of GS20 scintillator was cut in-house into scintillator cubes of size 2 mm $\times$ 2 mm $\times$ 2 mm as shown in Figure 2.12. Each scintillator cube is polished first by coarse grating paper (5 mm), then by fine grating paper (0.5 μm) to accomplish polished finishes. Reflective coating (Saint-Gobain Crystals BC-620) [28] is painted on all 5 surfaces of the scintillator cube, leaving only 1 surface that is coupled to the SiPM unpainted. No optical grease/layer has been applied in between the scintillator cubes and the SiPM array. A plastic assembly was made to mount the scintillator arrays to the SiPM array by centering each scintillator element to each SiPM.

Each individual channel in the SiPM is read out independently using a custom-made mounting board that acts as an interface between the SiPM array and the readout system (the CROC board). Individual counts are registered and counted on the MicroZed board using custom Verilog firmware. The firmware interfaces with a C++ control program executing under Linux to access and control the I/O of the development board. An Ethernet connection is established between the MicroZed



(a) **(b)**

Figure 2.12: Photos of (a) an array of Scintillator cubes and (b) a single cube with dimensions added.

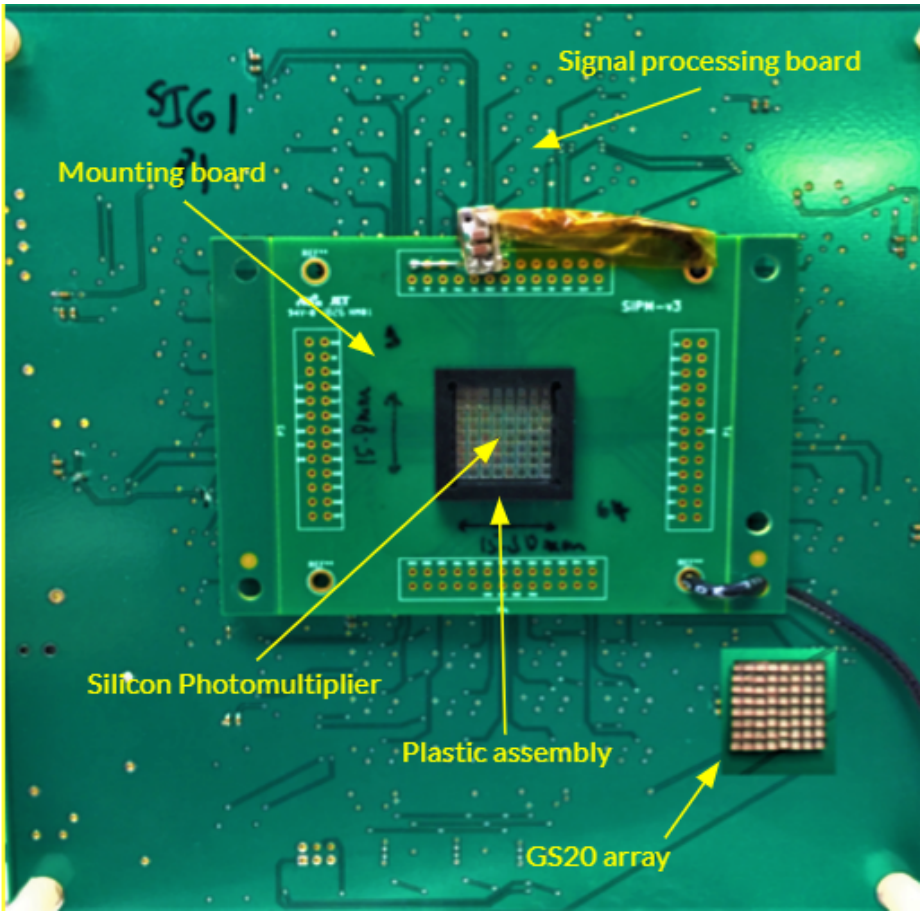
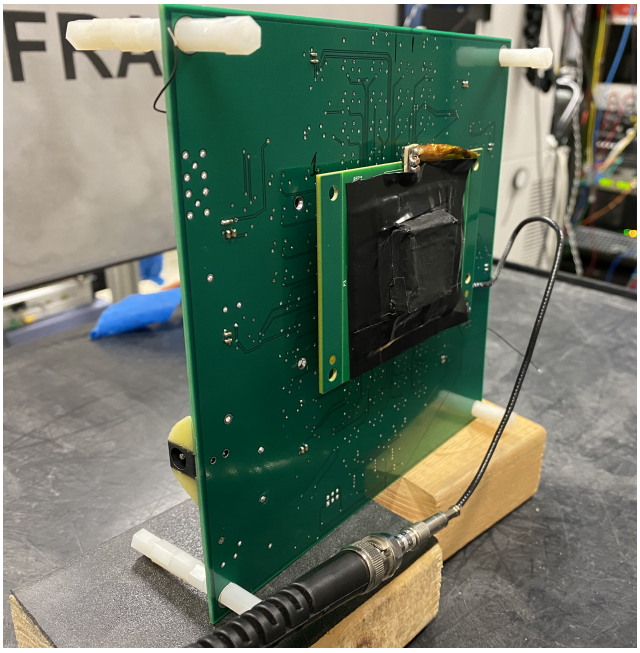
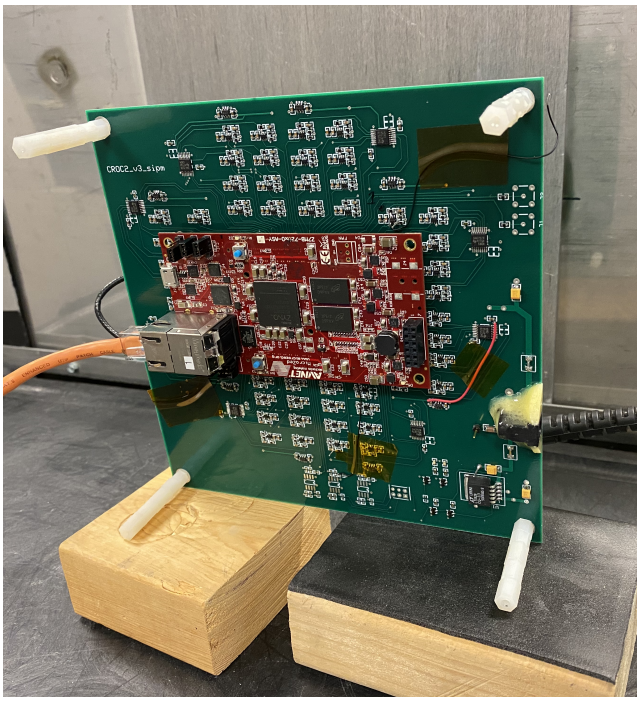


Figure 2.13: SiPM array with the associated electronics.



(a)



(b)

Figure 2.14: Photos of (a) back view, (b) front view and (c) side view of our detector prototype.

board and a computer for data collection and processing. A TCP-based Python communication was written to control the discrimination threshold of PHA and the integration time of ToT, and to receive data from the FPGA. Figure 2.13 shows labeled components of the front view of the detector prototype prior to being sealed using the Super 88 Black Polyvinyl Chloride Electrical Insulation Tape to ensure that the detector is light-tight. Figure 2.14 shows the full assembly of the first detector prototype from three perspectives: front view, side view and back view.

During acquisition, a voltage of 27.5 V was applied to bias the SiPM array. The bias voltage is the SiPM breakdown voltage and the overvoltage combined. A 5 V was supplied to power up the CROC board and the Avnet MicroZed FPGA. An Ethernet was connected from the FPGA to a computer for data transfer.

2.3 Second Detector Prototype

For the second detector prototype, several major changes were implemented. The first major change was the replacement of the current readout electronic with a commercially available SiPM readout system. The readout system is well-suited for scalable and high-rate applications. With the readout system, the detector module can be scaled up to a larger system relatively easily. The second change introduced to the second prototype was the substitution of the original SiPM model due to product discontinuation. The new SiPM model has a minor difference in dimension compared to the original SiPM model, which introduced a minor change in the pitch of the scintillator array. Lastly, the quality of the scintillator array has been improved with the collaboration with an external glass vendor, and can be manufactured in larger quantities.

2.3.1 Major Changes Implemented

There are three main improvements made for the second detector prototype:

1. **Ability to Scale Up**

   As part of the instrument requirement, the final detector prototype should have an active area of $20 \times 20\ cm^2$. Currently, the active area of the first detector prototype is $16 \times 16\ mm^2$. Therefore, the first detector prototype needs to be scaled to a larger system to meet the active area requirement. As shown in Figure 2.14, the readout electronics are significantly larger than the active area of the detector. It is not an ideal design for a scalable system. Thus, an alternative solution is needed either by rearranging the readout electronics in a scalable fashion or by seeking other commercial readout systems available in the market that suit our high-rate application and are highly scalable.

2. **Discontinuation of ArrayC-10035064P-BGA SiPM**

   After the SensL Technologies Ltd. company was acquired by ON Semiconductor, the SiPM model (ArrayC-10035064P-BGA) was discontinued in production. Even though the SiPM array is no longer for sale, the individual SiPMs that make up the whole array are still available. There is a possibility to re-build the original SiPM array. However, due to the interest of time, an alternative SiPM model that is commercially readily available and quality assured is needed to replace the current model.

3. **Mass Production of GS20 Scintillator Arrays**

   The scintillator arrays were made in-house at Oak Ridge National Laboratory. However, it is a long and tedious process to obtain a good quality that is consistent throughout all elements in the scintillator array. Hence, it was important for us to collaborate with external companies that have expertise in glass fabrication and manufacturing in order to produce consistently high-quality scintillator arrays in large quantities.

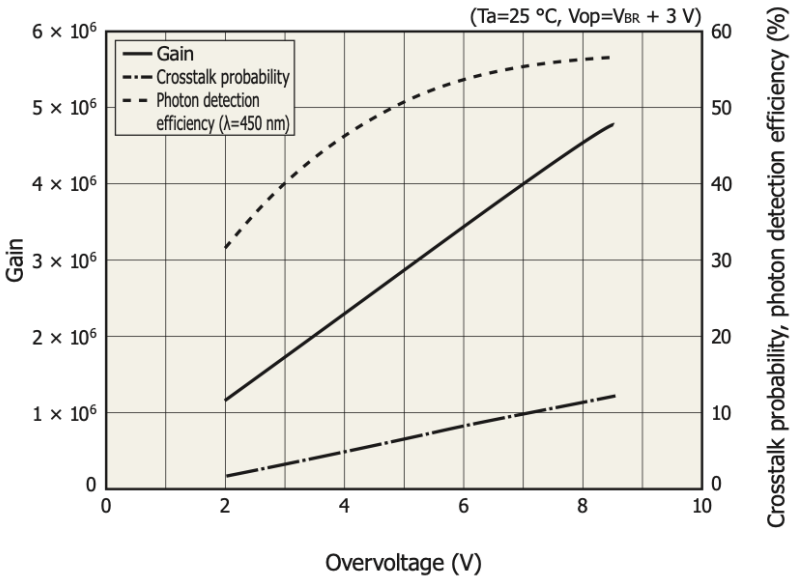
2.3.2 Silicon Photomultiplier

The discontinuation of the SensL ArrayC-10035064P-BGA SiPM has led us to search for a replacement on the market. The closest SiPM array we could find in terms of pixel size and pixel pitch is the Hamamatsu S13361-2050AE-08 Multi-Pixel Photon Counter (MPPC) array. It is an 8×8 array on a printed circuit board with a connector made by SAMTEC mounted on the back side of the board [60]. The effective photosensitive area for each channel is $2 \times 2\ mm^2$ [60]. Each sensor element has 1584 microcells with a fill factor of 74% [60]. Between each sensor element, there is a gap of 0.2 mm and between MPPC arrays, there is a gap of 0.4 mm [60]. The window is made up of epoxy resin with a refractive index of 1.55 [60]. Table 2.6 outlines the differences between the SensL ArrayC-10035064P-BGA SiPM and the Hamamatsu S13361-2050AE-08 MPPC array.

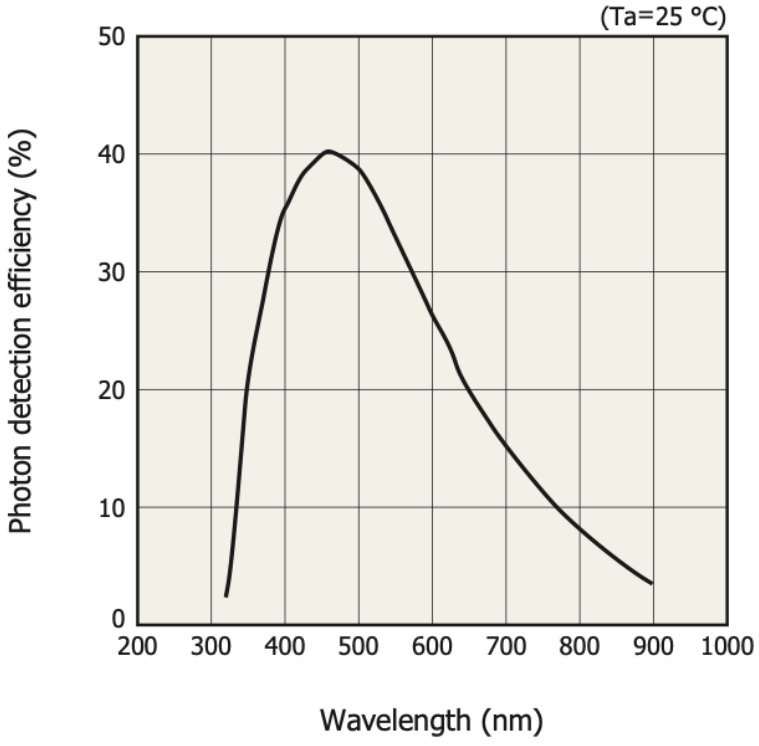
2.3.3 Readout Electronics

The PETsys readout system is a complete readout system designed to read a large number of SiPM channels with a high data rate and excellent time resolution [21]. It is based on the TOFPET2 ASIC [22]; each chip can handle the readout and digitization of 64 independent SiPM channels [22]. The readout system offers two modes of measurement: time and charge (QCD) mode and dual time (ToT) mode [22]. The QCD measures the integrated charge of the signal and ToT measures the width of the signal above a certain threshold [22].

The evaluation kit includes two Front-End Modules (FEM128), one Front-End type D module (FEB/D-1024), firmware for the FEB/D board and application software for data acquisition [20]. The FEM128 is made up of three different boards: FEB/A, FEB/S and FEB/I [20]. The FEM128 has two FEB/A boards, each of which has a PETsys TOFPET2 ASIC with 64 channels [21]. The FEB/S board is a passive board adapting the SiPM array to the input connector on the FEB/A board [21]. The FEB/I board allows the FEB/D to communicate with both ASICs in the FEM128



(a)



(b)

Figure 2.15: Characteristics of Hamamatsu MPPC [60].

Table 2.5: Characteristics of Hamamatsu S13361-2050AE-08 MPPC [60].

Properties	Value
Breakdown voltage, V_{br} (V)	53 ± 5
Overvoltage, ΔV (V)	1.0 - 5.0
Spectral range, λ (nm)	320 - 900
Peak wavelength, λ_p (nm)	450
Photon detection efficiency, PDE (%)	40
Dark count rate, DCR (kHz)	300
Crosstalk (%)	5

Table 2.6: Differences in specification between SensL ArrayC-10035064P-BGA SiPM (shortened as SensL SiPM) and Hamamatsu S13361-2050AE-08 MPPC array (shortened as Hamamatsu MPPC) [54, 60].

	SensL SiPM	Hamamatsu MPPC
Number of pixels	8×8	8×8
Photosensitive area/channel (mm^2)	1×1	2×2
Number of microcell	504	1584
Microcell size (μm)	35	50
Microcell fill factor (%)	64	74
Array pitch (mm)	2.0	2.2
Dead space between pixels (mm)	1.0	0.2
Breakdown voltage, V_{br} (V)	24.2 - 24.7	53 ± 5
Overvoltage, ΔV (V)	1.0 - 5.0	1.0 - 5.0
Spectral range, λ (nm)	300 - 950	320 - 900
Peak wavelength, λ_p (nm)	420	450
Photon detection efficiency, PDE (%)	31	40
Dark count rate, DCR (kHz)	30	300
Crosstalk (%)	7	5
Afterpulsing (%)	0.2	-

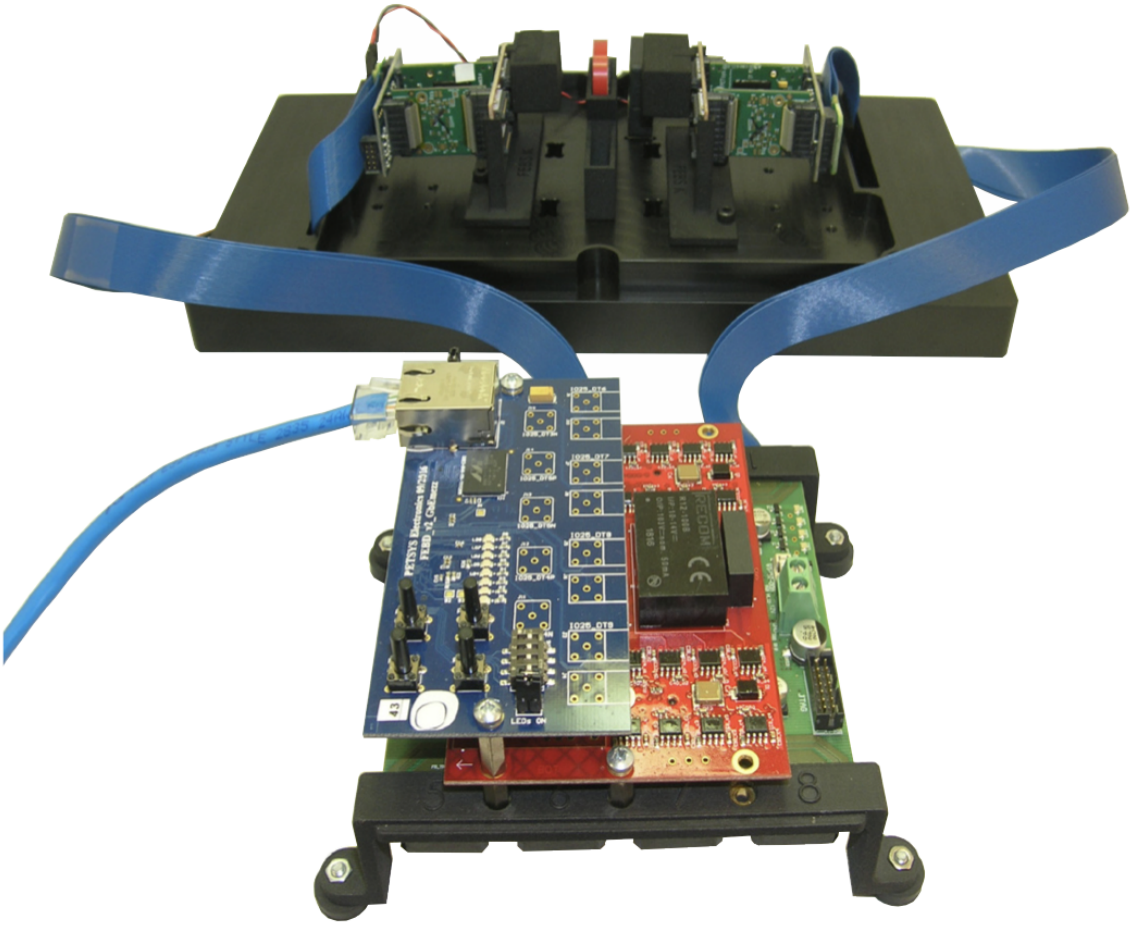


Figure 2.16: The PETsys TOFPET2 ASIC evaluation kit consists of two FEM128, one FEB/D board, firmware and software [20].

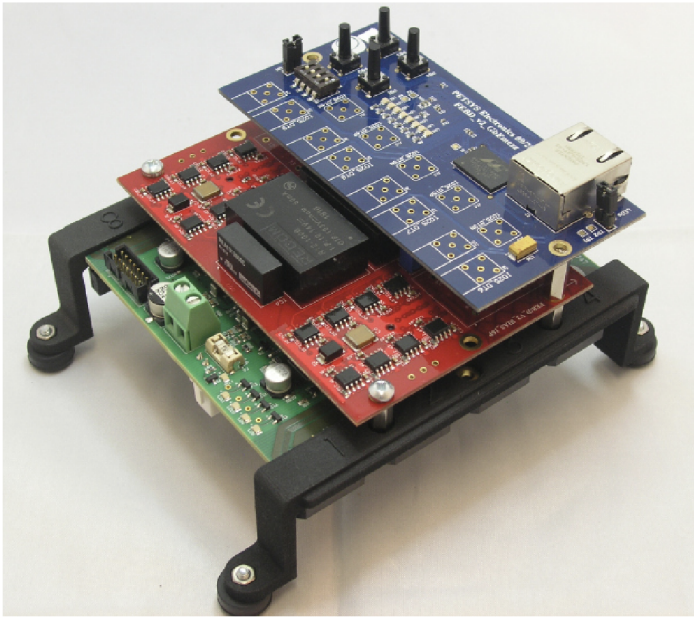


Figure 2.17: PETsys FEB/D consists of a communication mezzanine (in blue), a bias voltage mezzanine (in red) and data acquisition board equipped with Kintex7 FPGA (in green) [21].

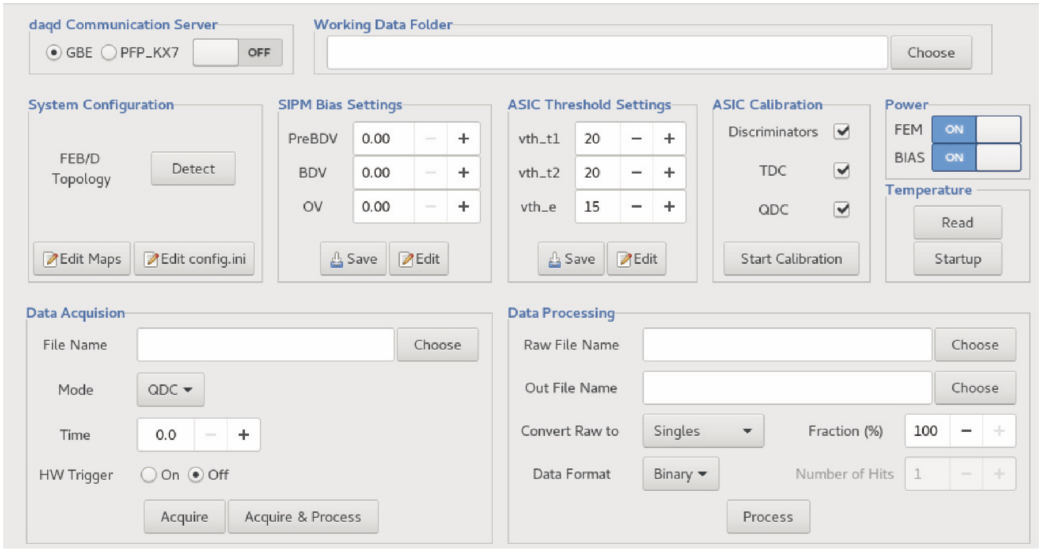


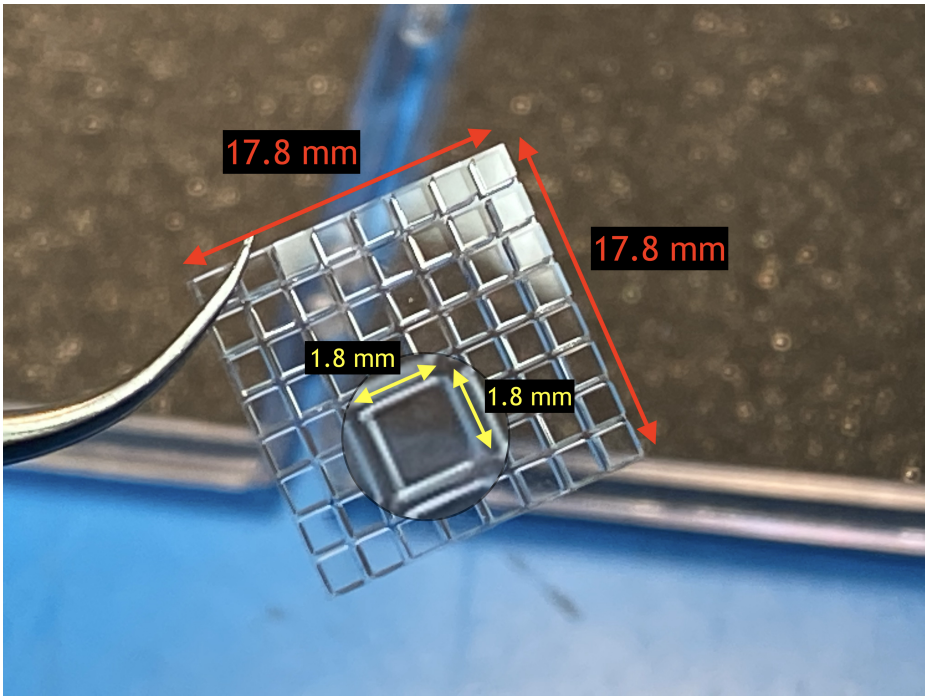
Figure 2.18: PETsys graphical user interface for data acquisition controls [21] .

modules [21]. The data output of each ASIC uses 4 LVDS data lines at up to 800 Mbps per data line [21]. Each event is encoded in 80 bits [21]. The maximum rate between the FEM128 and the FEB/D is about 500 *kcps* per channel [21].

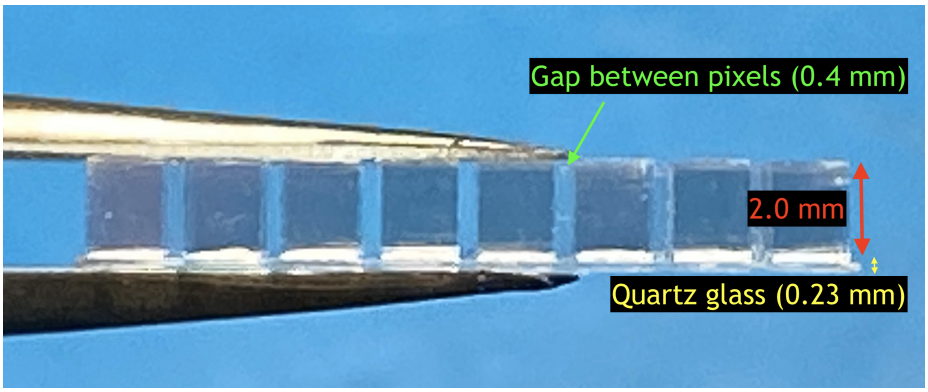
The FEB/D board consists of a Kintex-7 FPGA, a communication mezzanine and a bias voltage mezzanine [21]. The communication mezzanine has an SFP+ port for data output to the DAQ and for receiving the configuration signals [21]. The SFP+ port operates at 6.6 Gbits/s, allowing a maximum event output rate of 100 $Mcps$ [21]. There is also a Gbit Ethernet port that is available in the communication mezzanine, and the maximum data output rate to the computer is 15 $M\ events/s$[20]. The bias voltage mezzanine provides bias voltages in the range of $0-72\ V$. A $12-V_{DC}$ external supply voltage is needed to power up the FEB/D board [20]. The firmware installed in the FEB/D board allows for direct and online access to the PETsys TOFPET2 ASIC configuration, the bias voltage configuration, the temperature sensor readout and the raw TOFPET2 ASIC data [20]. A graphical user interface is provided for the data acquisition controls such as the SiPM bias settings, ASIC threshold settings, data acquisition mode and output data format [20]. The readout system can also accept an external signal to provide synchronization with other systems [21].

2.3.4 Full Detector Assembly and Operational Settings

For the second prototype, we expanded the scale of the first prototype from 64 to 256 channels, increasing the detector area from $16 \times 16\ mm^2$ to $35.6 \times 35.6\ mm^2$. The scintillator used for the second detector prototype remains the same as the scintillator in the first prototype, namely GS20 from Scintacor. Each element in the scintillator array is $1.8\times1.8\times2.0\ mm$ in size. All surfaces of each scintillator element have polished finishes. The scintillator elements were aligned at a pitch of 2.2 mm, following the pitch of the SiPM array. There was a gap of 0.4 mm between adjacent scintillator elements. These scintillator elements were then glued to a thin piece of 0.23 mm thick quartz glass to form a $17.8 \times 17.8 \times 2.25\ mm$ scintillator array. A thin piece of quartz was used as a support for the alignment of the scintillator array. Because the peak

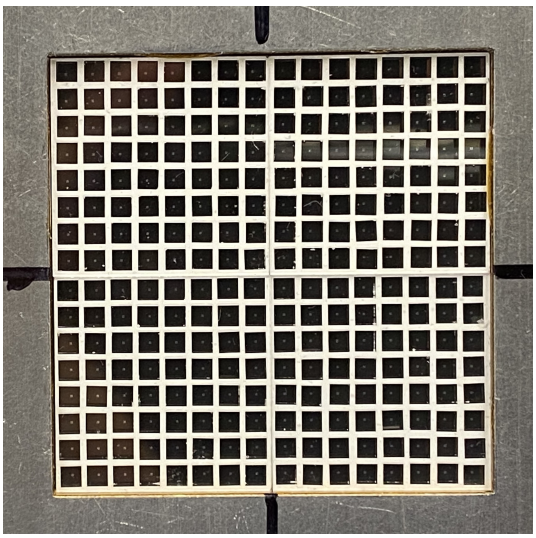


(a)

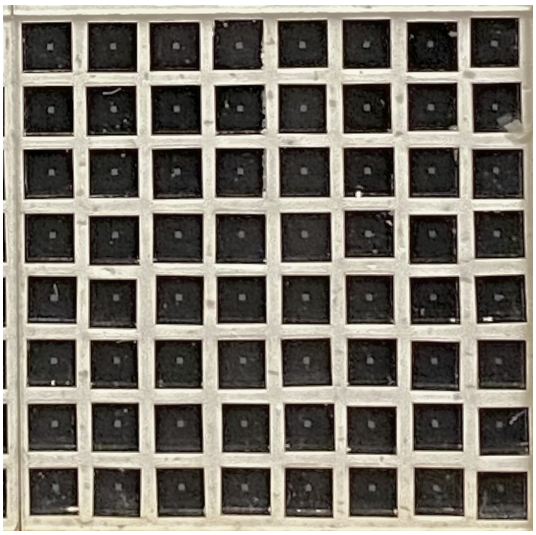


(b)

Figure 2.19: Photos show (a) the front view and (b) the side view of the scintillator array.



(a)



(b)

Figure 2.20: (a) A customized aluminum fixture is used to center each scintillator element to each SiPM and hold them in place. (b) A zoom-in view of the pixel shows that the scintillator elements are centered at each individual SiPM.

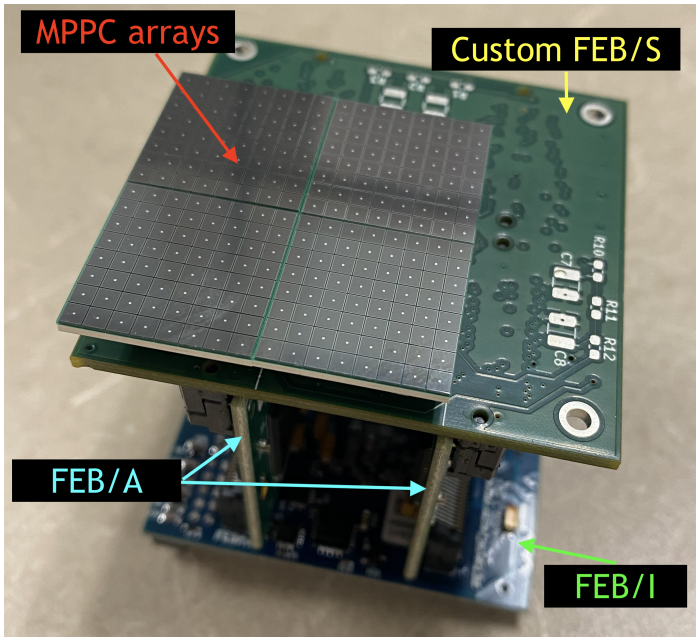
emission wavelength is around 395 mm for GS20, the Norland Optical Adhesive 88 (NOA 88) [65] was used because it is transparent in the UV range. The scintillator arrays were fabricated by our collaborator (IRD Glass), shown in Figure 2.19.

To prevent crosstalk across adjacent pixels, a reflective coating was applied to all surfaces but the top and bottom surfaces. One uncoated side was coupled to the SiPM and the other uncoated side was attached to a piece of Gore Teflon tape. For the first prototype, BC 620 was used as a reflector paint for the GS20 scintillator array. The reflectivity of BC-620 at 395 nm is around 90%. For the second prototype, Avian-B white reflectance coating. [75] was used instead because it has a higher reflectivity at the scintillator peak emission wavelength. An aluminum fixture was custom-made to hold the scintillator arrays in place as shown in Figure 2.20. No optical coupling was sandwiched between the scintillator arrays and the photodetectors.

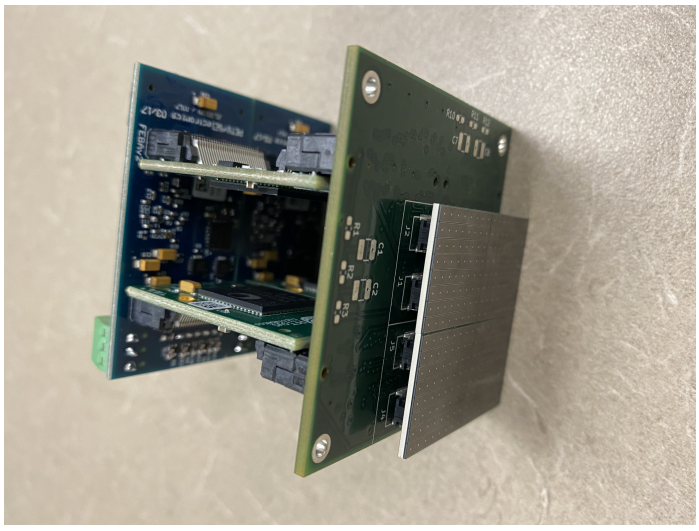
The photodetectors used were the Hamamatsu S13361-2050AE-08 MPPC arrays. Each individual channel of MPPC was read out independently. To integrate MPPC arrays to the PETsys readout system, the FEB/S board had to be redesigned because the SiPM arrays used are different models and cannot be directly mounted to the original FEB/S board, as shown in Figure 2.21. The custom FEB/S was then connected to FEM128 modules and the rest of the PETsys SiPM readout system. The PETsys system was synchronized with the accelerator pulses to obtain accurate neutron time-of-flight measurements.

During data acquisition, a bias voltage of 53 V with an overvoltage of 4 V was applied to all SiPMs. The ASIC threshold settings were individually adjusted for each channel using the charge integration (QDC) mode in a flood field acquisition.

A Gbit Ethernet was used for data transfer. The output data was stored in binary form. Each event has time, energy and pixel ID information. The PETsys readout was synchronized with an external system such that only events during the accelerator pulse period were collected. A complete assembly of the detector is shown in Figure 2.22. The detector consists of two partitions. The top partition consists of the data acquisition board (FEB/D), an external timing module, a $12-V$ voltage power supply

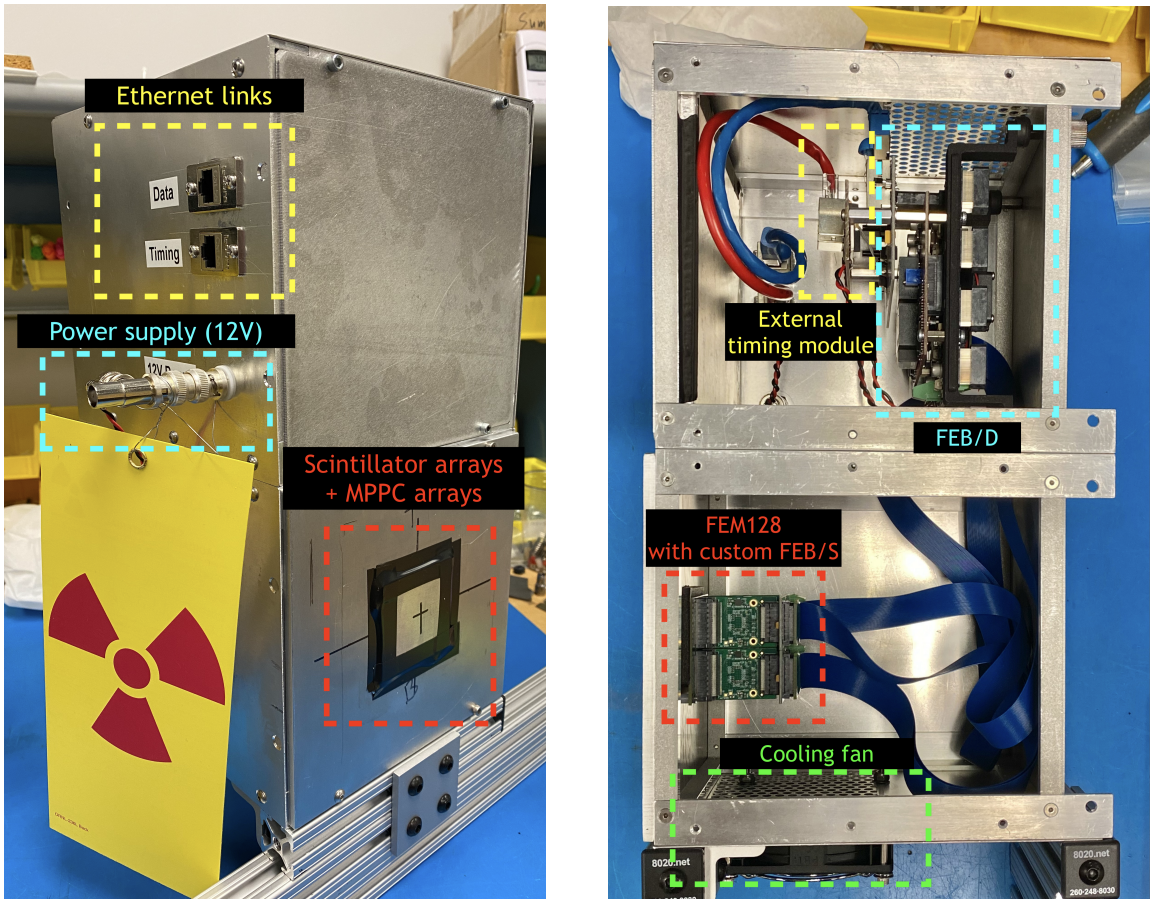


(a)



(b)

Figure 2.21: Photos show (a) the front view and (b) the side view of the custom sensor array designed to connect four 8×8 Hamamatsu S13361-2050AE-08 SiPM arrays to the PETsys SiPM readout system.



(a) **(b)**

Figure 2.22: Photos show (a) the exterior and (b) the interior of the complete detector assembly.

and Ethernet links. The bottom partition contains the scintillator arrays, SiPM arrays, the front end boards (FEM128) and a cooling fan. The detector is partitioned as such to minimize the exposure of the readout system in the direct beam during acquisition. There have been a number of upgrades from the first prototype to the second prototype as summarized in Table 2.7.

Table 2.7: Changes made in the second detector prototype

Changes	First prototype	Second prototype
Detector area (mm^2)	16×16	17.8×17.8
Active area per pixel (mm^2)	1×1	1.8×1.8
Dead space per pixel (mm^2)	1×1	0.4×0.4
Pixel pitch (mm)	2.0	2.2
Number of channels	8×8	16×16
Dimension of a scintillator (mm^3)	$2.0 \times 2.0 \times 2.0$	$1.8 \times 1.8 \times 2.0$
Presence of substrate glass	None	Quartz
Scintillator array manufacturer	ORNL	ORNL + IRD Glass
Reflective coating	BC-620 (TiO_2)	Avian-B ($BaSO_4$)
Reflectance (%)	90	97
Thickness of reflective coating (mm)	0.1-0.2	0.4
SiPM model	SensL ArrayC-10035064P-BGA SiPM	Hamamatsu S13361-2050AE-08 MPPC array
Photosensitive area per pixel (mm)	1.0	2.0
Dead space per pixel (mm)	1.0	0.2
Pixel pitch (mm)	2.0	2.2
Photon detection efficiency (%)	31	40
Dark count rate (kHz)	30	300
Bias voltage + Overvoltage (V)	27.5	57
SiPM readout system	CROC board	PETsys Readout System
Signal processing	Time-over-threshold	Charge integration
Time-of-flight	not supported	supported
ASIC	-	TOFPETv2
Number of channels per modules	64	128

Chapter 3

Detector Characterization

3.1 First Detector Prototype

Multiple tests were performed on the first detector prototype at Missouri University Research Reactor (MURR), High Flux Isotope Reactor (HFIR) and our detector development lab space in SNS. At MURR, the Double-Axis Powder Diffractometer (2X-C) and the High-Resolution Neutron Powder Diffractometer (PSD) beam lines were used. The neutron wavelengths at PSD and 2X-C were 1.48 Å and 2X-C, respectively. At HFIR, some additional tests were repeated at the Instrument Development Beamline (CG-1A) beam line. The neutron wavelength at CG-1A is 4.22 Å. In our detector development lab at SNS, the detector was tested with a moderated ^{252}Cf neutron source as well as a calibrated ^{60}Co γ source. The ^{60}Co main photon energies with their relative intensity are 1.173 MeV (99.85%) and 1.332 MeV (99.98%).

3.1.1 Neutron Detection Efficiency

The detector efficiency test was performed at the PSD beamline in MURR and CG-1A in HFIR. The detector was placed on a motorized stage and was positioned using the motorized stage to a location with the highest neutron flux possible, at a fixed

distance away from the beam port. The beam was collimated to a size of $1 \times 1\ cm$ using a collimation plate and two collimation slits.

In order to calibrate the neutron flux, a $1 - inch$ diameter ^{3}He gas detector filled with 8 bar of ^3He and 1 bar CF_4 was used to measure the neutron flux. The ^3He detector was assumed to have a detection efficiency close to 100% at the neutron wavelengths of the beam lines [7, 26]. To ensure that the intensity of the neutron beam did not saturate the ^3He detector, the beam was attenuated with an $8 - mm$ thick polyethylene attenuator. The measurements were repeated for the pixelated detector and the ^3He detector at the same location for the same amount of collection time with the same beam collimation and attenuation.

The relative detection efficiency, ϵ can be calculated by taking the ratio of the number of counts measured by the pixelated detector, $N_{pixelated}$ over the number of counts measured by the ^3He detector, $N_{^3He}$. These two quantities need to be background-subtracted prior to taking the ratio.

$$\epsilon = \frac{N_{pixelated}}{N_{^3He}} \tag{3.1}$$

The relative detection efficiency of the pixelated detector measured was 74% at 1.48 Å and 92% at 4.22 Å.

3.1.2 Counting Rate and Linearity

The counting rate and linearity tests were carried out at PSD in MURR and CG-1A in HFIR. The detector was again positioned using the motorized stage to a location with the highest neutron flux possible, a distance away from the beam port.

To measure the maximum counting rate capability of the detector, it is important to observe any detector count rate saturation with increasing neutron flux. Multiple attenuators of varying thicknesses were used to attenuate the neutron flux to different intensities. A fission monitor, that has a very low detection efficiency, was used as a reference during the test to observe any count rate saturation on the detector of

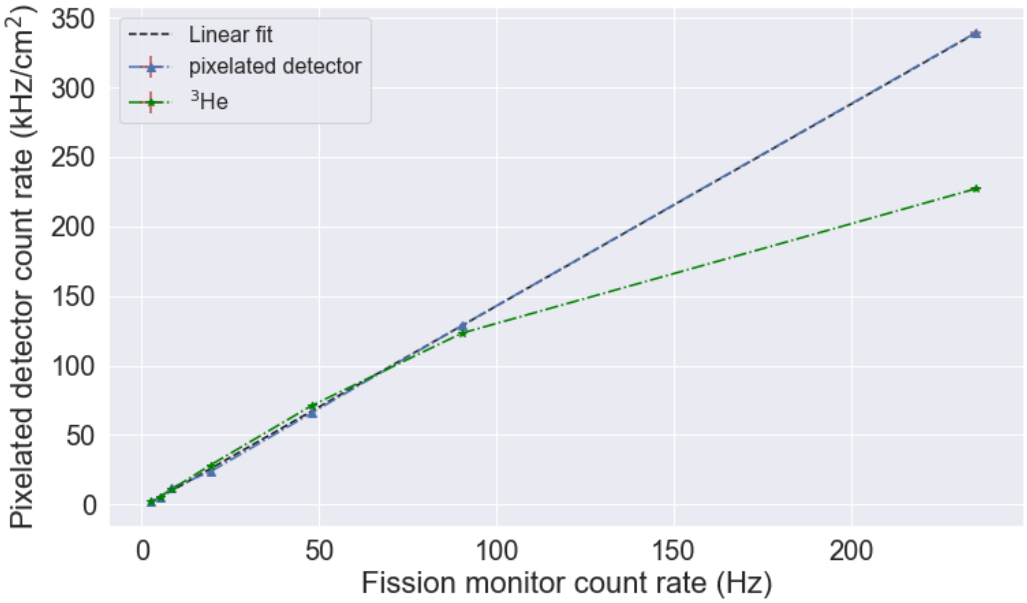
interest. It was assumed that the fission monitor does not saturate even at the highest neutron flux due to its low detection efficiency. The test was repeated for both the pixelated detector and a ^3He detector at the same location for the same irradiation period.

Figure 3.1 shows the results of the counting rate tests conducted at PSD, MURR and CG-1A, HFIR. Each data point in the plot was obtained using two detector measurements (fission monitor and the detector of interest) at the same neutron flux using the same set of attenuators. The leftmost data point was measured when the neutron flux was attenuated by the most number of attenuators (most attenuated beam), and the rightmost data point was measured when the neutron flux was at its highest flux possible without any attenuators (unattenuated beam).

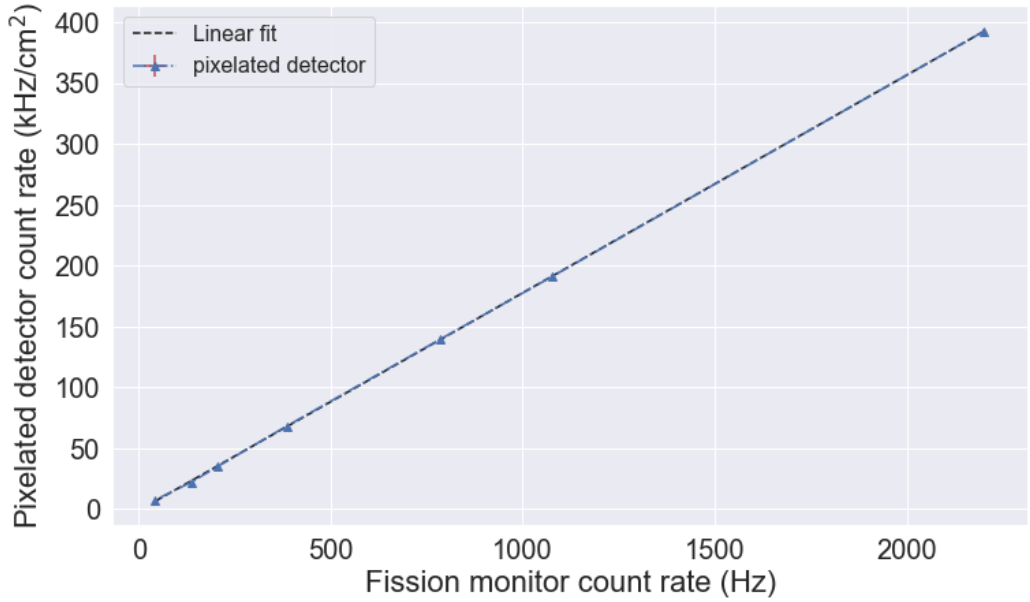
Figure 3.1a shows that the pixelated detector exhibits a linear response with increasing fission monitor rate, up to about 350 kHz/cm^2. This shows that the count rate of the pixelated detector still increases with increasing flux, and the linear trend with respect to the fission monitor rate shows that there were no signs of saturation up to the maximum measured rate. Meanwhile, the ^3He detector shows an increasing count rate with increasing flux, but the deviation from the linear trend with respect to the fission monitor rate suggests that the ^3He detector experienced count rate saturation and showed a considerable dead time at unattenuated beam intensity. The same test was repeated at CG-1A, HFIR and Figure 3.1b shows that the count rate of the pixelated detector was linear up to about 400 kHz/cm^2. These results not only demonstrate that the pixelated detector outperformed the ^3He detector in terms of counting rate, but also imply that further tests with a more intense beam are needed to determine the counting rate limit of the pixelated detector.

3.1.3 Crosstalk

Since the SiPM detector is pixelated, an examination of the crosstalk between pixels is also important as crosstalk can lead to double counting of neutron events. In the first prototype, each channel can be triggered as long as the pulse height of the signal is



(a)



(b)

Figure 3.1: (a) Counting rate test at PSD, MURR (b) Counting rate test at CG-1A. HFIR.

above a certain voltage threshold. Post-processing of the ToT spectrum may further minimize the crosstalk between detector pixels.

When a neutron is captured by ^6Li, the reaction products (2.05 MeV α and 2.73 MeV tritium) are produced. Given that α particles have an absorption length of $5-10$ μm, tritium has an absorption length of $40-150$ μm in GS20 and there is a $0.1-0.15$ mm spacing between scintillator elements for the first detector prototype, it is possible that the reaction products can deposit a fraction of the kinetic energy across multiple scintillator elements, thereby initiating scintillation in multiple pixels. It is possible for optical crosstalk to happen when the scintillation photons escape from one scintillator element to the other. Electronic crosstalk can also occur when there is unwanted electromagnetic coupling/interference between independent signal paths in the SiPM arrays and the readout system.

To measure the detector overall crosstalk, a piece of borated aluminum with a $1-mm$ diameter hole was centered over four different pixels, one at a time, as shown in Figure 3.2. The crosstalk between pixels was estimated using the change in count rates between the first and second nearest neighbors. The crosstalk was estimated to be less than 3%, which is the lower limit of sensitivity of the measurement technique.

3.1.4 Spatial Resolution and Uniformity

Because the scintillator material used in this detector is not contiguous, but rather, segmented, it is important to understand how the segmentation of the scintillator affects the spatial resolution and uniformity of the detector. The spatial resolution and uniformity tests were conducted at the 2XC beam line, MURR. To conduct such measurement, the detector was scanned linearly in one direction with a 0.5 mm step size using a collimated neutron beam. The neutron beam was collimated using a piece of borated aluminum with a slit width of 0.85 mm. It is assumed that the uniformity is similar in both directions. The detector was placed about 163 cm away from the beam port to ensure a flat neutron field.

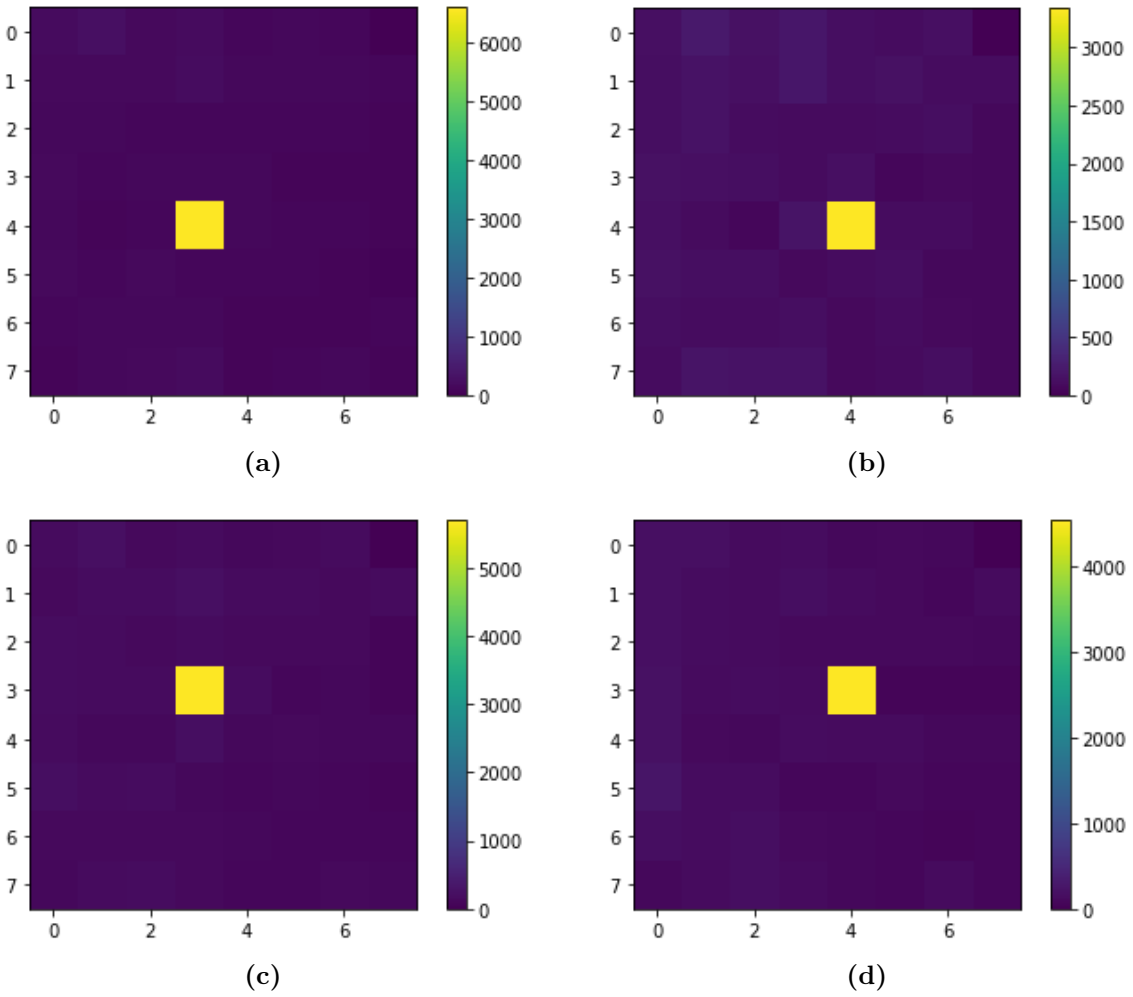


Figure 3.2: Crosstalk measurement results over pixel (a) 28 (b) 29 (c) 36 (d)37.

The measurement was performed using individual readout, so no interpolation was performed to reconstruct the location of a neutron event. It is expected that the spatial resolution of the detector is primarily determined by the pitch of the pixelated detector because the track length of the reaction products is much smaller than the pixel pitch. Figure 3.3 shows the relative intensity as a function of the position. At maximum, the 0.85 mm wide neutron beam overlapped fully within the 1 mm active area. At minimum, the slit was in between the pixels. The overall variation in relative intensity across the pixels is about 6.5%, well within 10%.

3.1.5 Gamma Sensitivity

The gamma sensitivity is defined as the ratio of the number of counts measured using the detector, $N_{detected}$ to the number of counts emitted from the gamma source, $N_{emitted}$, given the solid angle subtended by the detector from the gamma source. It is also the absolute γ efficiency.

$$\gamma - sensitivity = \frac{N_{detected}}{N_{emitted}} \tag{3.2}$$

For the γ-sensitivity test, a calibrated ^{60}Co source was used. The calibrated ^{60}Co has an initial activity, A_o of 10 μCi dated 08/01/2017. ^{60}Co has a half-life of 5.27 $years$ and a decay constant, λ of 0.1315 $years^{-1}$. By taking the time elapsed, t since A_0 was measured, the activity of ^{60}Co at the time of measurement can be calculated.

$$A = A_0 e^{-\lambda t} \tag{3.3}$$

The solid angle, ω subtended by a rectangular area of size $l \times b$ at any point lying on the perpendicular axis at a distance, d away from the center of the source is given by:

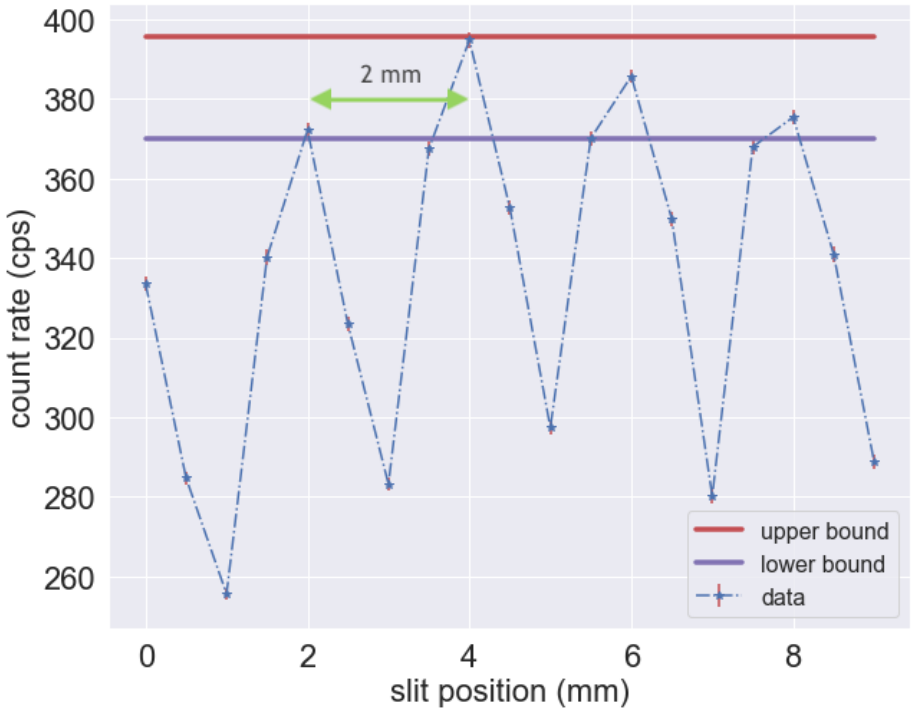


Figure 3.3: Simulated result versus experimental result for linear scan measurement

$$\omega = 4sin^{-1}\left(\frac{lb}{\sqrt{(l^2+4d^2)(b^2+4d^2)}}\right) \tag{3.4}$$

Given the detector of size $1.6 \times 1.6\ mm^2$ was positioned $d = 3\ cm$ away from the source, the solid angle can be calculated using Equation 3.4. The γ-sensitivity of the detector was measured to be 1×10^{-3} with just pulse height discrimination.

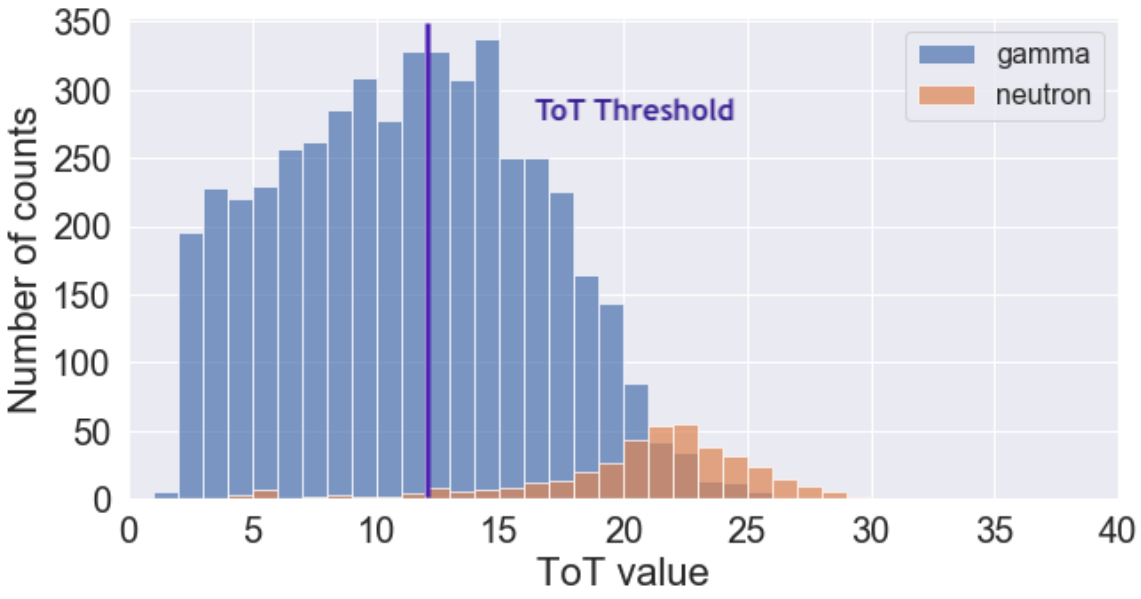
With the Time-over-Threshold (ToT) method, the γ-sensitivity was further reduced by 1 order of magnitude by setting a threshold on the ToT spectrum in post-processing. Figure 3.4 shows an example that placing a threshold in the ToT spectrum can further discriminate between neutrons and γ-rays with the tradeoff of losing a small fraction of the neutron events.

The ability to discriminate neutrons from gamma is better when using a different SiPM with a larger active area. The SiPM is the SensL ArrayC 60035-64P-PCB, which will be referenced as the "6 mm SiPM". Since a different SiPM model was used, it is difficult to pinpoint the exact cause of a difference in neutron-γ discrimination capability. One stark difference was the percentage of active area per pixel. As previously mentioned, the active area of the SensL ArrayC 10035-64P-BGA, referenced as the "1 mm SiPM", is about 25% of a whole pixel and the active area of the 6 mm SiPM is about 70% of a whole pixel. Further investigation is needed before coming up with a substantiated claim.

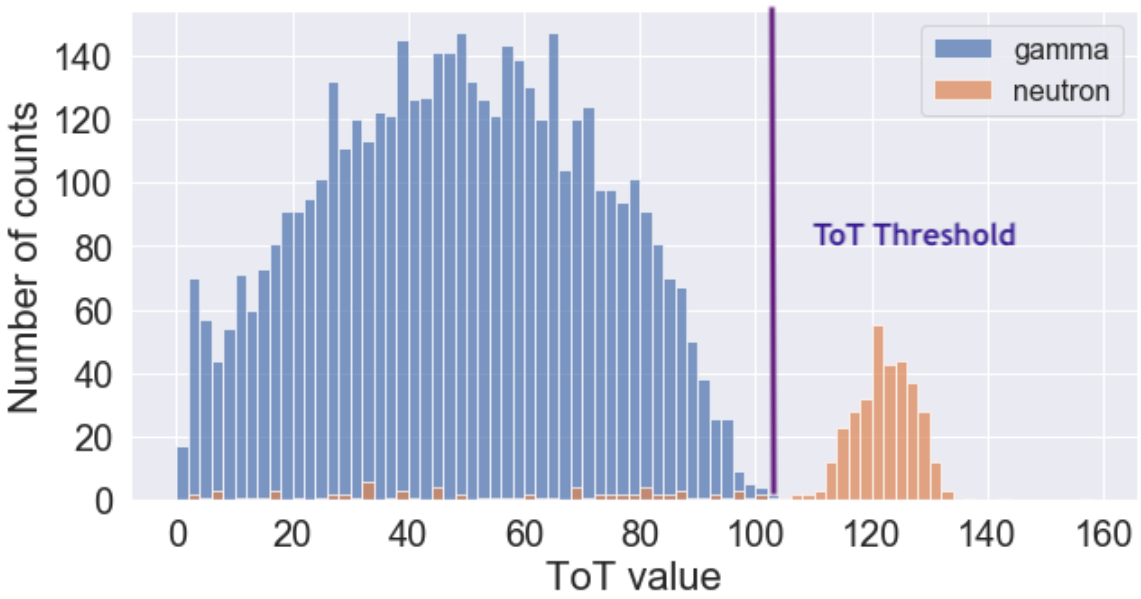
3.1.6 Summary

Table 3.1 summarizes the results of the tests performed on the first detector prototype. The performance of the detector proves to be a promising alternative to the MWPC detector for neutron reflectometry instruments at the SNS.

The counting rate capability of the pixelated detector was demonstrated to be better than a single ^3He detector, which has a higher counting rate than the MWPC detector. This is a major advantage of the pixelated detector, which eliminates the bottleneck of the MWPC detector in rate capability. It should be emphasized that



(a)



(b)

Figure 3.4: Time-over-Threshold spectrum of neutron peak and gamma peak obtained using (a) 1 mm SiPM (b) 6 mm SiPM.

a more intense neutron source is needed to determine the maximum counting rate of the pixelated detector. In terms of detection efficiency and spatial resolution, the detector prototype has met the detector requirements for reflectometry instruments.

The active area of the first detector prototype is 1.6. $\times$ 1.6 cm^2. The detector needs to be scaled up to a larger active area. The detector assembly did not make scaling up the detector system easy. The re-assembly of the detector in a scalable fashion was proposed for the second detector prototype. A complete replacement for a more compact and scalable readout solution is also another alternative.

The γ-sensitivity was higher than desired, but it is expected given the intrinsic characteristics of the scintillator. GS20 inherently has a higher sensitivity towards γ-rays. It has been shown that with a different readout technique such as the Anger logic, the γ-sensitivity can be reduced. However, the Anger logic method will not provide as high of a counting rate ability as the individual readout method. The same applies to other charge division readouts. There exists a tradeoff between the counting rate capability and γ-sensitivity of the detector. Another suggestion for minimizing the γ-sensitivity of the detector was to reduce the thickness of the scintillator. The current thickness of the scintillator is 2 mm, which gives about 95% efficiency for thermal neutron capture. Reducing the scintillator thickness to 1 mm reduces the efficiency to 75%. This presents a tradeoff between γ-sensitivity and neutron detection efficiency. To overcome the tradeoff, it is possible to orient the scintillator elements at an angle to improve the efficiency of neutron capture. Such a design may present engineering challenges in the fabrication of the scintillator arrays. These are worth investigating to achieve optimal detector performance for neutron reflectometry.

3.2 Second Detector Prototype

Due to significant changes made in the second detector prototype, it is important to characterize the performance of the detector with existing changes. Similar tests previously performed on the first detector prototype were repeated on the second

Table 3.1: Summarized result for performance evaluation of first detector prototype.

Parameters	Results
Counting rate (kHz/cm^2)	≥ 392
Neutron efficiency relative to ^{3}He detector (%)	75 (for 1.8 Å)
	92 (for 4.2 Å)
Gamma sensitivity	1×10^{-3}
	1×10^{-4} (with ToT)
Spatial resolution (mm)	2
Crosstalk (%)	≤ 3
Uniformity (%)	≤ 10
Active area (cm^2)	1.6×1.6

detector prototype. All the tests were performed at HFIR CG-1A, except for the γ-sensitivity test which was conducted at the SNS detector development lab.

3.2.1 Neutron Detection Efficiency

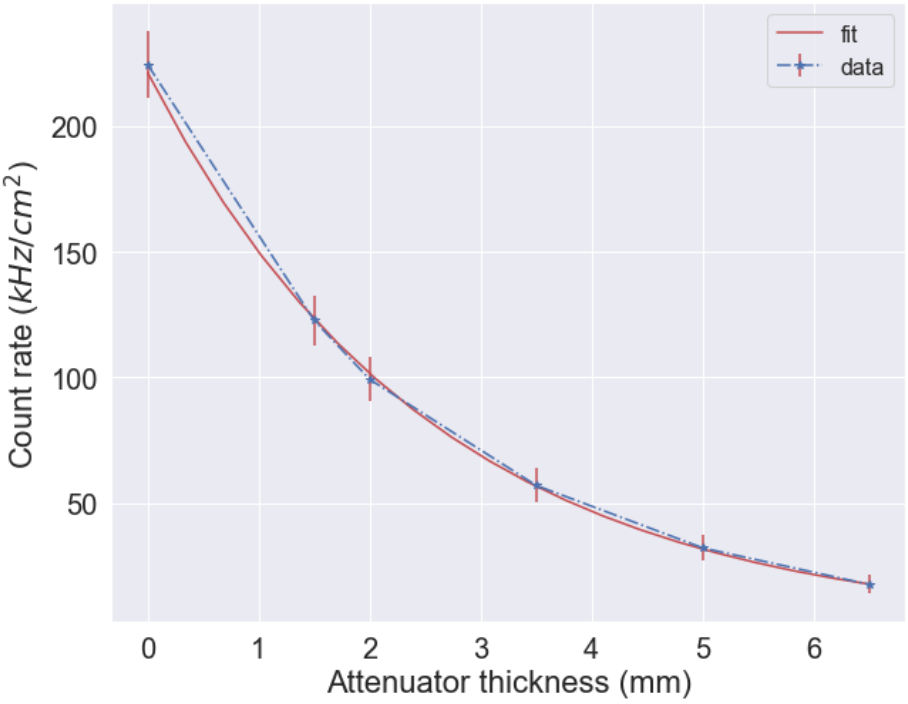
The procedure for measuring the detection efficiency of the detector is the same, as described previously. A ^3He detector was used as a reference and was assumed to be close to fully efficient (close to 100% efficiency). Both the pixelated detector and the ^3He detector were placed at the same location for the test with the assumption that the neutron flux was the same for both. Both measurements were 100 s long. The background was measured by each detector. The counts measured were background-subtracted before taking the ratio. The neutron detection efficiency of the detector was measured to be $62.71 \pm 0.15\%$.

3.2.2 Counting Rate and Linearity

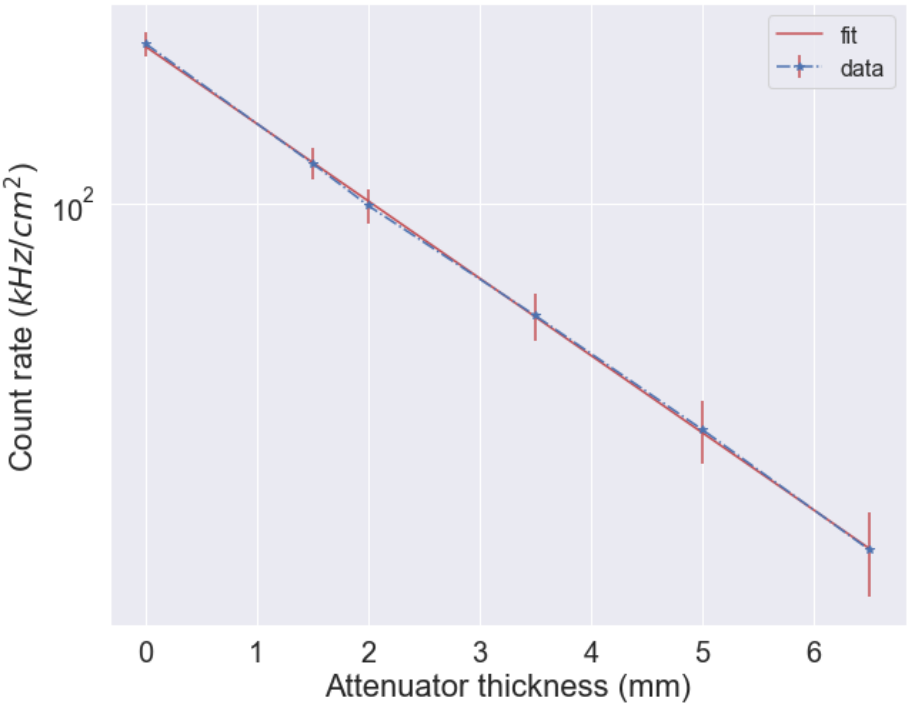
The count rate test performed was similar to the test performed on the first detector prototype, with the exception that a fission monitor wasn't used as a reference. As described previously, multiple attenuators were used to vary the intensity of the neutron flux for different measurements. The count rate of the detector was recorded at each measurement. A plot of the detector count rate as a function of the thickness of the attenuators is shown in Figure 3.5. It is expected that the count rate falls exponentially as a function of attenuator thickness, according to the Beer-Lambert law in Equation 3.5.

$$I = I_0 e^{-\mu x} \tag{3.5}$$

where I is the measured intensity (in this case count rate), I_0 is the initial intensity, μ is the linear attenuation coefficient of the attenuators, x is the thickness of the attenuator. The equation of fit is $y = 221.51\ e^{-0.39x}$, and the $R^2 = 0.9997$. As expected, the maximum counting rate capability of the pixelated detector cannot be



(a)



(b)

Figure 3.5: Plot of the count rate of the pixelated detector as a function of attenuator thickness. The equation of fit is $y = 221.51\ e^{-0.39x}$, and the $R^2 = 0.9997$.

determined at CG-1A as no signs of detector count rate saturation were observed. Hence, a more intense source was needed to find the count rate limit of the detector.

3.2.3 Crosstalk

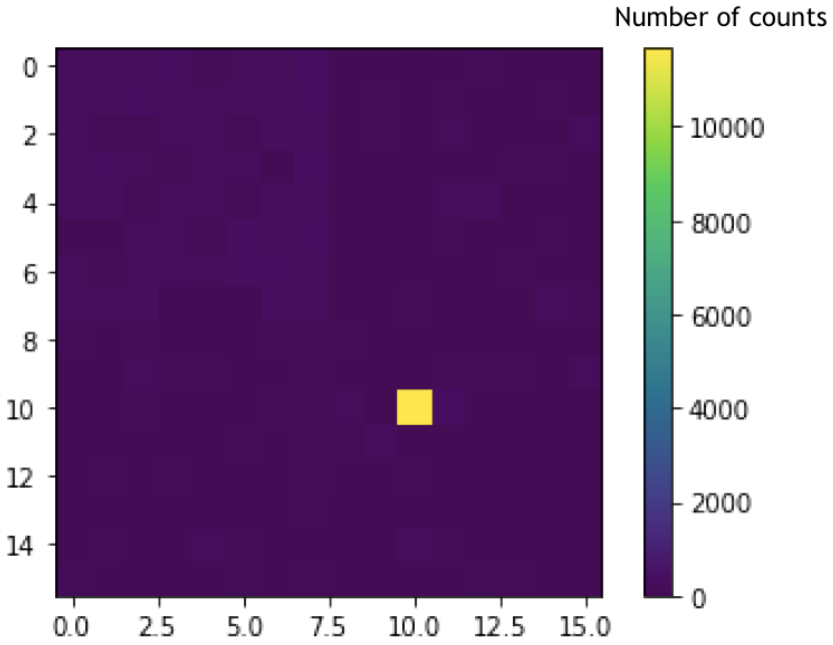
The same crosstalk test was repeated for the second detector prototype. A borated aluminum mask with a 1 mm-diameter pinhole was used to collimate the neutron beam to hit a single pixel, shown in Figure 3.6. The crosstalk was approximated using the percentage difference between the first nearest neighbors and the second nearest neighbors according to the following formula:

$$crosstalk\ (\%) = \frac{\bar{N}_{first\ nearest\ neighbors} - \bar{N}_{second\ nearest\ neighbors}}{N_{target\ pixel}} \times 100 \tag{3.6}$$

where $\bar{N}_{first\ nearest\ neighbors}$ is the average count in the first nearest neighbors, $\bar{N}_{second\ nearest\ neighbors}$ is the average count in the second nearest neighbors and $N_{target\ pixel}$ is the number of count in the target pixel. The first nearest neighbors are defined as the pixels that are one pixel away from the target pixel, and the second nearest neighbors are defined as the pixels that are two pixels away from the target pixel. The crosstalk was estimated to be $\leq 1\%$.

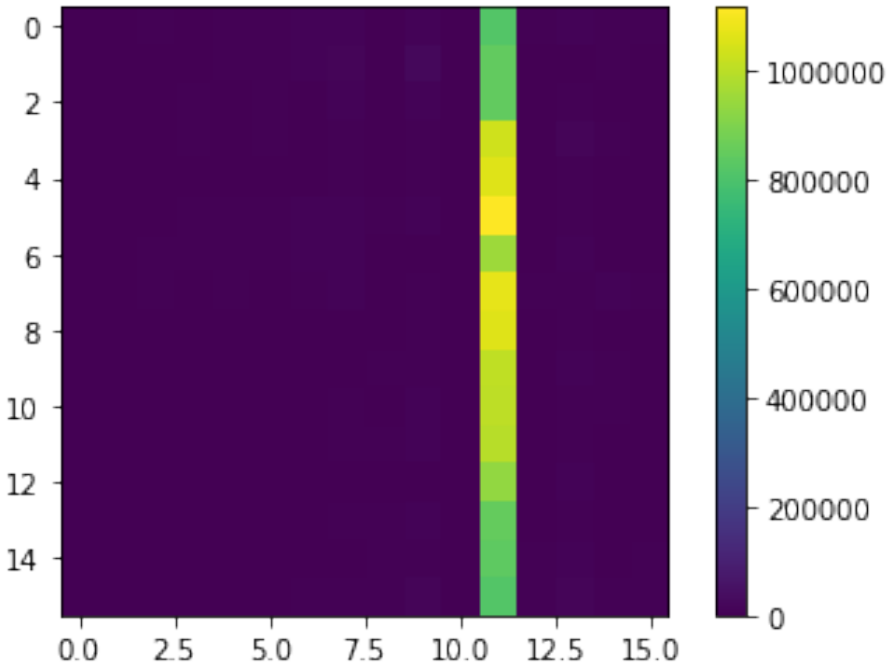
3.2.4 Spatial Resolution

The spatial resolution of the detector, as discussed previously, is largely determined by the pitch of the sensor array, 2.2 mm. To measure the spatial resolution of the detector, a borated aluminum mask with a slit width of 1.5 mm was used. To characterize the spatial resolution, a Gaussian curve was used to fit the cross-sectional profile of the measurements. When the 1.5 mm slit was positioned at the center of a pixel, only one column of pixels was illuminated shown in Figure 3.7a. Due to insufficient data points within the peak, a Gaussian curve was not fitted to the cross-sectional measurement. This shows that the spatial resolution of the detector is 2.2 mm. Figure 3.8 shows then the 1.5 mm slit was positioned slightly off-centered,

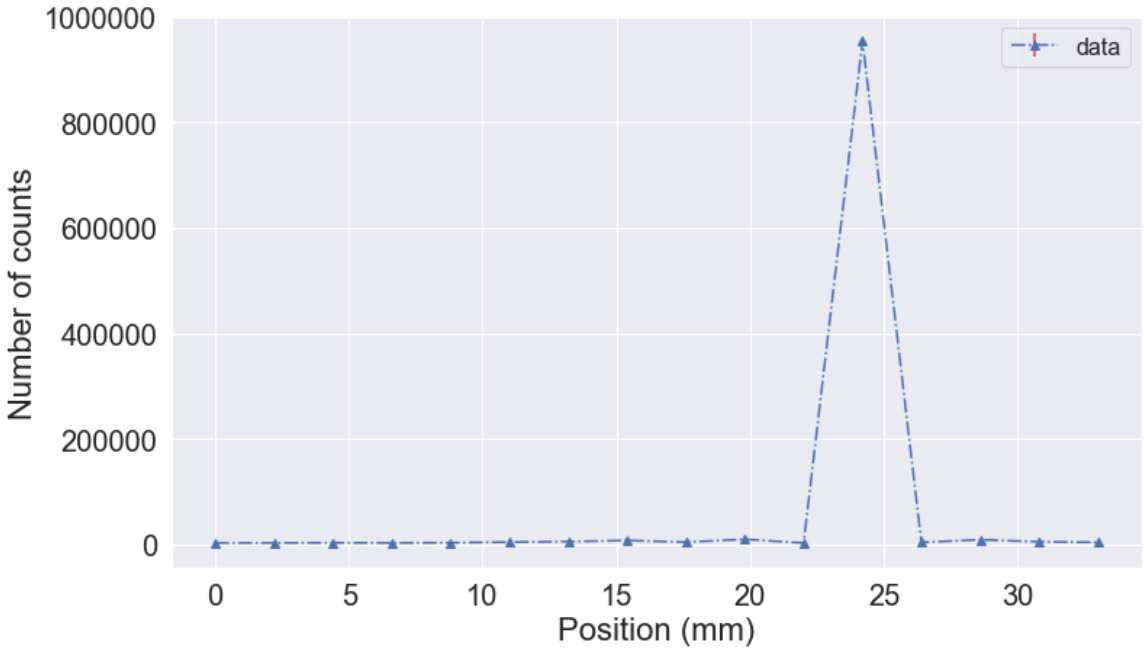


(a)

Figure 3.6: Crosstalk measurement over pixel 170.

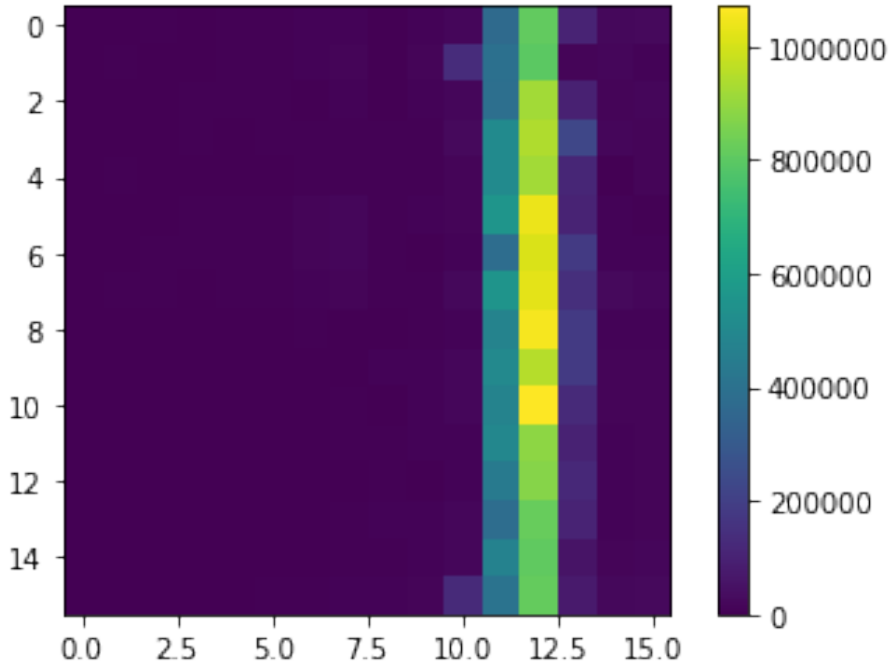


(a)

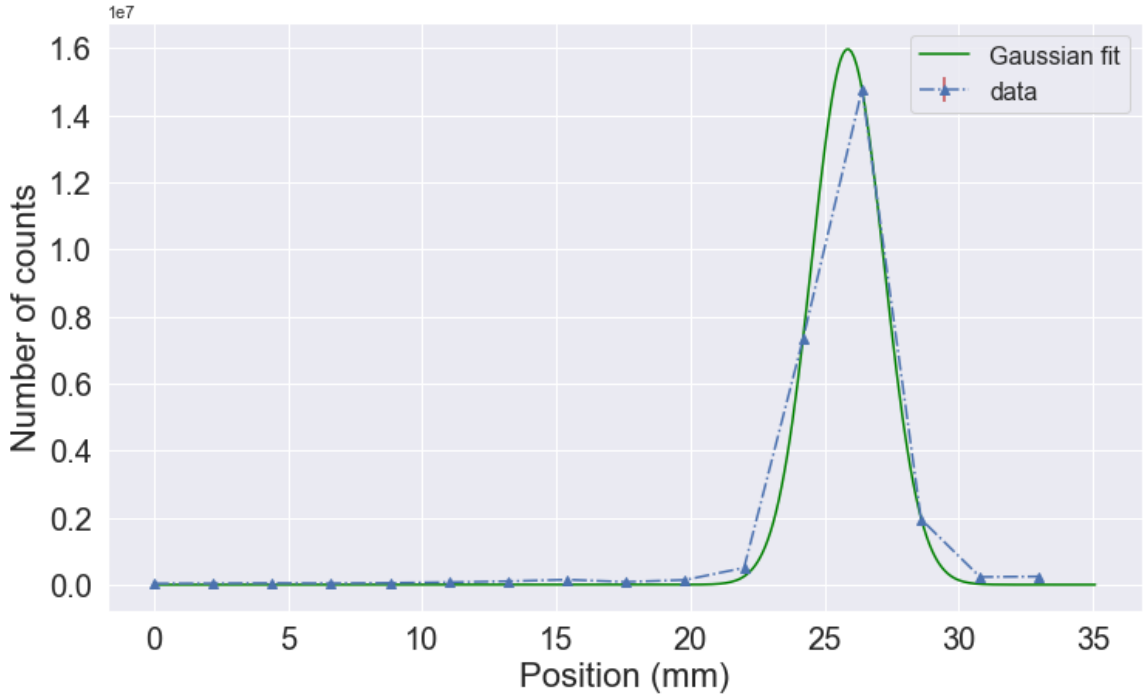


(b)

Figure 3.7: (a) The 2-D histogram and (b) cross-sectional profile of the measurements when a 1.5 mm slit was positioned at the center of a pixel.



(a)



(b)

Figure 3.8: (a) The 2-D histogram and (b) cross-sectional profile of the measurements when a 1.5 mm slit was positioned slightly off the center of a pixel.

more than 1 column was illuminated. A Gaussian curve was fitted to the cross-sectional profile of the measurement. The FWHM of the peak was approximated to be 3.15 mm, which is larger than the spatial resolution of the detector.

3.2.5 Gamma Sensitivity

The experimental procedure for the γ sensitivity test is detailed in the previous section. A calibrated ^{60}Co source was used to measure the γ sensitivity of the detector by taking the ratio of the number of γ events detected over the number of γ-rays emitted by the source with the solid angle subtended by the detector taken into consideration. The γ-sensitivity obtained was $\approx 10^{-2}$.

3.2.6 Summary

Table 3.2 summarizes the comparison in detector performance between the first prototype and the second prototype.

For the counting rate, both prototypes demonstrated that a more intense neutron source was needed to determine the limit of the detector rate capability. Even though the counting rate tests were done at the same beam line (HFIR CG-1A), the incident neutron flux at the beam line was not guaranteed to be consistent for those two measurements. Hence, the difference in the highest count rate measured by both detectors cannot be considered as degradation in performance.

Even with a higher percentage of active area per pixel and a higher photon detection efficiency for the second detector prototype, the neutron efficiency was lower than that of the first detector prototype. There are many factors that can affect neutron detection efficiency. The size of each scintillator element for the first prototype ($2 \times 2 \times 2$ mm^3) is about 23% larger than the size of the scintillator element ($1.8 \times 1.8 \times 2$ mm^3) for the second prototype. Hence, the neutron detection efficiency is expected to be lower. Another factor would be the discrimination threshold. The discrimination threshold has a direct impact on the neutron detection

efficiency because a lower threshold would register for more event counts. The first prototype used a pulse height discrimination threshold but the second prototype used a charge integration threshold. Hence, it is difficult to compare between two different discrimination thresholds.

The spatial resolution is largely determined by the pitch of the sensor array due to pixelation in the scintillator. Due to the discontinuation of the SensL SiPM, the next closest SiPM on the market (in terms of photon efficiency for our scintillator peak emission wavelength, number of pixels, pixel size and pixel pitch) was chosen. The Hamamatsu SiPM was the closest match found, and was a newly released product at the time of purchase.

The crosstalk between pixels was improved as the reflective coating between pixels was made thicker. A different reflective coating was used as it was better-suited for the emission wavelengths of the scintillator.

The active area of the detector increases by $4\times$ in the second detector prototype. The readout electronics for the first detector prototype were completely replaced by a commercial readout system from PETsys electronics. The replacement has made scaling up the detector to a larger system easy without significant modification to the existing electronics. This is a significant improvement compared to the first detector prototype.

The γ-sensitivity for the second prototype was two orders of magnitude higher than what was measured for the first detector prototype. Due to significant changes made to the photodetector and the readout system, it is difficult to pinpoint the root cause for the degradation in γ sensitivity. Further investigations will be required.

Table 3.2: Summarized result for performance evaluation of first and second detector prototype.

Parameters	First prototype	Second prototype
Counting rate (kHz/cm^2)	≥ 392	≥ 225
Neutron efficiency relative to ^{3}He detector (%)	92 (4.2 Å)	62 (4.2 Å)
	75 (1.8 Å)	
Spatial resolution (mm)	2.0	2.2
Crosstalk (%)	≤ 3	≤ 1
Active area (cm^2)	1.6×1.6	3.56×3.56
Gamma sensitivity	1×10^{-3} (PHD)	1×10^{-2} (QDC)
	1×10^{-4} (ToT)	

Chapter 4

Neutron Reflectivity Experiment

4.1 Counting Rate Test

Even though the pixelated detector has been previously characterized at HFIR CG-1A, the counting rate test had to be repeated at the SNS BL-4B. This is because the neutron flux profile at a spallation neutron source is vastly different from the neutron flux profile at a reactor, as discussed in Section 1.1.2. For the counting rate test, it is of particular interest to characterize the instantaneous count rate capability of the detector. For the neutron reflectivity experiments, it is important to evaluate the performance of the detector in actual experimental conditions.

4.1.1 Experimental Setup and Procedure

The pixelated detector, along with a beam monitor, were set up at SNS BL-4B as shown in Figure 4.1. A temporary hollow snout, which was made up of sheets of boron carbide (B_4C), was installed to prevent neutrons scattered off the beam slit from interfering with the reflectivity measurements. Additional borated aluminum neutron shielding was added around the pixelated detector and the beam monitor to minimize radiation damage to the detectors in high flux environments. To ensure that the detector was aligned with the instrument, a series of alignment tests were

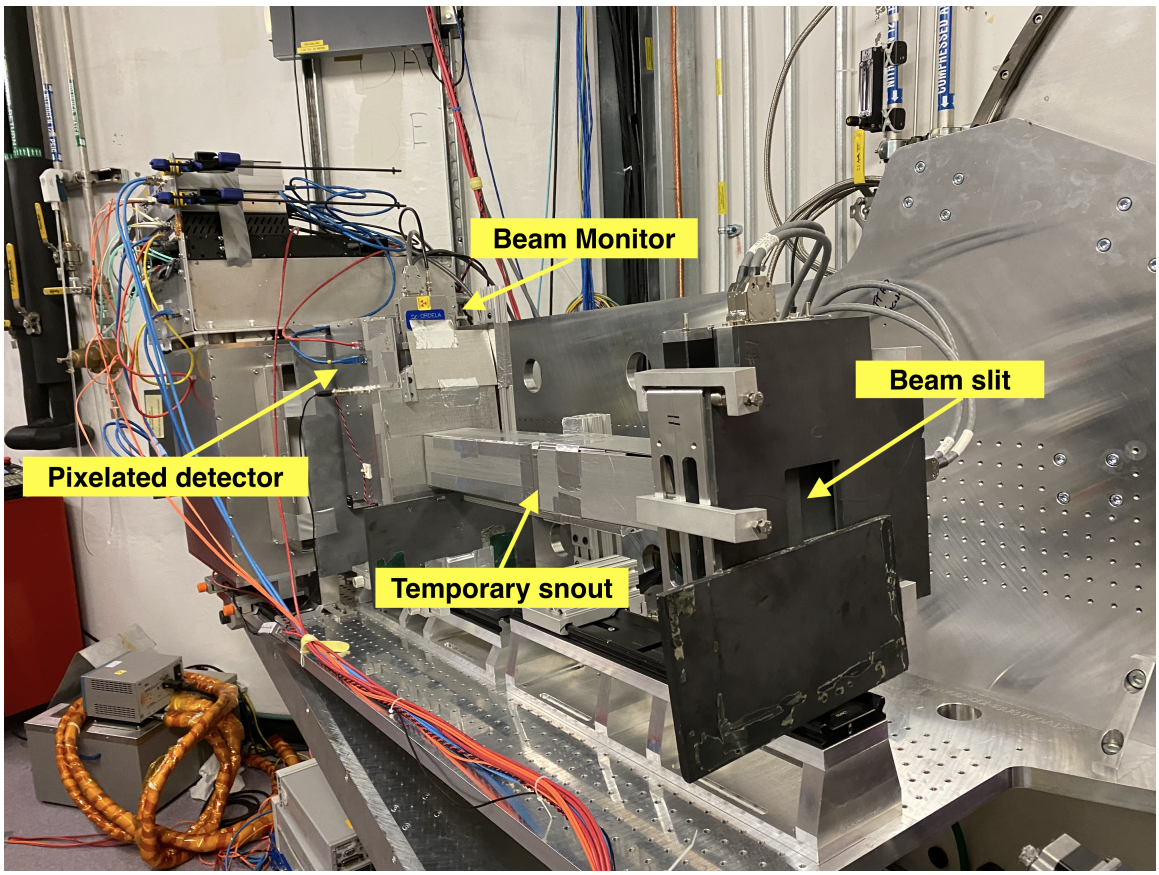


Figure 4.1: The pixelated neutron detector installed at the Liquid Reflectometer (BL-4B) for a neutron reflectivity experiment.

carried out by varying the angle of the sample while making sure that the reflected neutron beam could be seen on the detector at different angles.

To conduct the counting rate test, the instrument was adjusted such that the angle of the sample was set to 0^o. Measurements with a sample angle of 0^o will be called direct beam measurements because the detector is directly in line with the beam. The beam slit was set to 14×30 mm. To vary the neutron flux at the instrument, the number of attenuators (borated polyethylene) was varied at the beam port. Each attenuator was 5 mm in thickness. As a benchmark for linearity in count rate, a beam monitor (Ordela Model 4515-N-L) [55], which has a low neutron efficiency, was used. The count rate of the pixelated detector was compared with the count rate of the beam monitor to observe any signs of count rate saturation.

4.1.2 Results and Analysis

The pixelated detector showed a linear response in count rate with increasing neutron flux and no count rate saturation was observed at the maximum neutron flux available at the beam line, shown in Figure 4.2. The count rate is the global time-average rate. The global time-averaged rate is defined as the number of counts per second recorded in the total active area of the detector. This implies that even though the neutrons come in pulses, the count rate was averaged over the acquisition period. It should also be cautioned that even though the count rate is quoted for the whole detector, the neutron beam did not cover the entire active area of the detector. The highest global time-averaged rate measured at BL-4B is about 1.8 MHz.

What is of particular interest for this measurement is the instantaneous rate. The instantaneous count rate is defined as the number of counts recorded per the time bin in a single frame over the whole detector area. Since the detector was externally synchronized with the accelerator pulse, the frame rate was 60 Hz. Each frame is approximately 16.67 ms. In a single time frame, there are 814 time bins with a bin size of 20.48 μs. The instantaneous count rate can be calculated using the following equation:

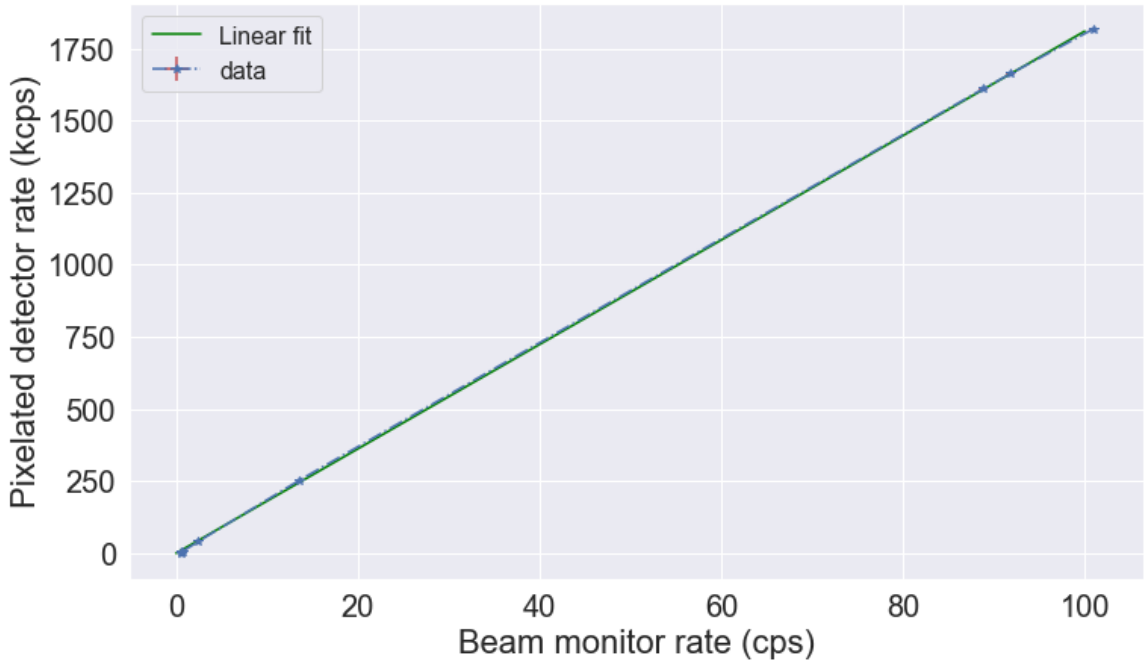


Figure 4.2: The graph shows the time-averaged count rate of the pixelated detector is plotted against the time-averaged count rate of the beam monitor. The pixelated detector shows a linear response in increasing count rate up to the maximum available flux. The equation of fit is $y = 18.1x - 0.307$ and the R^2 of the linear fit is 0.99995.

$$instantaneous\ rate = \frac{Number\ of\ counts}{bin\ size \times number\ of\ frames} \tag{4.1}$$

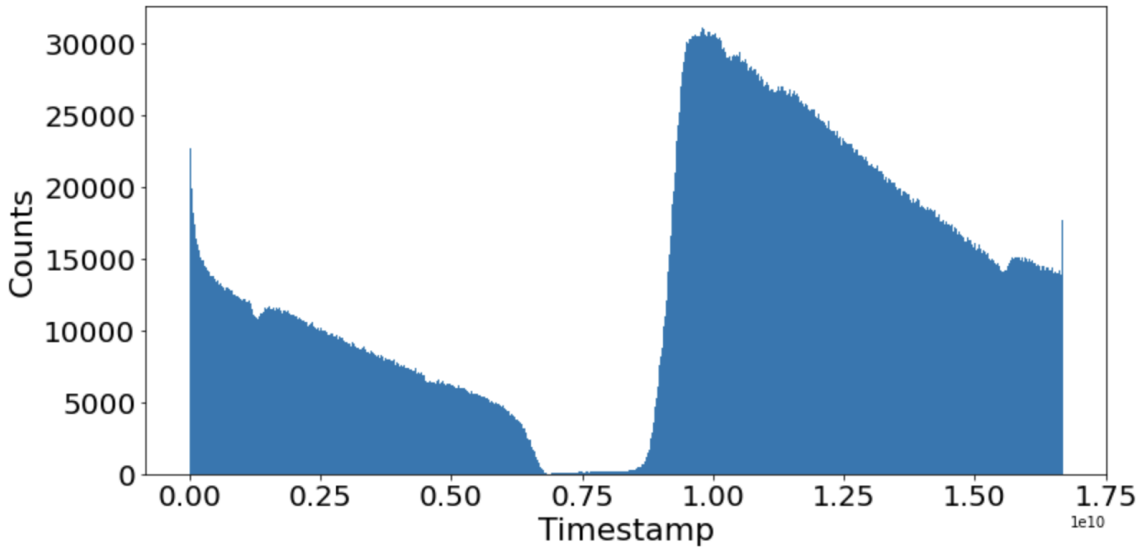
From Figure 4.3a, the highest number of counts per bin was 379499. The whole measurement was taken for 300 s. The number of frames is 300 $s \times 60\ Hz = 18000$. Plugging the numbers into Equation 4.1, the highest instantaneous rate of the detector was about 1.03 $Mcps$. To find the local instantaneous rate, individual pixels were investigated. The local instantaneous rate is defined by the instantaneous count rate per pixel. The highest local instantaneous rate was about 83.5 $kcps$ per pixel, which is equivalent to 17.3 $kcps/mm^2$.

4.1.3 Conclusion

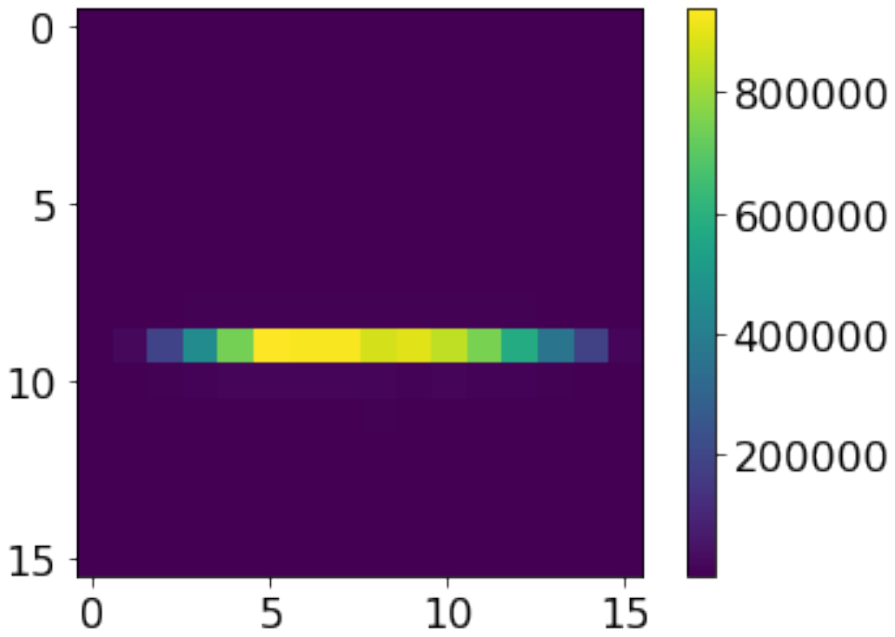
The outcome of the counting rate test was significant. The pixelated detector demonstrated a high counting rate capability with no dead time at the highest neutron flux setting (without any attenuators). The ability to make direct beam measurements without attenuators has never been achieved by the current detector, MWPC. This can not only drastically reduce the time needed for an experiment, but also overcome the bottleneck of rate-limited neutron reflectivity experiments.

4.2 Neutron Reflectivity Experiment

To demonstrate the practical performance of the detector, two neutron reflectivity experiments using the pixelated detector were conducted at the SNS BL-4B. Two standard samples, namely iridium on silicon wafer and quartz, were used. The quartz sample, shown in Figure 4.4, has a well-known critical angle, so it is a good choice for validation. The iridium on silicon wafer sample produces a reflectivity curve with well-defined interference fringes, so it is also a good candidate for validation.



(a)



(b)

Figure 4.3: The (a) Time-of-Flight (ToF) measurement and (b) the area plot of the detector count rate for the highest neutron flux setting.

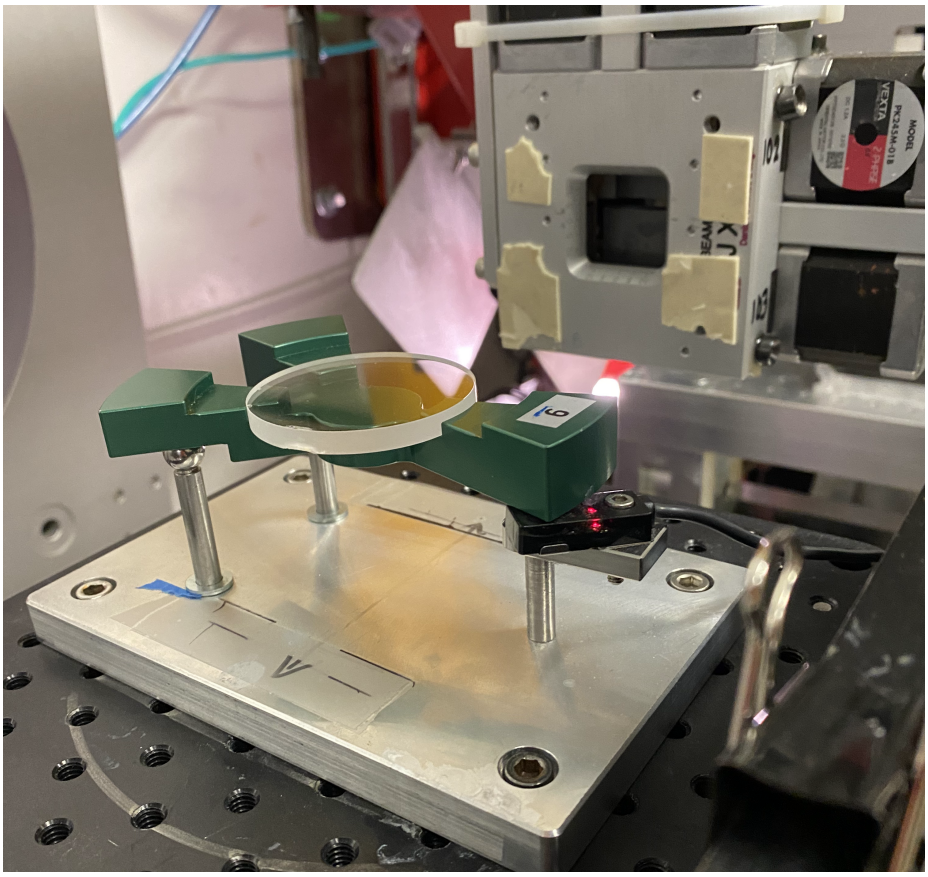


Figure 4.4: The quartz sample at the sample stage.

4.2.1 Experimental Setup and Procedure

A neutron reflectivity experiment consists of a set of measurements for direct beam and reflected beam. For each beam measurement at SNS BL-4B, there were 7 runs as 7 different instrument configurations were needed to get a full reflectivity curve over a range of scattering vectors (0.008 Å^{-1} $<$ Q $<$ 0.3 Å^{-1}). The instrument configurations for direct beam and reflected beam measurements are tabulated in Table 4.1 and Table 4.2, respectively. The neutron wavelength was varied for the first 5 runs, and the sample angle was changed for the last 2 runs. Each neutron wavelength setting has a neutron bandwidth, $\Delta\lambda$ of 3.4 Å. The neutron wavelength quoted in Tables 4.1 and 4.2 is the central wavelength of the neutron bandwidth. Adjustment to the instrument settings can be automated according to user-defined configuration. The default configuration was used for these experiments.

4.2.2 Data Acquisition and Reflectivity Analysis

The timestamp, energy and pixel ID for each event were stored. The timestamps for the rising and falling edge of the accelerator pulse were also recorded. The time-of-flight of each event can be calculated by taking the difference between the accelerator pulse timestamp and the event timestamp within a 60 Hz time frame. The pixel ID can be mapped out into (x, y) coordinates to an areal plot.

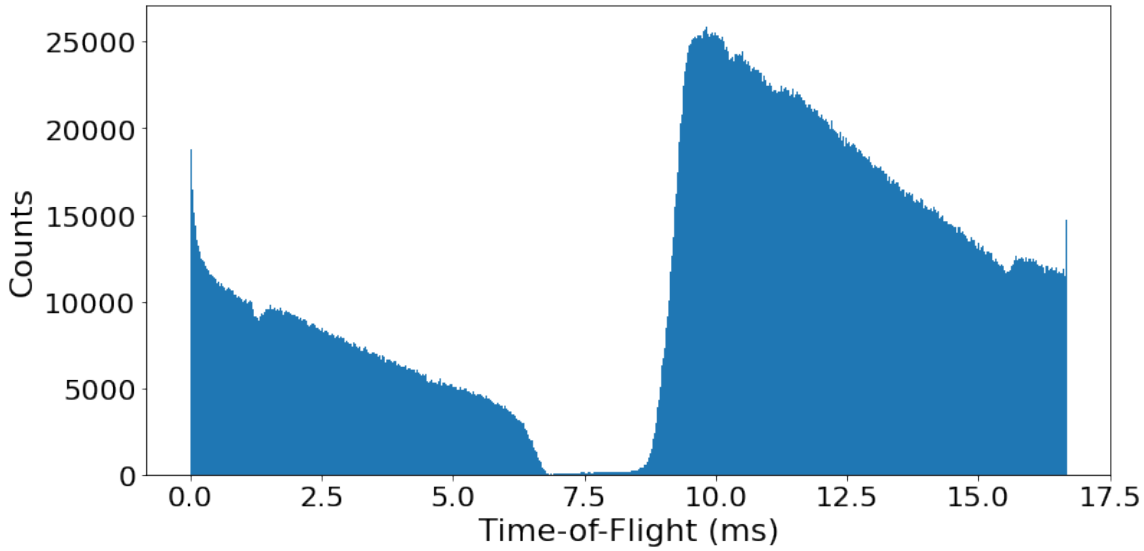
Figure 4.6 shows the shifted and unshifted ToF spectrum for a direct beam measurement. Because of the difference in neutron energies and how ToF was calculated, some neutrons made it to the detector within the same frame, but others were captured in the subsequent frame. Hence in the unshifted ToF spectrum, the ToF appeared in two segments. The first segment belongs to the previous frame and the second segment belongs to the current frame. However, once the frame overlap was accounted for, the shifted ToF spectrum showed the true ToF spectrum for the measurement. The Bragg edges from aluminum were observed in the ToF spectrum as expected since there were aluminum materials used at the beam line. At 0.0 s (in

Table 4.1: These 7 instrument configurations were used in the direct beam measurements at SNS BL-4B.

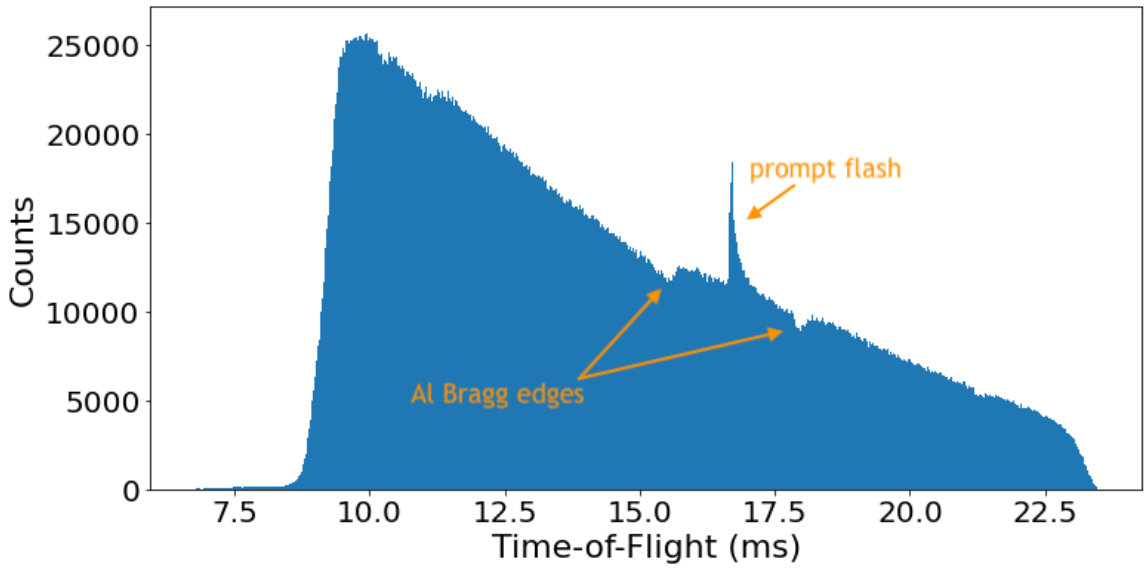
run	central neutron wavelength (Å)	sample angle (^{o})	detector angle (^{o})	acquisition time (s)
1	15.000	0.0	0.0	900
2	12.386	0.0	0.0	900
3	9.740	0.0	0.0	900
4	7.043	0.0	0.0	300
5	4.250	0.0	0.0	300
6	4.250	0.0	0.0	300
7	4.250	0.0	0.0	300

Table 4.2: These 7 instrument configurations were used in the reflected beam measurements at SNS BL-4B.

run	central neutron wavelength (Å)	sample angle (^{o})	detector angle (^{o})	acquisition time (s)
1	15.000	0.600	1.200	300
2	12.386	0.600	1.200	300
3	9.740	0.600	1.200	300
4	7.043	0.600	1.200	300
5	4.250	0.600	1.200	300
6	4.250	1.183	2.366	600
7	4.250	2.343	4.686	4030



(a)



(b)

Figure 4.5: (a) Unshifted and (b) shifted ToF spectrum for a direct beam measurement (run #5).

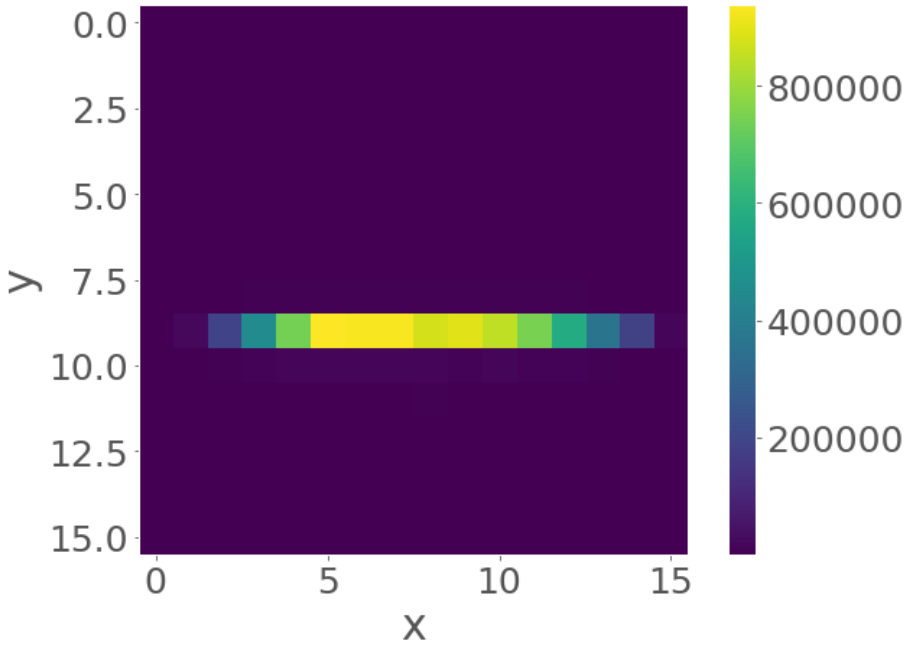
unshifted ToF spectrum) or 16.67 ms (in shifted ToF spectrum), the proton beam hit the target. At this instant, different types of particles were generated including neutrons and γ-rays. Because γ-rays travel at the speed of light, the prompt pulse peak at around 0 s/16.67 ms was presumably mostly comprised of γ-rays. Because neutrons have mass and they do not travel at the speed of light, neutrons took a longer time time to arrive at the detector. The distance between the moderator and the detector is 15.09 m.

Using the pixel ID, the positional information can be derived such as the area plot and the cross-sectional count rate profile as shown in Figures 4.6a and 4.6b. Most events were captured within a narrow region given the size of the beam slit at the instrument. In hindsight, the beam slit should have been made larger so that the beam spot covers multiple rows instead of a single row to obtain better statistics.

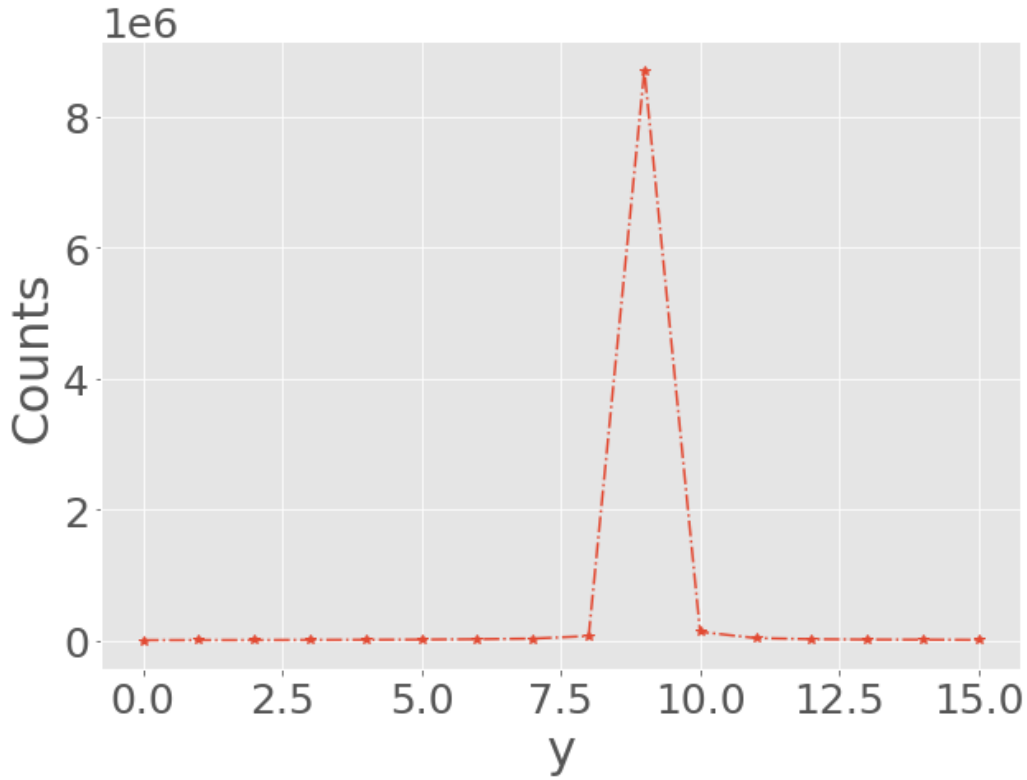
This analysis focuses solely on specular reflectivity. Hence, only background-subtracted events from the narrow region (row 9) were used to generate the reflectivity curve. Events captured elsewhere were disregarded, which could have been used for off-specular reflectivity. Additionally, events that fell within the prompt pulse region were disregarded as it was an artifact from the proton beam hitting the target. To transform the ToF measurements to a reflectivity curve, the scattering vector, Q [66] was calculated, where θ is the detector angle and λ is the neutron wavelength. The neutron wavelength can be calculated from the velocity of a neutron [66]:

$$\lambda\ [\mathring{A}] = \frac{3956}{v\ [m/s]} \tag{4.2}$$

The velocity of the neutron is the ratio of the distance traveled to the neutron ToF. For each run, the data were normalized with the proton charge of the accelerator pulse because the amount of charge hitting the target affects the number of neutrons produced and the proton charge for every pulse was not a constant variable. Lastly, the reflectivity was obtained by taking the ratio of the reflected beam measurements to the direct beam measurements.



(a)



(b)

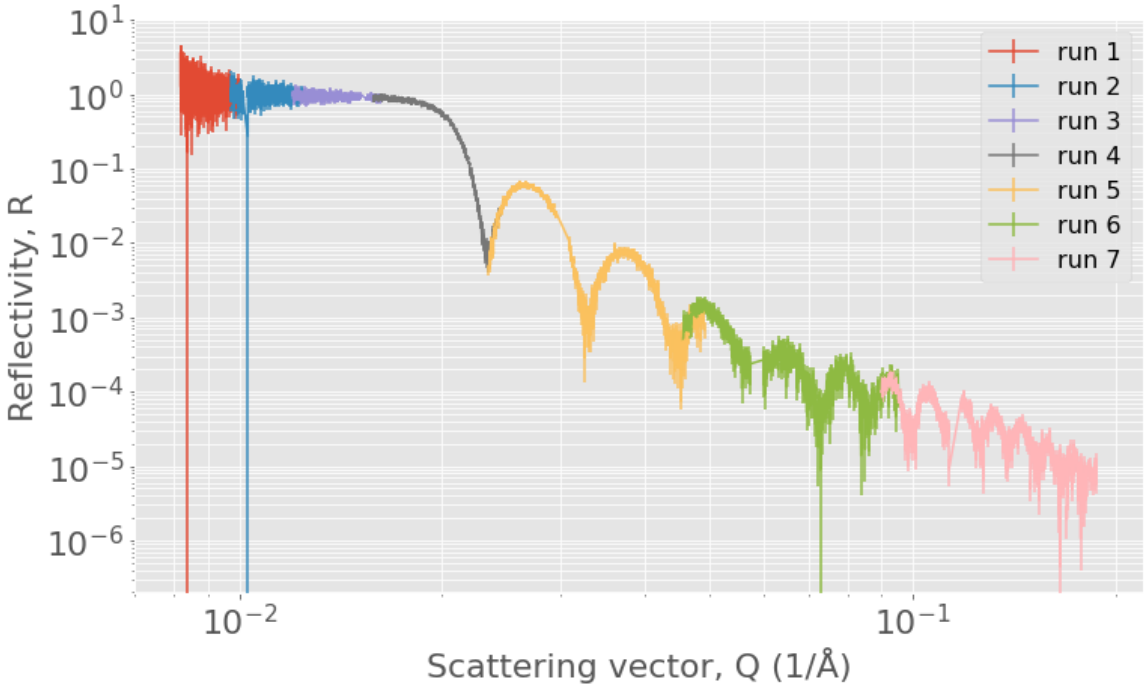
Figure 4.6: The data collected during acquisition includes (a) the time-of-flight (ToF) measurement, (b) the area plot and (c) the cross-section profile of the detector count rate.

4.2.3 Results and Discussion

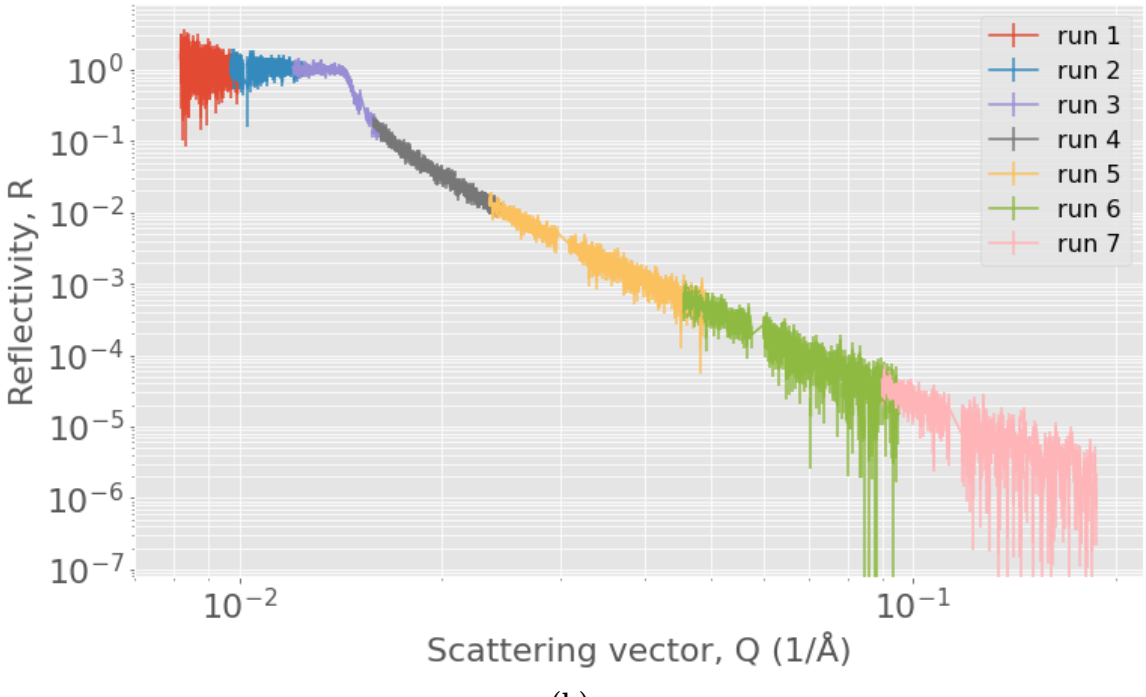
After performing the reflectivity analysis described in the previous section, the reflectivity curves were obtained, shown in Figure 4.7. Measurements of each run were plotted with a different color to show the Q range each setting covers. Upon closer look, small breaks were observed in different parts of the reflectivity curve, typically within the same run measurement. The breaks were a result of the way the prompt pulse region was treated. In our preliminary reflectivity analysis, events that occur within the prompt pulse region were simply disregarded. The events that were disregarded are the reason there were missing links in the reflectivity curve, since those events belong to certain Qs. A better way of treating the events in the prompt pulse region would be by interpolating (inferring) the events in the prompt pulse region so that not all events that fell within the prompt pulse region were completely eliminated.

To evaluate the quality of the reflectivity measurements obtained using the pixelated detector, the same measurements were repeated using MWPC as a reference for both the iridium and quartz samples. To transform the reflectivity curve to scattering length density (SLD) profile, the reflectivity measurements were modeled using a reflectivity fitting software [36, 18]. The fitting process first involved defining an initial SLD profile. The SLD profile is made up of a series of layers. Each layer is defined by thickness, a uniform SLD and roughness. Once the initial SLD was properly set up, the reflectivity was computed for the SLD profile and compared with the measured reflectivity. Hence, it is crucial to have prior knowledge about the sample composition to obtain an accurate and reliable SLD. The layer models specified for the iridium and quartz sample were tabulated in Tables 4.3 and 4.4.

Once the initial layer models were properly defined to the best knowledge, the reflectivity fitting program was run using the Nelder-Mead algorithm as its fitting engine [52]. The objective of the fitting engine was to minimize the least-square difference between the computed reflectivity and the measured reflectivity. Figures 4.8 and 4.9 show the measured and computed reflectivity for iridium and quartz,



(a)



(b)

Figure 4.7: Plots show the reflectivity curves for (a) iridium and (b) quartz samples using the pixelated detector.

Table 4.3: Layer model for the iridium sample.

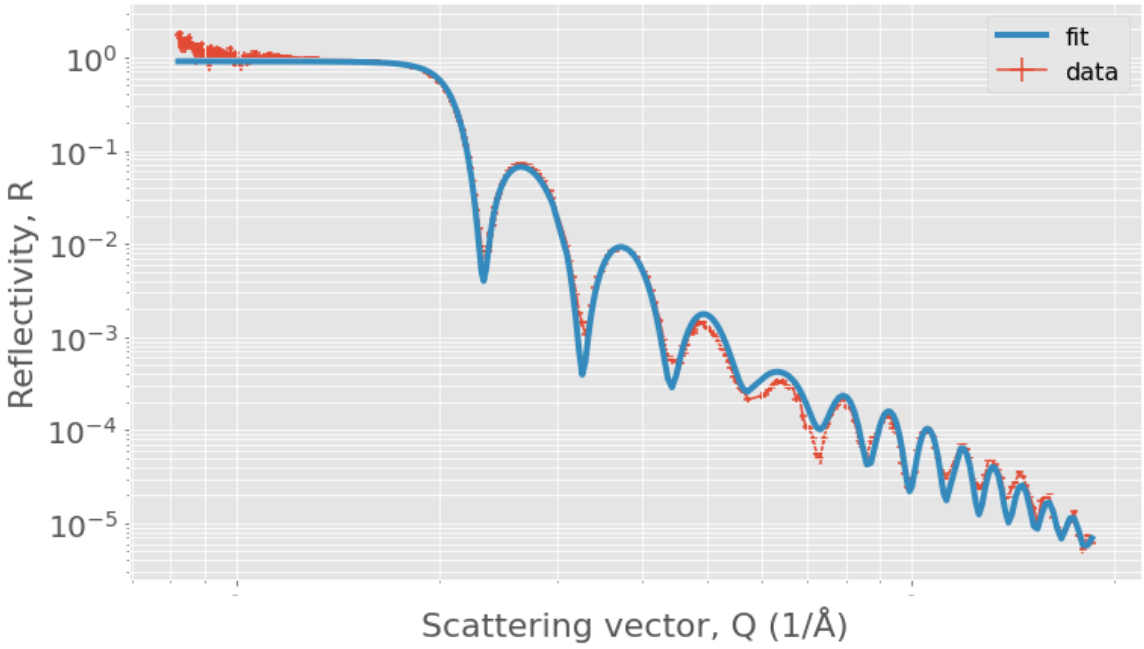
Layer	Thickness (Å)	SLD (10^{-6}/Å^2)	Roughness (Å)
Air	-	0.0	-
Iridium oxide	48.68	3.807	22.76
Iridium	457.2	7.153	6.786
Silicon oxide	18.12	0.048	1.309
Silicon	-	2.07	0.691

Table 4.4: Layer model for the quartz sample.

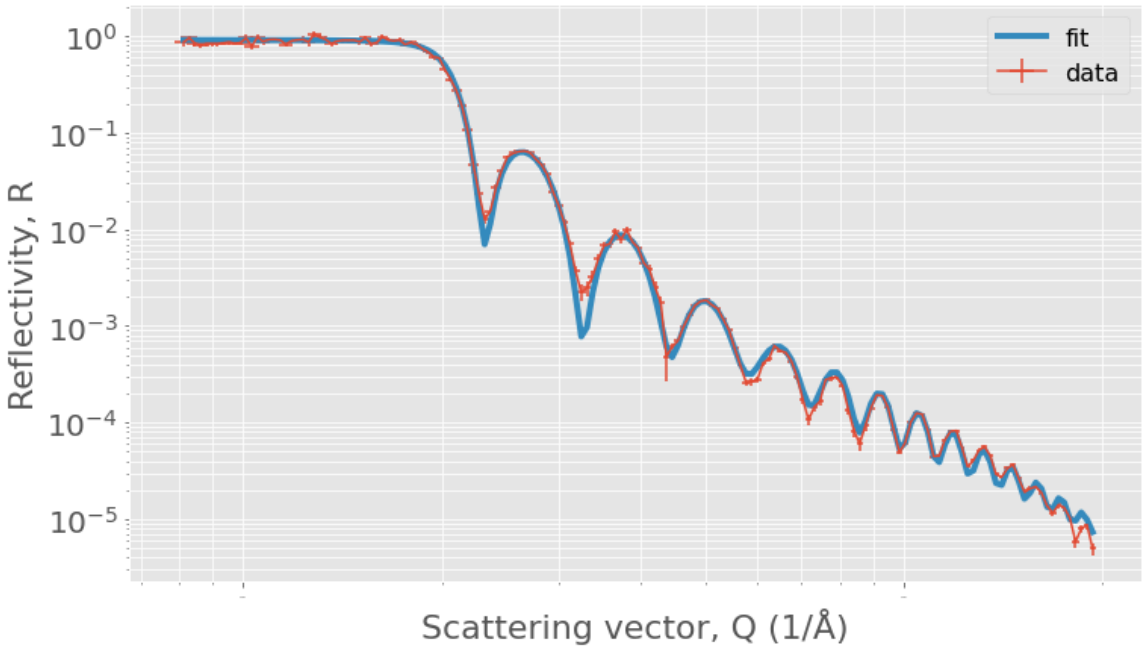
Layer	Thickness (Å)	SLD (10^{-6}/Å^2)	Roughness (Å)
Air	-	0.0	-
Quartz	-	4.068	1.012

respectively. It should be noted that the reflectivity curves for the pixelated detector were rebinned with the same number of bins used for MWPC to obtain a decent number of counts per bin. The computed reflectivity was in good agreement with the measured reflectivity. Both detectors show well-defined interference fringes (Kiessig fringes) in the measured reflectivity for the iridium sample, and a clear-cut drop-off at the same Q in the measured reflectivity for the quartz sample.

Figure 4.10 shows the SLD profiles for the iridium and quartz sample after the reflectivity model fitting was complete. The pixelated neutron detector is labeled as PiNDe. The SLD profile inferred from the measured reflectivity using the pixelated detector was in close agreement with the SLD profile inferred from the measured reflectivity using MWPC. For the iridium sample, both SLD profiles show that the depth and thickness of the iridium layer were very similar. Meanwhile, the SLD profiles for the quartz sample show a similar transition at the interface between air and quartz. A more quantitative outcome of the SLD profiles for the quartz and iridium samples obtained is summarized in Tables 4.5 and 4.6, respectively. The surface roughness of a layer derives from off-specular reflectivity, which was not taken into account in the current analysis. The uncertainty provided in Table 4.5 and 4.6 were the statistical uncertainty obtained using the DREAM engine [18]. Because the pixelated detector was installed at the instrument without precision alignment, systematic uncertainties were expected but they were not quantified in this experiment.

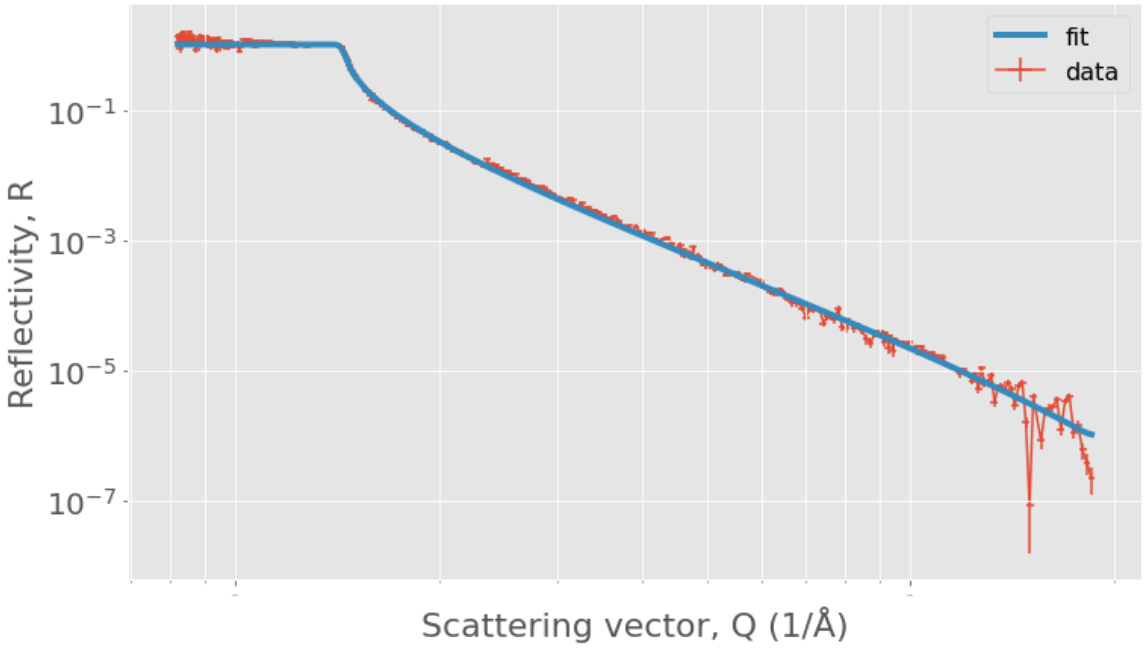


(a)

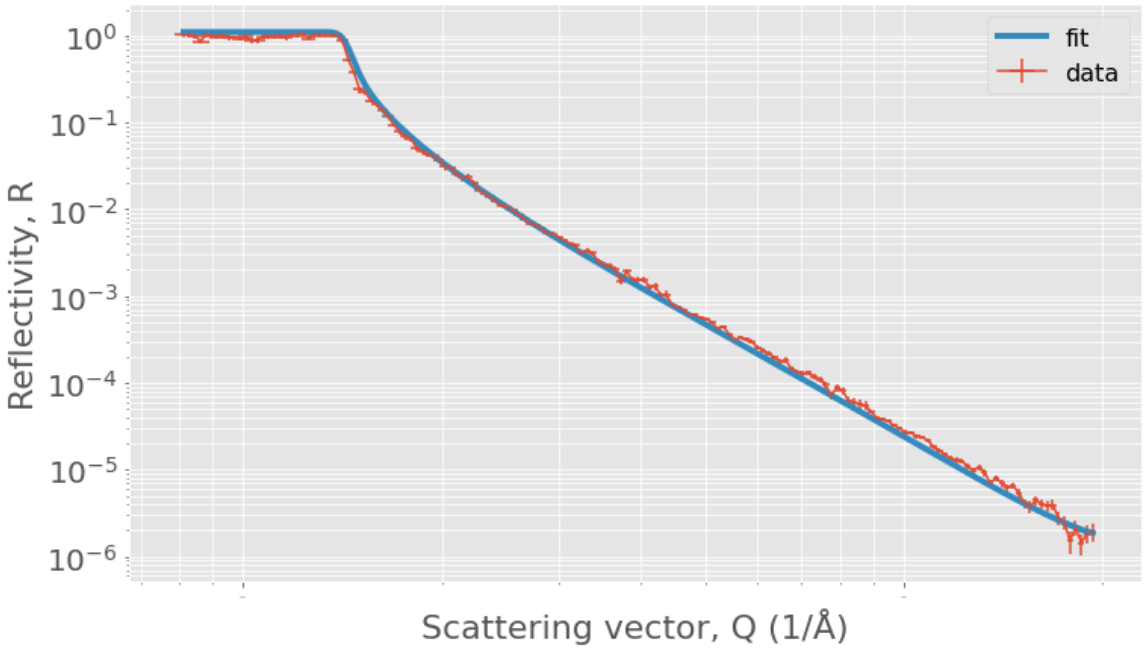


(b)

Figure 4.8: Plots show the reflectivity curves for iridium samples using (a) the pixelated detector and (b) MWPC.

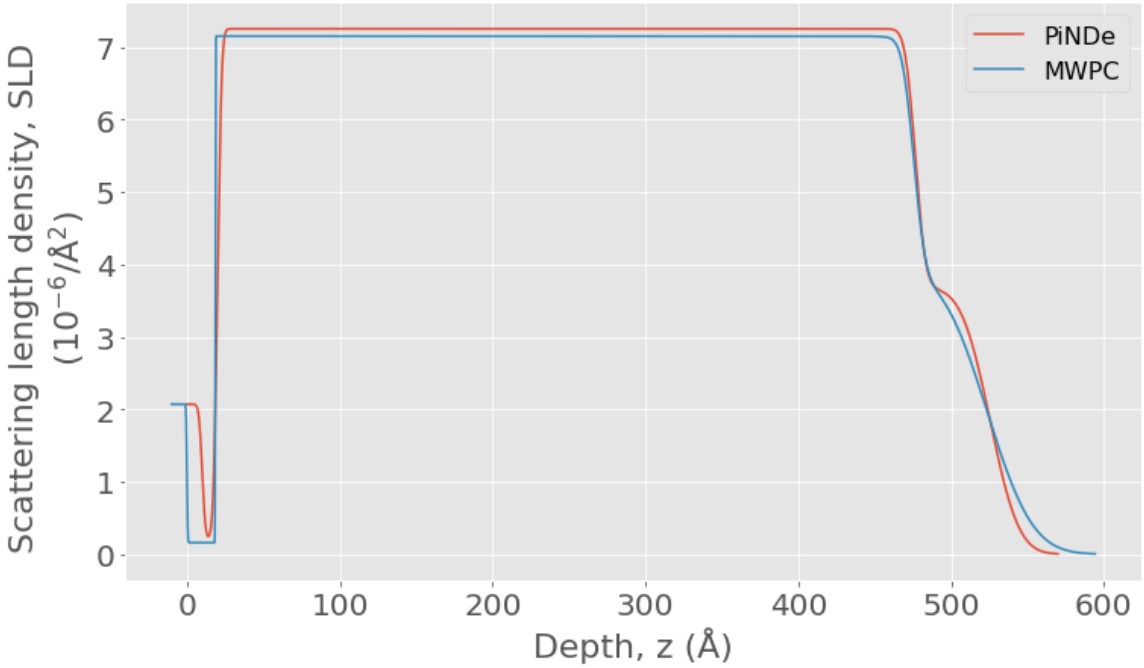


(a)

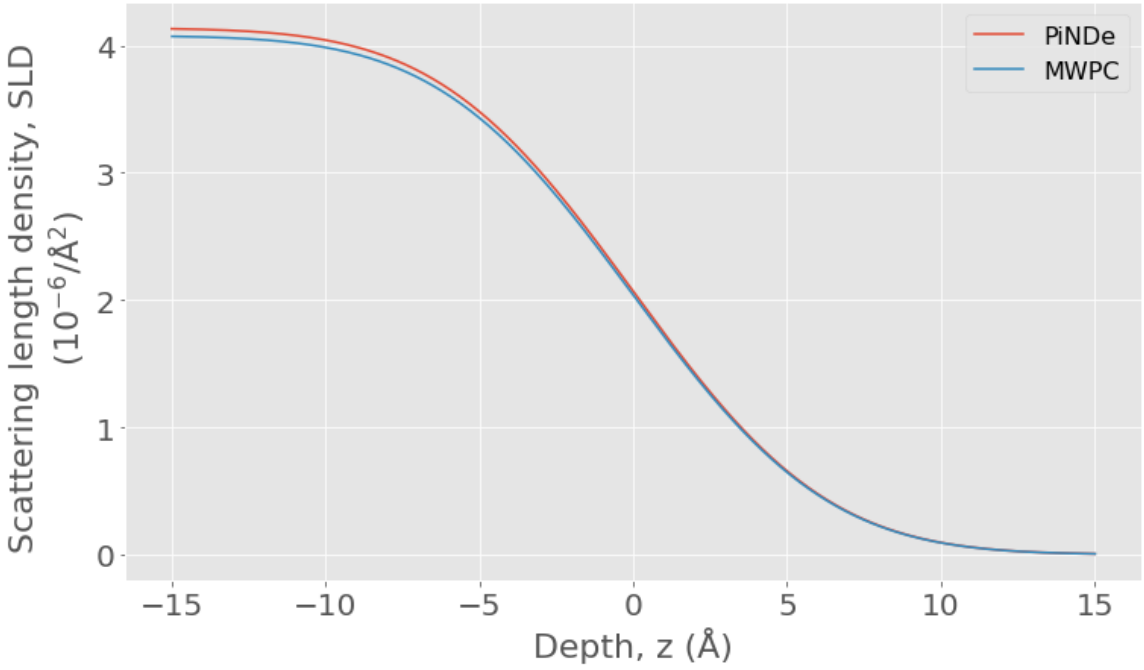


(b)

Figure 4.9: Plots show the reflectivity curves for quartz samples using (a) the pixelated detector and (b) MWPC.



(a)



(b)

Figure 4.10: Plots show the scattering length density profile for (a) iridium and (b) quartz samples using both the pixelated detector and MWPC.

Table 4.5: The thickness, SLD, roughness and χ^2 goodness of fit for the quartz sample

Parameter	MWPC	PiNDe
quartz layer		
thickness (Å)	-	-
SLD ($10^{-6}/\mathring{A}^2$)	4.078 ± 0.007	4.138 ± 0.0039
roughness (Å)	-	-
goodness of fit		
χ^2	5.33	7.317

Table 4.6: The thickness, SLD, roughness and χ^2 goodness of fit for the iridium sample

Parameter	MWPC	PiNDe
iridium oxide layer		
thickness (Å)	48.56 ± 0.69	49.38 ± 0.16
SLD ($10^{-6}/\mathring{A}^2$)	3.833 ± 0.01	3.663 ± 0.032
roughness (Å)	22.78 ± 0.91	1.012 ± 0.19
iridium layer		
thickness (Å)	457.3 ± 0.26	455.0 ± 0.16
SLD ($10^{-6}/\mathring{A}^2$)	7.158 ± 0.02	7.249 ± 0.0036
roughness (Å)	6.379 ± 0.53	1.037 ± 0.13
silicon oxide layer		
thickness (Å)	17.97 ± 0.46	29.56 ± 0.66
SLD ($10^{-6}/\mathring{A}^2$)	0.045 ± 0.061	2.785 ± 0.03
roughness (Å)	1.495 ± 0.53	0.263 ± 0.37
goodness of fit		
χ^2	4.015	10.36

Chapter 5

Summary and Conclusion

A high-rate pixelated neutron detector was developed for neutron reflectometry instruments at the SNS, ORNL. Chapter 1 focuses on the introductory topics on spallation neutron source, neutron scattering and neutron reflectometry. It also presents the motivation behind the project and prior similar research. Chapter 2 details the design and construction of the detector prototypes. This chapter touches upon the scintillators, photodetectors, readout electronics, signal processing, firmware and software of the detector system. It also highlights major changes implemented from the first detector prototype to the second detector prototype. Chapter 3 outlines the process of detector characterization using standard metrics such as counting rate, neutron detection efficiency, γ-sensitivity, spatial resolution, crosstalk and uniformity. The detector performance for both prototypes was summarized in this chapter as well. Chapter 4 dives into performing neutron reflectivity experiments on standard samples using the pixelated detector. The current detector, MWPC, was used as a benchmark to evaluate the quality of the reflectivity measurements taken using the pixelated detector. This chapter also covers the analysis for reflectivity measurements, from obtaining reflectivity curve, $R(Q)$ using time-of-flight measurements to inferring the scattering length density of the sample.

5.1 Summary of Research Findings

The comparison between the performance of detector prototypes and instrument requirements is tabulated in Table 5.1. The high-rate pixelated neutron detector demonstrated its high counting rate capability from all the rate tests. The limit of counting rate capability of the pixelated detector has not yet been determined as the detector did not experience count rate saturation in these counting rate tests even at the highest neutron flux settings. More intense neutron flux is needed to determine the maximum limit in the counting rate.

Despite having a γ-sensitivity higher than desired, the pixelated detector still was able to produce reflectivity measurements that were in very good agreement with the reflectivity measurements obtained using MWPC. This is valid at least for the neutron reflectivity experiments using standard samples. More understanding of the acceptable level of γ sensitivity is needed for a general sample. The same applies to the spatial resolution of the detector, as the spatial resolution of the second detector prototype is slightly larger than what is listed in the instrument requirements.

The neutron detection efficiency of the detector is dependent on the neutron wavelength as the cross-section of ^6Li increases with increasing wavelength. Therefore, the neutron detection efficiency is expected to be higher for longer neutron wavelengths. This is desirable as the upcoming neutron reflectometers in the Second Target Station (STS) are expected to have neutrons with a longer wavelength. Even though the active area of the detector prototypes is smaller than what is required, the upgrade in the readout system for the second detector prototype has made it a lot easier to scale up the detector system to a larger active area without significant modification to the readout electronics.

Overall, the high-rate pixelated neutron detector is a promising candidate for neutron reflectometry instruments, especially with its high counting rate capability. Among the other high-rate designs such as the Multi-Blade and BAND-GEM, the rate capability of the pixelated detector exceeds the rate capability of the Muilti-Blade and

Table 5.1: Comparison between the performance of detector prototypes and instrument requirements.

Parameters	First prototype	Second prototype	Instrument Requirement
Global time-average count rate (cps)	$\geq 1 \times 10^6$	$\geq 1.8 \times 10^6$	1×10^6
Local time-average count rate (cps/cm^2)	$\geq 3.92 \times 10^5$	$\geq 2.25 \times 10^5$	-
Global instantaneous count rate (cps)	-	$\geq 1.03 \times 10^6$	-
Local instantaneous count rate (cps/cm^2)	-	$\geq 1.73 \times 10^6$ (83.5 kcps/pixel)	-
Neutron efficiency relative to ^{3}He detector (%)	92 (4.2 Å) 75 (1.8 Å)	62 (4.2 Å)	≥ 60 (2.0 Å)
Spatial resolution (mm)	2.0	2.2	1-2
Crosstalk (%)	≤ 3	≤ 1	
Active area (cm^2)	1.6×1.6	3.56×3.56	20×20
Gamma sensitivity	1×10^{-3} (PHD) 1×10^{-3} (ToT)	1×10^{-2} (QDC)	1×10^{-6}

is on the same order of magnitude as the rate capability of BAND-GEM. Even though the pixelated detector offers desirable capabilities in terms of counting rate, neutron detection efficiency, spatial resolution and scalability, it is by no means perfect. This leads to the next section where the recommended future work is discussed.

5.2 Recommendations for Future Work

Since the maximum counting rate capability of the pixelated detector has not yet been determined, a rate test needs to be conducted at a beam line with more intense neutron flux. When determining the maximum counting rate capability of the detector, it is important to understand the bottleneck in the detector system. For example, there is a data transfer rate limit from the readout system to a computer depending on the type of cable used (e.g. 1 *Gbps* for CAT5 Ethernet or 6.6 *Gbps* for an SFP+ cable). There is also a rate limit per ASIC channel from one module (FEM128) to another (FEB/D). The other fundamental factors in limiting the detection rate are the response time of the photodetector and the decay time of the scintillator. The rate limit is determined by the weakest link in the detector system.

Although the pixelated detector performed relatively well in the reflectivity measurement, the γ sensitivity of the detector needs to be further improved. In particular, the γ sensitivity of the second prototype is worse than the γ sensitivity of the first prototype by 2 orders of magnitude. There were two major changes made to the second prototype, which were the SiPM and the readout system. Further investigation is needed to figure out whether the SiPM or the readout system or both are the culprits to a higher γ sensitivity. There are several approaches to improve the γ sensitivity. First, the scintillator elements can be made thinner. The scintillator is 2.0 mm thick with a 95% capture efficiency. The thickness of the scintillator can be further reduced to 1.0 mm with a 75% capture efficiency. With a thinner scintillator, there is also a lower sensitivity towards γ rays. This presents a tradeoff between neutron efficiency and γ sensitivity. However, if the scintillator elements are arranged

at a certain angle, the neutron efficiency can be improved while minimizing the γ sensitivity. Another alternative if the SiPM was the main culprit, could be to find a replacement SiPM array. It may be worthwhile to look into the market to see if there are any other suitable candidates. It will also be beneficial to have a replacement SiPM with a pitch less than 2.0 mm.

Since the detector area needs to be extended to a much larger area, it is important to ensure that the performance of the detector remains consistent on a larger scale. Two versions of the custom FEB/S were designed, one of which directly plugs into the readout system, but cannot accommodate more than 4×4 SiPM arrays. The other one can be scaled up to an unlimited number of SiPM arrays, but does not directly plug into the readout system. Ribbon cables may be required to make the electrical connection. However, this version of the custom FEB/S has not yet been tested and such testing is planned as future work.

Bibliography

[1] F. Abelès. Vi methods for determining optical parameters of thin films. In *Progress in optics*, volume 2, pages 249–288. Elsevier, 1963. 15

[2] G. Albani, E. P. Cippo, G. Croci, A. Muraro, R. Hall-Wilton, C. Höglund, A. Menelle, G. Grosso, F. Murtas, M. Rebai, et al. High-rate measurements of the novel band-gem technology for thermal neutron detection at spallation sources. *Nuclear Instruments and Methods in Physics Research Section A: Accelerators, Spectrometers, Detectors and Associated Equipment*, 957:163389, 2020. 23

[3] H. Ambaye, R. Goyette, A. Parizzi, and F. Klose. Sns magnetism reflectometer. *Neutron News*, 19(3):11–13, 2008. 21

[4] J. F. Ankner, X. Tao, C. E. Halbert, J. Browning, S. Michael Kilbey, O. A. Swader, M. Dadmun, E. Kharlampieva, and S. Sukhishvili. The sns liquids reflectometer. *Neutron News*, 19(3):14–16, 2008. 21

[5] Avnet. Microzed zynq evaluation kit and system on module hardware user guide. xii, 43, 45

[6] R. Becker, A. Grillo, R. Jacobsen, R. Johnson, I. Kipnis, M. Levi, L. Luo, P. Manfredi, M. Nyman, V. Re, et al. Signal processing in the front-end electronics of babar vertex detector. *Nuclear Instruments and Methods in Physics Research Section A: Accelerators, Spectrometers, Detectors and Associated Equipment*, 377(2-3):459–464, 1996. 47

[7] K. Berry. Neutron lifecycle series: Helium-3 gas detectors at the sns and hfir. URL https://conference.sns.gov/event/56/attachments/64/192/Lecture_6a-%20_Neutron_Detection_with_He3_-_Kevin_Berry.pdf. 20, 67

[8] G. Blasse. Scintillator materials. *Chemistry of Materials*, 6(9):1465–1475, 1994. 29, 30

[9] P. Böni and A. Furrer. Introduction to neutron scattering. In *Neutron Scattering in Layered Copper-Oxide Superconductors*, pages 1–22. Springer, 1998. 5

[10] M. Born and E. Wolf. *Principles of optics: electromagnetic theory of propagation, interference and diffraction of light*. Elsevier, 2013. 15

[11] L. Boyd. *Characterisation of a position sensitive thermal neutron detector*. PhD thesis, University of Glasgow, 2021. 25

[12] J. Chadwick. Possible existence of a neutron. *Nature*, 129(3252):312–312, 1932. ix, 6

[13] S.-A. Chong, R. Riedel, T. Visscher, C. Dohanue, B. Hannan, C. Montcalm, and J. Hayward. High data-rate neutron-sensitive pixelated detector using silicon photomultiplier. In *2019 IEEE Nuclear Science Symposium and Medical Imaging Conference (NSS/MIC)*, pages 1–4. IEEE, 2019. 20

[14] F. Cousin and G. Fadda. An introduction to neutron reflectometry. In *EPJ Web of Conferences*, volume 236, page 04001. EDP Sciences, 2020. xi, 12, 13, 14, 15, 17

[15] R. Crawford, R. Dean, P. Ferguson, J. Galambos, F. Gallmeier, T. Mcmanamy, and M. Rennich. The second target station at the ornl spallation neutron source. In *Journal of Physics: Conference Series*, volume 251, page 012054. IOP Publishing, 2010. 1, 3, 19

[16] M. Crow, J. Hodges, and R. Cooper. Shifting scintillator prototype large pixel wavelength-shifting fiber detector for the powgen3 powder diffractometer. *Nuclear Instruments and Methods in Physics Research Section A: Accelerators, Spectrometers, Detectors and Associated Equipment*, 529(1-3):287–292, 2004. 25

[17] R. Cubitt and G. Fragneto. Neutron reflection:: Principles and examples of applications. In *Scattering*, pages 1198–1208. Elsevier, 2002. URL https://doi.org/10.1016/B978-012613760-6/50065-6. 12, 15

[18] M. Doucet, R. Ferraz Leal, and T. Hobson. Web interface for reflectivity fitting. *SoftwareX*, 7:287–293, 2018. doi: 10.1016/j.softx.2018.09.001. 99, 102

[19] G. Ehlers, A. Athanasiades, L. Sun, C. S. Martin, M. Regmi, and J. L. Lacy. Performance tests of boron-coated straw detectors with thermal and cold neutron beams. *Nuclear Instruments and Methods in Physics Research Section A: Accelerators, Spectrometers, Detectors and Associated Equipment*, 953:163238, 2020. 23

[20] P. Electronics. Petsys time-of-flight asic evaluation kit, . URL https://www.petsyselectronics.com/web/public/products/2. xii, 53, 56, 58

[21] P. Electronics. Sipm readout system, . URL https://www.petsyselectronics.com/web/public/products/6. xiii, 53, 57, 58

[22] P. Electronics. Petsys tofpet2 asic, . URL https://www.petsyselectronics.com/web/public/products/1. 53

[23] M. R. Eskildsen and B. Khaykovich. Second target station workshop report, 2015. URL https://neutrons.ornl.gov/sites/default/files/STS%20Workshop%20Report.pdf. ix, 21, 22

[24] F. Fernandez-Alonso and D. L. Price. *Neutron Scattering: fundamentals*, volume 44. Academic Press, 2013. 5, 8, 9, 10

[25] S. Ferry, F. Guilloux, S. Anvar, F. Chateau, E. Delagnes, V. Gautard, F. Louis, E. Monmarthe, H. Le Provost, S. Russo, et al. Multi-time-over-threshold technique for photomultiplier signal processing: Description and characterization of the scott asic. *Nuclear Instruments and Methods in Physics Research Section A: Accelerators, Spectrometers, Detectors and Associated Equipment*, 695:52–60, 2012. 47

[26] J. Fried, J. Harder, G. Mahler, D. Makowiecki, J. Mead, V. Radeka, N. Schaknowski, G. Smith, and B. Yu. A large, high performance, curved 2d

position-sensitive neutron detector. *Nuclear Instruments and Methods in Physics Research Section A: Accelerators, Spectrometers, Detectors and Associated Equipment*, 478(1-2):415–419, 2002. 20, 67

[27] J. D. Galambos, D. E. Anderson, D. Bechtol, K. L. Bethea, N. Brown, W. Carden, S. M. Chae, A. Clark, D. M. Counce, K. Craft, et al. Technical design report: Second target station. Technical report, Oak Ridge National Laboratory, Jan 2015. URL https://neutrons.ornl.gov/sites/default/files/SNS_STS_Technical_Design_Report_2015-01.pdf. ix, 21, 22, 26

[28] S. Gobain. Reflector paint for plastic scintillators (bc-620) saint gobain. URL http://static6.arrow.com/aropdfconversion/5f21e5069a452c0b4d6a95c9954f098ba0ad6261/113423053200175sgc-bc620-data-sheet_.pdf. 47

[29] M. P. Hehlen, B. W. Wiggins, A. Favalli, M. Iliev, and K. D. Ianakiev. Light propagation in a neutron detector based on 6li glass scintillator particles in an organic matrix. *Journal of Applied Physics*, 124(12):124502, 2018. doi: 10.1063/1.5047433. xi, 35, 36

[30] S. Henderson, W. Abraham, A. Aleksandrov, C. Allen, J. Alonso, D. Anderson, D. Arenius, T. Arthur, S. Assadi, J. Ayers, et al. The spallation neutron source accelerator system design. *Nuclear Instruments and Methods in Physics Research Section A: Accelerators, Spectrometers, Detectors and Associated Equipment*, 763:610–673, 2014. URL https://doi.org/10.1016/j.nima.2014.03.067. 1

[31] K. Iniewski. *Advanced Materials for Radiation Detection*. Springer, 2022. ix, 31

[32] S. Jaksch, R. Engels, G. Kemmerling, C. Gheorghe, P. Pahlsson, S. Désert, and F. Ott. Cumulative reports of the sonde project july 2017. *arXiv preprint arXiv:1707.08679*, 2017. 25

[33] S. Jaksch, R. Engels, G. Kemmerling, U. Clemens, S. Désert, H. Perrey, C. Gheorghe, A. Fredriksen, P. Øya, H. Frielinghaus, and et al. Recent developments sonde high-flux detector project. *Proceedings of the International Conference on Neutron Optics (NOP2017)*, 2018. doi: 10.7566/jpscp.22.011019. 25

[34] K. Kanaki, M. Klausz, T. Kittelmann, G. Albani, E. P. Cippo, A. Jackson, S. Jaksch, T. Nielsen, P. Zagyvai, R. Hall-Wilton, and et al. Detector rates for the small angle neutron scattering instruments at the european spallation source. *Journal of Instrumentation*, 13(07), Jul 2018. doi: 10.1088/1748-0221/13/07/p07016. URL https://iopscience.iop.org/article/10.1088/1748-0221/13/07/P07016/pdf. 19, 20, 23

[35] M. Katagiri, T. Nakamura, M. Ebine, A. Birumachi, S. Sato, E. Shooneveld, and N. Rhodes. High-position-resolution neutron imaging detector with crossed wavelength shifting fiber read-out using two zns/6lif scintillator sheets. *Nuclear Instruments and Methods in Physics Research Section A: Accelerators, Spectrometers, Detectors and Associated Equipment*, 573(1-2):149–152, 2007. 25

[36] P. Kienzle, K. O'Donovan, J. Ankner, N. Berk, and C. Majkrzak. Reflectometry software: Refl1d, 2015. 99

[37] M. Klausz, K. Kanaki, P. Zagyvai, and R. Hall-Wilton. Performance evaluation of the boron coated straws detector with geant4. *Nuclear Instruments and Methods in Physics Research Section A: Accelerators, Spectrometers, Detectors and Associated Equipment*, 943:162463, Jul 2019. doi: 10.1016/j.nima.2019.162463. 19, 23

[38] R. T. Kouzes, J. H. Ely, L. E. Erikson, W. J. Kernan, A. T. Lintereur, E. R. Siciliano, D. C. Stromswold, and M. L. Woodring. Alternative neutron detection testing summary. Technical report, Pacific Northwest National Lab.(PNNL), Richland, WA (United States), 2010. 23

[39] R. T. Kouzes, J. H. Ely, A. T. Lintereur, E. K. Mace, D. L. Stephens, and M. L. Woodring. Neutron detection gamma ray sensitivity criteria. *Nuclear Instruments and Methods in Physics Research Section A: Accelerators, Spectrometers, Detectors and Associated Equipment*, 654(1):412–416, 2011. 23

[40] R. T. Kouzes, A. T. Lintereur, and E. R. Siciliano. Progress in alternative neutron detection to address the helium-3 shortage. *Nuclear Instruments and Methods in Physics Research Section A: Accelerators, Spectrometers, Detectors and Associated Equipment*, 784:172–175, 2015. 23

[41] S. Kumar, M. Herzkamp, D. Durini, H. Nöldgen, and S. V. Waasen. Development of a solid-state position sensitive neutron detector prototype based on 6li-glass scintillator and digital sipm arrays. *Nuclear Instruments and Methods in Physics Research Section A: Accelerators, Spectrometers, Detectors and Associated Equipment*, page 161697, 2018. doi: 10.1016/j.nima.2018.12.012. 25, 35

[42] J. L. Lacy, A. Athanasiades, N. Shehad, R. Austin, and C. Martin. Novel neutron detector for high rate imaging applications. In *2002 IEEE Nuclear Science Symposium Conference Record*, volume 1, pages 392–396. IEEE, 2002. 23

[43] J. L. Lacy, A. Athanasiades, L. Sun, C. S. Martin, and G. J. Vazquez-Flores. Boron coated straw detectors as a replacement for 3 he. In *2009 IEEE Nuclear Science Symposium Conference Record (NSS/MIC)*, pages 119–125. IEEE, 2009. 23

[44] J. L. Lacy, A. Athanasiades, L. Sun, C. S. Martin, T. D. Lyons, M. A. Foss, and H. B. Haygood. Boron-coated straws as a replacement for 3he-based neutron detectors. *Nuclear Instruments and Methods in Physics Research Section A: Accelerators, Spectrometers, Detectors and Associated Equipment*, 652(1):359–363, 2011. 23

[45] K. Lefmann. Neutron scattering: Theory, instrumentation, and simulation. *Niels Bohr Institute, University of Copenhagen*, 2017. URL https://citeseerx.ist.psu.edu/viewdoc/download?doi=10.1.1.323.9868&rep=rep1&type=pdf. 3, 5, 8, 9

[46] T. Mason, D. Abernathy, I. Anderson, J. Ankner, T. Egami, G. Ehlers, A. Ekkebus, G. Granroth, M. Hagen, K. Herwig, et al. The spallation neutron source in oak ridge: A powerful tool for materials research. *Physica B: Condensed Matter*, 385:955–960, 2006. 1, 21

[47] G. Mauri. Development and characterization of detectors for large area application in neutron scattering and small area application in neutron reflectometry, May 2019. URL https://arxiv.org/abs/1905.12311. 19, 23

[48] G. Mauri, F. Messi, M. Anastasopoulos, T. Arnold, A. Glavic, C. Höglund, T. Ilves, I. Lopez Higuera, P. Pazmandi, D. Raspino, et al. Neutron reflectometry with the multi-blade 10b-based detector. *Proceedings of the Royal Society A: Mathematical, Physical and Engineering Sciences*, 474(2216):20180266, 2018.

[49] G. Mauri, I. Apostolidis, M. Christensen, A. Glavic, C. Lai, A. Laloni, F. Messi, A. L. Olsson, L. Robinson, J. Stahn, and et al. The multi-blade boron-10-based neutron detector performance using a focusing reflectometer. *Journal of Instrumentation*, 15(03), 2020. doi: 10.1088/1748-0221/15/03/p03010. 23

[50] A. Muraro, G. Croci, E. P. Cippo, G. Grosso, C. Höglund, G. Albani, R. Hall-Wilton, K. Kanaki, F. Murtas, D. Raspino, and et al. Performance of the high-efficiency thermal neutron band-gem detector. *Progress of Theoretical and Experimental Physics*, 2018(2), Feb 2018. doi: 10.1093/ptep/pty005. 23

[51] A. Muraro, G. Claps, G. Croci, C. Lai, R. De Oliveira, S. Altieri, S. Cancelli, G. Gorini, R. Hall-Wilton, C. Höglund, et al. Mbgem: a stack of borated gem detector for high efficiency thermal neutron detection. *The European Physical Journal Plus*, 136(7):1–14, 2021. 20

[52] J. A. Nelder and R. Mead. A Simplex Method for Function Minimization. *The Computer Journal*, 7(4):308–313, 01 1965. ISSN 0010-4620. doi: 10.1093/comjnl/7.4.308. URL https://doi.org/10.1093/comjnl/7.4.308. 99

[53] U. D. of Commerce and Nist. Nist center for neutron research, Apr 2015. URL https://www.ncnr.nist.gov/programs/reflect/. xi, 18

[54] OnSemiconductor. C-series low noise, blue-sensitive silicon photomultipliers datasheet, 2021. URL https://www.onsemi.com/products/sensors/silicon-photomultipliers-sipm/c-series-sipm. ix, xii, 39, 40, 41, 42, 43, 55

[55] Ordela. Neutron beam monitors, Feb 2019. URL https://ordela.com/neutron-beam-monitors/. 89

[56] L. G. Parratt. Surface studies of solids by total reflection of x-rays. *Physical review*, 95(2):359, 1954. 15

[57] J. Penfold and R. Thomas. The application of the specular reflection of neutrons to the study of surfaces and interfaces. *Journal of Physics: Condensed Matter*, 2(6):1369, 1990. 14

[58] J. Penfold and R. K. Thomas. Neutron reflectivity and small angle neutron scattering: An introduction and perspective on recent progress. *Current opinion in colloid & interface science*, 19(3):198–206, 2014. 14, 15

[59] J. Penfold, Z. Tun, R. Cubitt, et al. Neutron reflectometry: a probe for materials surfaces. In *Proceedings of a Technical Meeting Organized by the International Atomic Energy Agency, Vienna*, 2004. 19, 20

[60] H. Photonics. Hamamatsu mppc (multi-pixel photon counter) arrays: S13361-2050 series. URL https://www.hamamatsu.com/us/en/product/optical-sensors/mppc/mppc_mppc-array/S13361-2050AE-08.html. ix, xii, 53, 54, 55

[61] S. Piatek. Silicon photomultipliers: Operation, performance, and possible applications, 2008. URL https://hub.hamamatsu.com/us/en/webinar/sipm-operation-performance/index.html. ix, xi, 32, 33, 34

[62] F. Piscitelli. Novel boron-10-based detectors for neutron scattering science. *The European Physical Journal Plus*, 130(2):1–9, 2015. 23

[63] F. Piscitelli, J. Buffet, J. Clergeau, S. Cuccaro, B. Guérard, A. Khaplanov, Q. La Manna, J. Rigal, and P. Van Esch. Study of a high spatial resolution 10b-based thermal neutron detector for application in neutron reflectometry: the multi-blade prototype. *Journal of Instrumentation*, 9(03):P03007, 2014. 23

[64] F. Piscitelli, F. Messi, M. Anastasopoulos, T. Bryś, F. Chicken, E. Dian, J. Fuzi, C. Höglund, G. Kiss, J. Orban, et al. The multi-blade boron-10-based neutron detector for high intensity neutron reflectometry at ess. *Journal of Instrumentation*, 12(03):P03013, 2017. doi: 10.1088/1748-0221/12/03/p03013. 23, 25

[65] N. Products. Norland optical adhesive 88 (noa88). URL https://www.norlandprod.com/adhesives/NOA%2088.html. 61

[66] R. Pynn. Neutron scattering: A primer, 1990. URL https://ncnr.nist.gov/summerschool/ss16/pdf/NeutronScatteringPrimer.pdf. ix, 4, 8, 10, 12, 97

[67] V. Radeka, N. Schaknowski, G. Smith, and B. Yu. High-performance, imaging, thermal neutron detectors. *Nuclear Instruments and Methods in Physics Research Section A: Accelerators, Spectrometers, Detectors and Associated Equipment*, 419(2-3):642–647, 1998. 20

[68] J. D. Richards, R. G. Cooper, N. Donahue, and T. Visscher. Development of a neutron-sensitive anger camera for neutron scattering instruments. In *IEEE Nuclear Science Symposuim & Medical Imaging Conference*, pages 1771–1776. IEEE, 1771. 25

[69] R. Riedel, C. Donahue, T. Visscher, and C. Montcalm. Design and performance of a large area neutron sensitive anger camera. *Nuclear Instruments and Methods in Physics Research Section A: Accelerators, Spectrometers, Detectors and Associated Equipment*, 794:224–233, 2015. 25

[70] E. Rofors, N. Mauritzson, H. Perrey, R. Al Jebali, J. Annand, L. Boyd, M. Christensen, U. Clemens, S. Desert, R. Engels, et al. Response of a li-glass/multi-anode photomultiplier detector to collimated thermal-neutron beams. *Nuclear Instruments and Methods in Physics Research Section A: Accelerators, Spectrometers, Detectors and Associated Equipment*, 999:165170, 2021. 25

[71] Scintacor. An introduction to lithium-6 glass. URL https://scintacor.com/technologies/neutrons/. 35

[72] Scintacor. Scintacor lithium glass scintillators, 2021. URL https://www.crystals.saint-gobain.com/radiation-detection-scintillators/crystal-scintillators/lithium-glass-scintillators. ix, 35, 36

[73] S. N. S. (SNS). Neutron sciences. URL https://neutrons.ornl.gov/content/how-sns-works. xi, 1, 2, 3, 4

[74] A. Spowart. Neutron scintillating glasses: Part ii. *Nuclear Instruments and Methods*, 140:19–28, 01 1977. doi: 10.1016/0029-554X(77)90059-3. 35

[75] A. Technologies. Avian-b white reflectance coating, Mar 2020. URL https://aviantechnologies.com/product/avian-b-white-reflectance-coating/. 61

[76] C. Wang, L. Clonts, R. Cooper, M. Crow, Y. Diawara, E. Ellis, L. Funk, B. Hannan, J. Hodges, J. Richards, et al. Wavelength-shifting-fiber scintillation detectors for thermal neutron imaging at sns. In *2011 IEEE Nuclear Science Symposium Conference Record*, pages 4877–4882. IEEE, 2011. 25

[77] R. Welton, M. Stockli, S. Murray, and R. Keller. The status of the spallation neutron source ion source. *Review of scientific instruments*, 75(5):1793–1795, 2004. 1

[78] I. A. Zaliznyak and J. M. Tranquada. Neutron scattering and its application to strongly correlated systems. In *Strongly Correlated Systems*, pages 205–235. Springer, 2015. ix, 6, 9, 10, 12

Appendix

Appendix A

Printed Circuit Board (PCB)

A.1 KiCAD electronic design automation software

KiCAD EDA software is a free software suit that is compatible in major operation systems (Windows, macOS and Linux). It provides an integrated environment for schematic capture and PCB design. A typical workflow in KiCAD can be broken down into two steps:

1. Drawing a schematic diagram

   The schematic is a symbolic representation of the circuit. In KiCAD, the Schematic Editor (Eeschema) is used to draw schematics by adding symbols to the electrical components to the circuit design with right electrical connection. Footprints axre selected for each component. When the schematic is complete, the design has to pass an electrical rule check (ERC) to make sure all electrical connections are properly handled. The schematic is typically drawn first before laying out the circuit board.

2. Laying out a circuit board

   The circuit board is the physical manifestation of the schematic. In KiCAD, the PCB editor (Pcbnew) is used to lay out the board. The layout process requires careful placement of component on the board and copper traces making

connections described in the schematic. Electrical considerations such as trace resistance, controlled impedance requirements, and crosstalk need to be taken into consideration. Once the layout is complete and the board has passed the Design Rule Check (DRC), the board is ready to be manufactured.

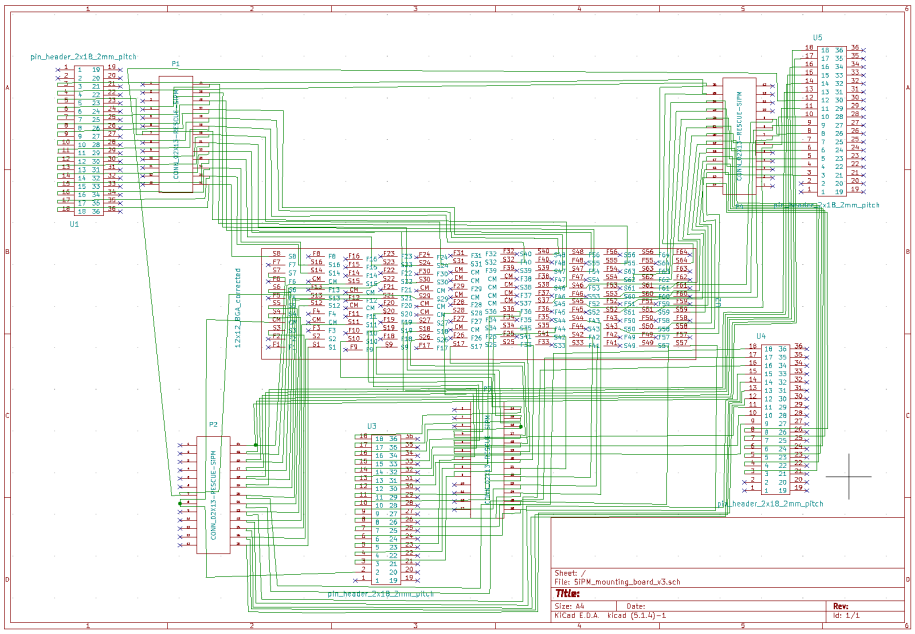
A.2 Mounting Board for First Detector Prototype

In order to mount the SensL ArrayC-10035064P-BGA SiPM to the CROC board, a mounting board was designed using the KiCAD EDA software. The SensL SiPM has a 12×12 ball grid array (BGA) connections. The BGA can be used to mount the array on the mounting board using reflow soldering. The 8×8 SiPM have cathodes connected together to form a common I/O.

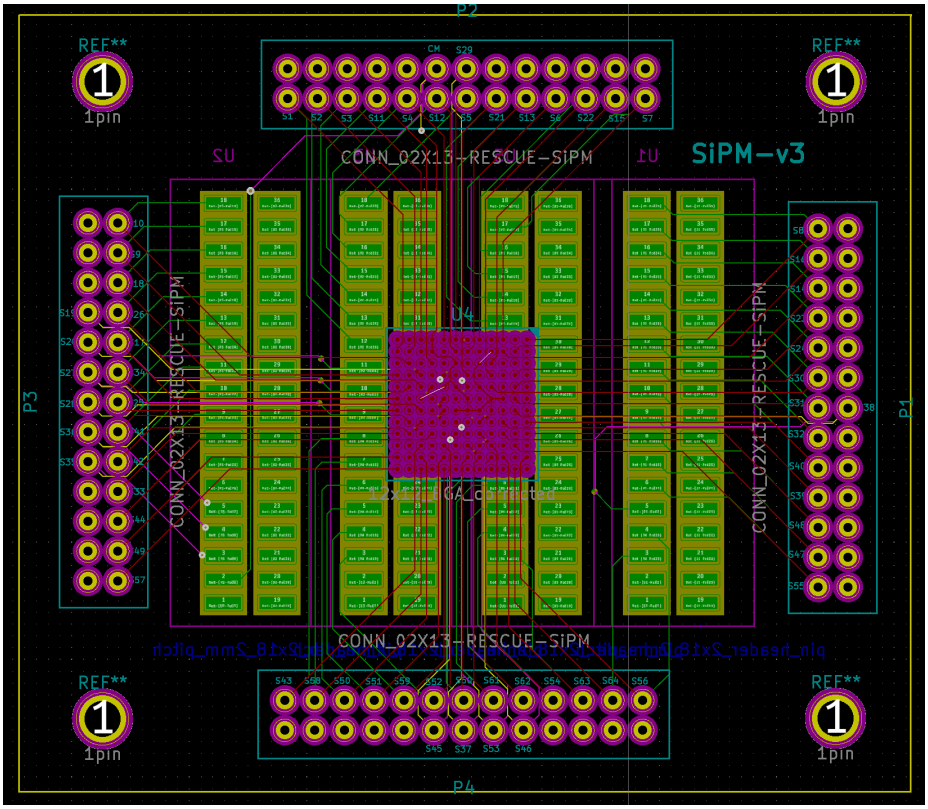
The 12×12 BGA connections are:

- $64 \times$ fast output
- $64 \times$ standard I/O
- $16 \times$ common I/O

For this board, the 64 standard I/O were routed to the headers of the CROC board, and the 16 common I/O were connected to a voltage supply to bias the SiPM array. The 64 fast outputs were not used in the detector system. Four headers with 2×18 pins were used to route the 64 standard output to the CROC board. The schematic diagram and PCB layout for the mounting board are shown in Figure A.1. Not pictured in the schematics, four mounting holes were added to the PCB layout for mechanical support purposes. The width of the copper trace was set to be 0.1 mm, the diameter of the via was set to 0.15 mm and the mask clearance was set to 0.2 mm. A front view and back view of the board was generated using the KiCAD 3D viewer, as shown in Figure A.2.

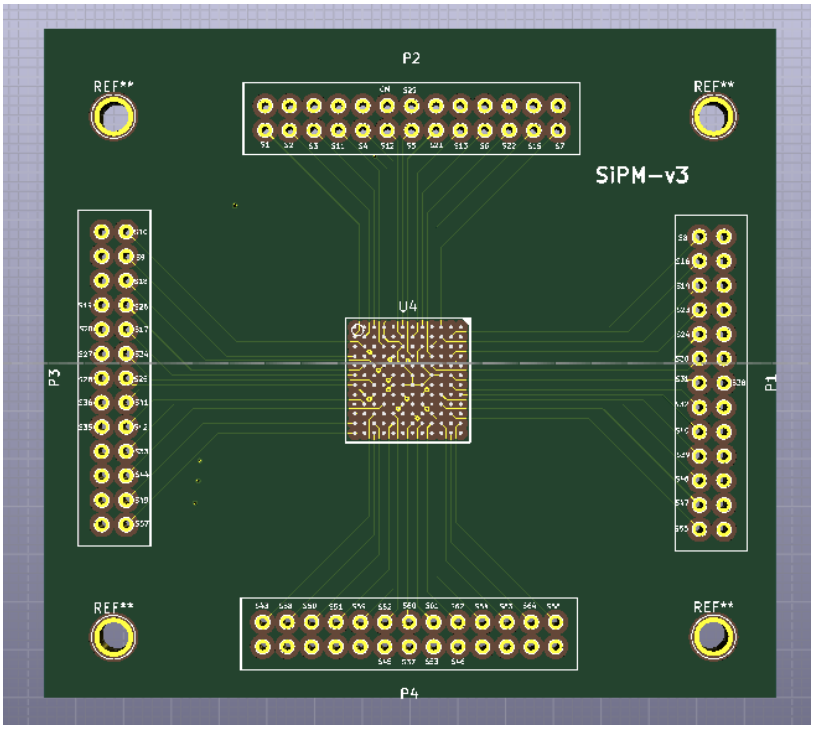


(a)

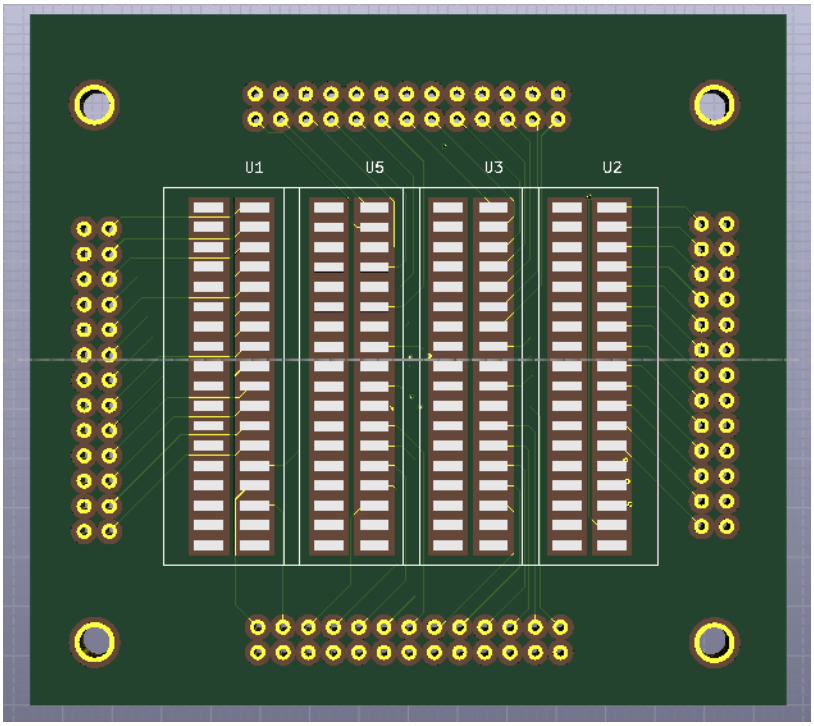


(b)

Figure A.1: (a) Schematic and (b) PCB layout of the SiPM mounting board for the first detector prototype.



(a)



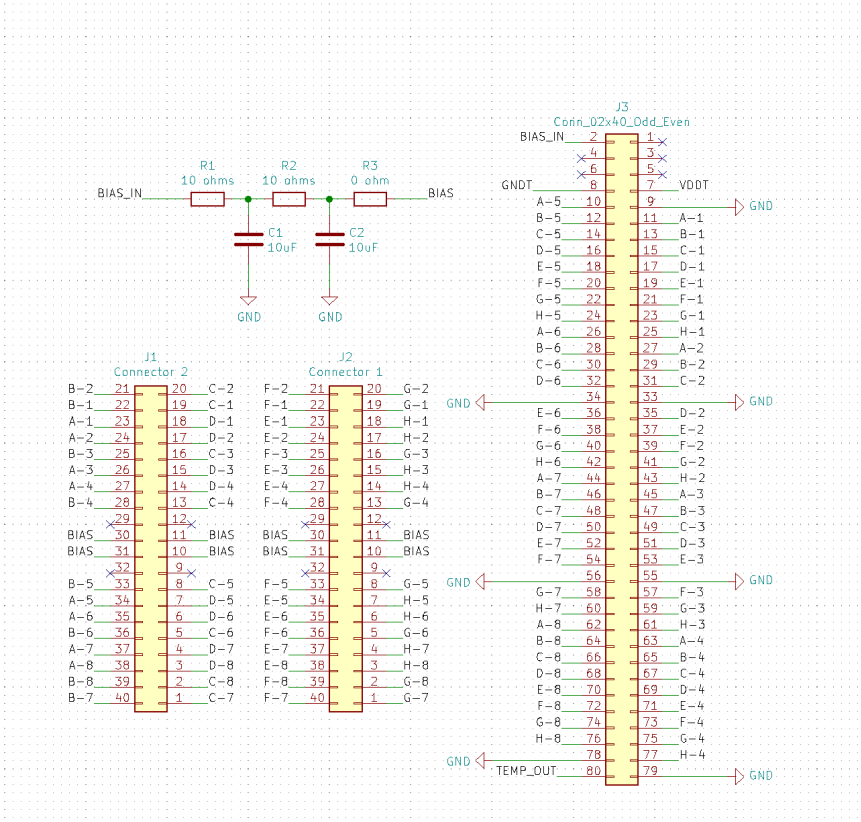
(b)

Figure A.2: (a) Front view and (b) back view of the SiPM mounting board generated using the KiCAD 3D viewer.

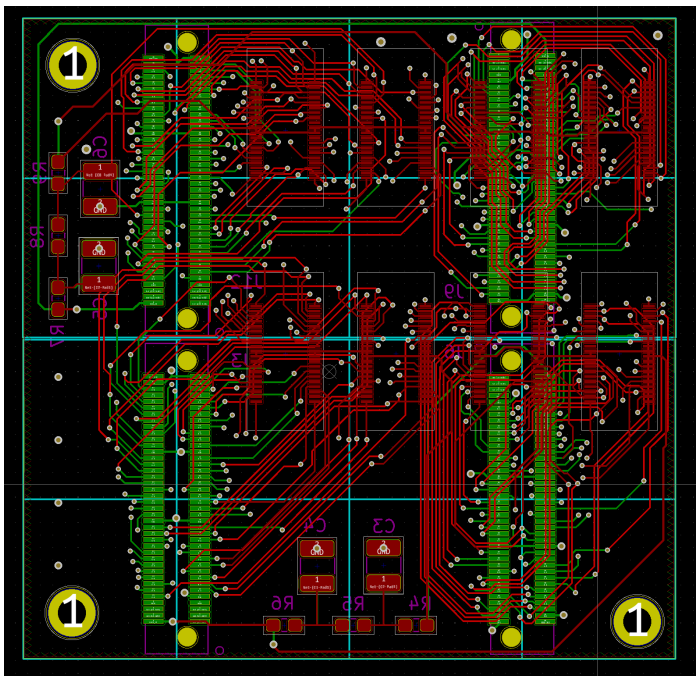
A.3 Custom FEB/S for Second Detector Prototype

Due to SiPM dimension mismatch, the existing FEB/S that comes with the readout system had to be replaced. Two versions of the custom FEB/S board were designed. The first version, which we called the "direct connection" version, allow the custom FEB/S board to be directly plugged into the headers of the FEB/A board. For the direct connection version, the custom FEB/S board does not fit within the area of the SiPM arrays. Hence it is not suitable for scaling up the system to larger than 16×16 system. The schematics and PCB layout of the direct connection version is shown in Figure A.3. As shown in Figure A.4, the custom FEB/S board is larger than the the area covered by the four SiPM arrays.

The second version, which we call the "ribbon connection" version, is designed by Justin Beal. This version, the custom FEB/S board fits directly under the SiPM arrays. This makes it suitable for scaling the detector system to any larger systems. However, because of the geometry constraint, this board cannot be plugged into the headers of the FEB/A board. Hence, ribbon cables are needed to make such connections. The schematics and PCB layout of the ribbon connection version is shown in Figure A.5. As shown in Figure A.6, the custom FEB/S board fits under the the area covered by the four SiPM arrays. This version of the board has not been tested.

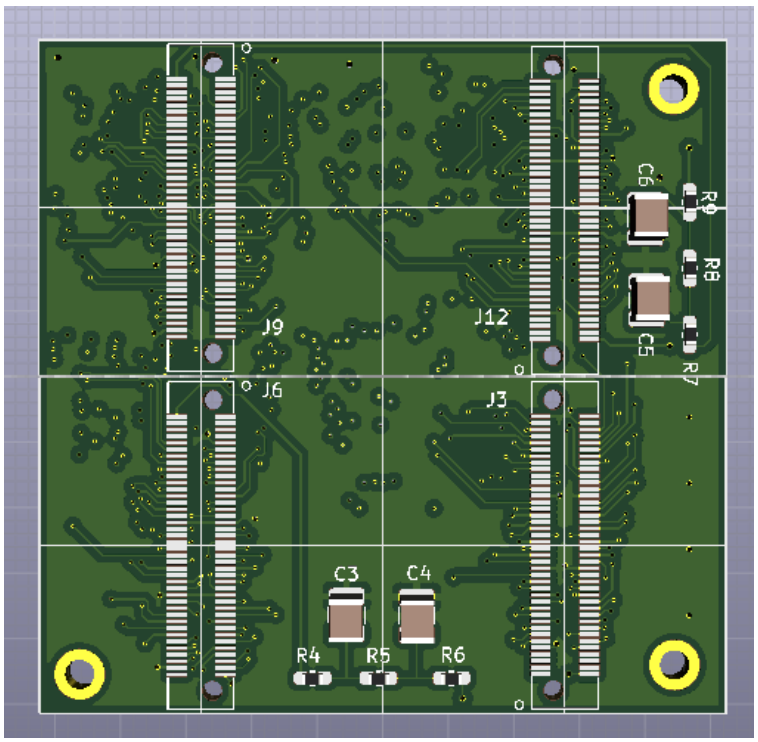


(a)

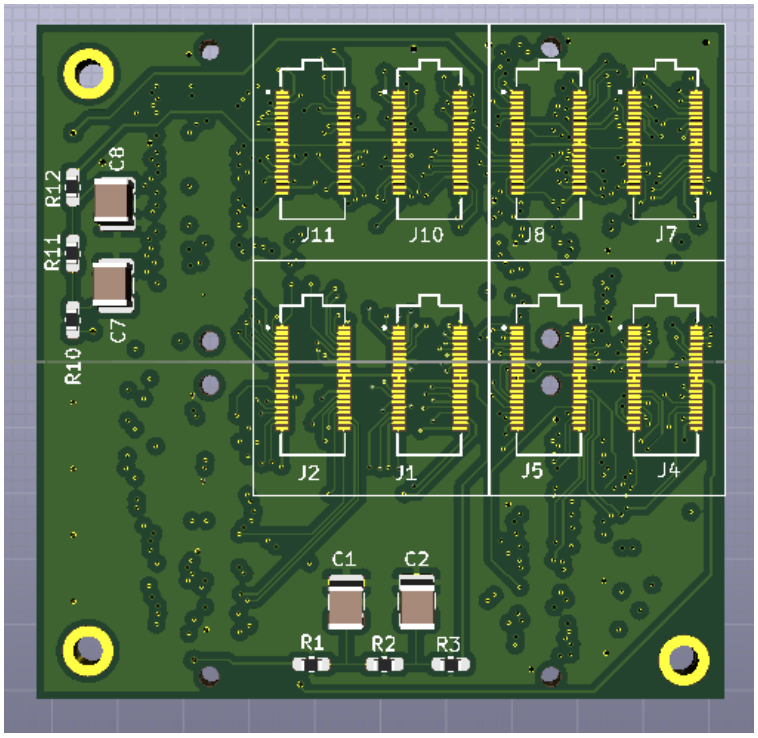


(b)

Figure A.3: Schematic and PCB layout of the custom FEB/S (direct connection) for the second detector prototype.

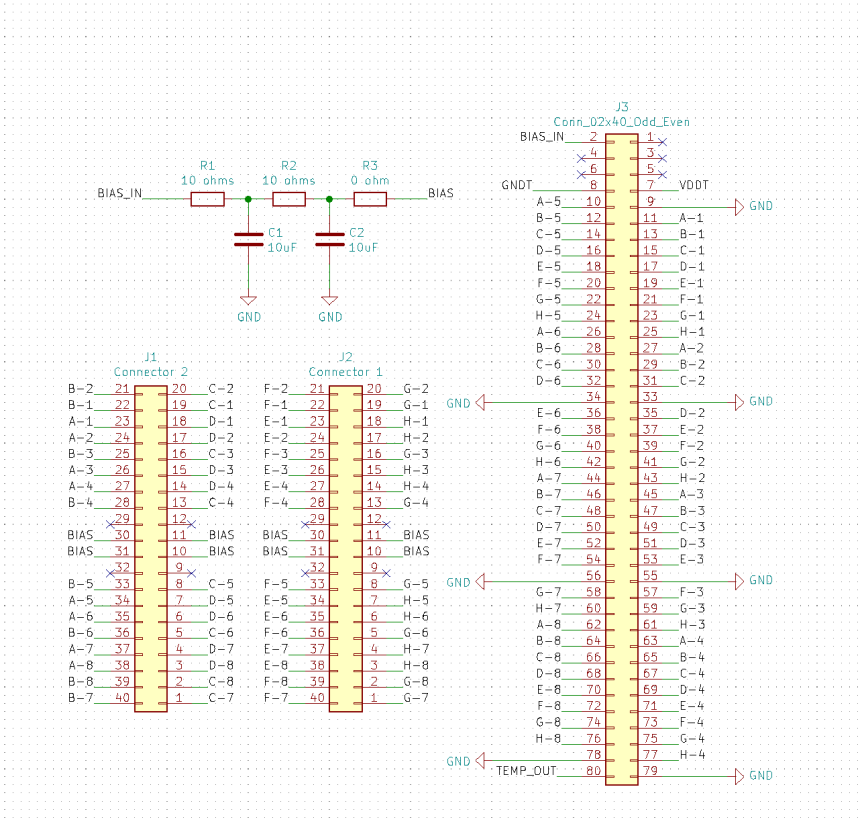


(a)

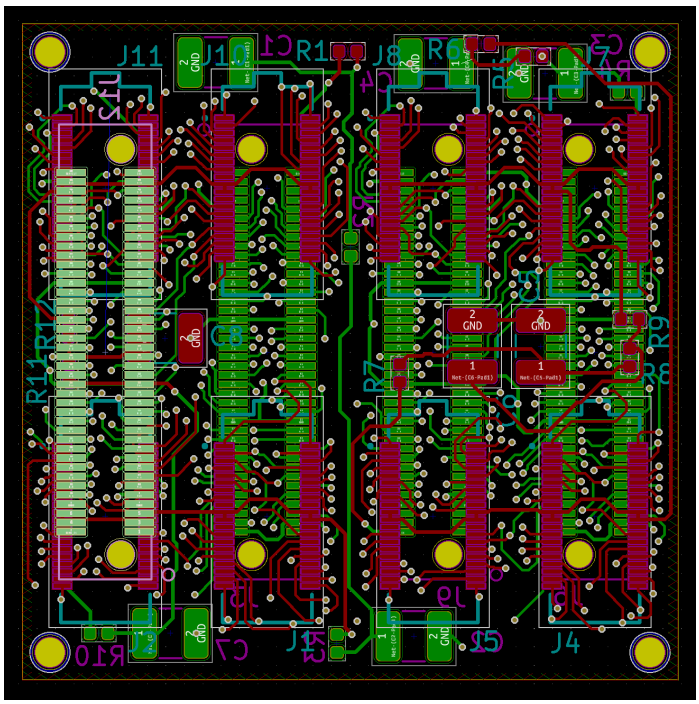


(b)

Figure A.4: Front view and back view of the custom FEB/S (direct connection) generated using the KiCAD 3D viewer.

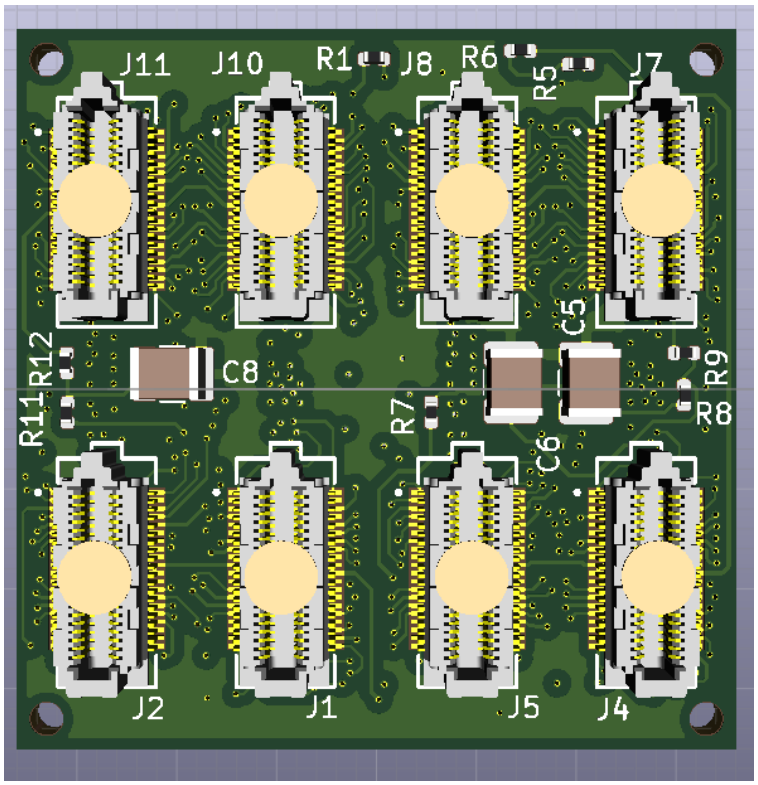


(a)

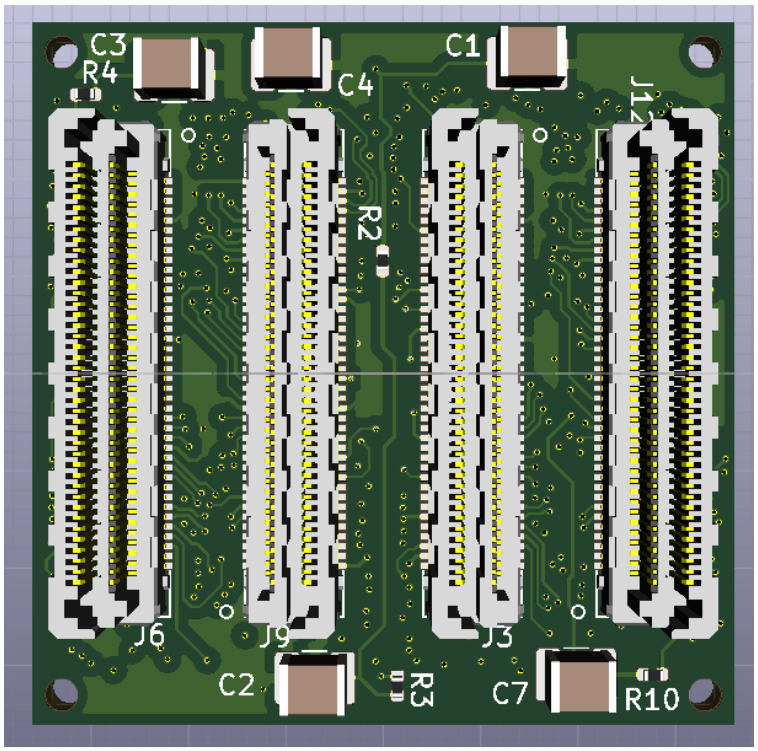


(b)

Figure A.5: Schematic and PCB layout of the custom FEB/S (ribbon connection) for the second detector prototype.



(a)



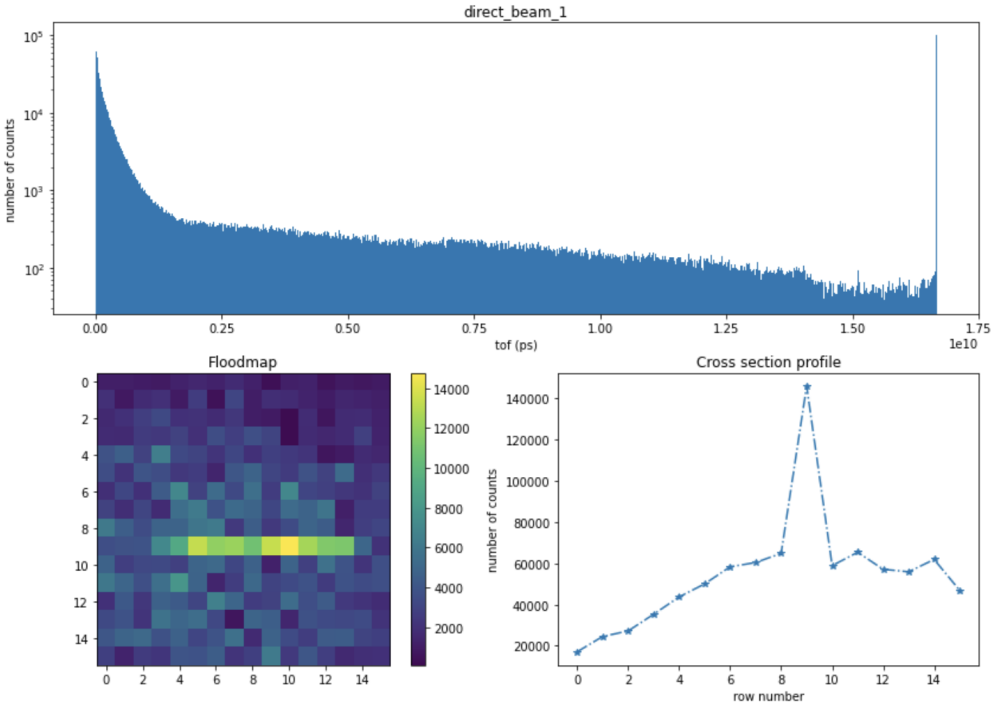
(b)

Figure A.6: Front view and back view of the custom FEB/S (ribbon connection) generated using the KiCAD 3D viewer.

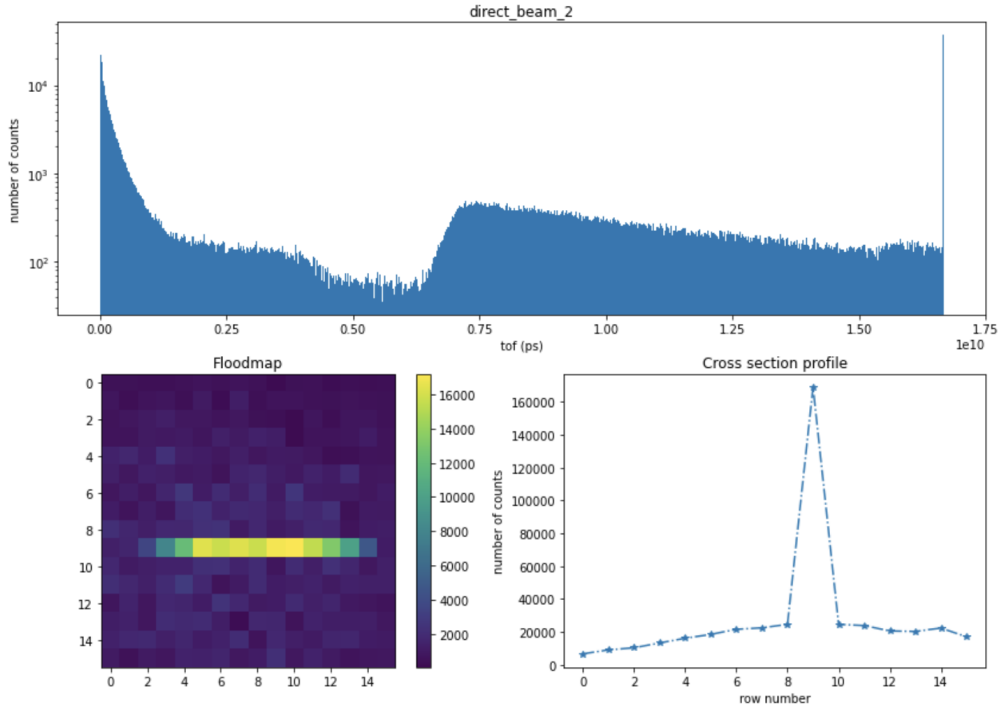
Appendix B

Time-of-Flight (ToF) Measurements from Reflectivity Experiment

The ToF spectrum, flood map and cross-sectional profile in count rate of the pixelated detector are shown. Figures B.1, B.2, B.3, and B.4 show the direct beam measurements using the 7 settings listed in Table 4.1. Figures B.5, B.6, B.7, and B.8 show the reflected beam measurements using the 7 settings listed in Table 4.2.

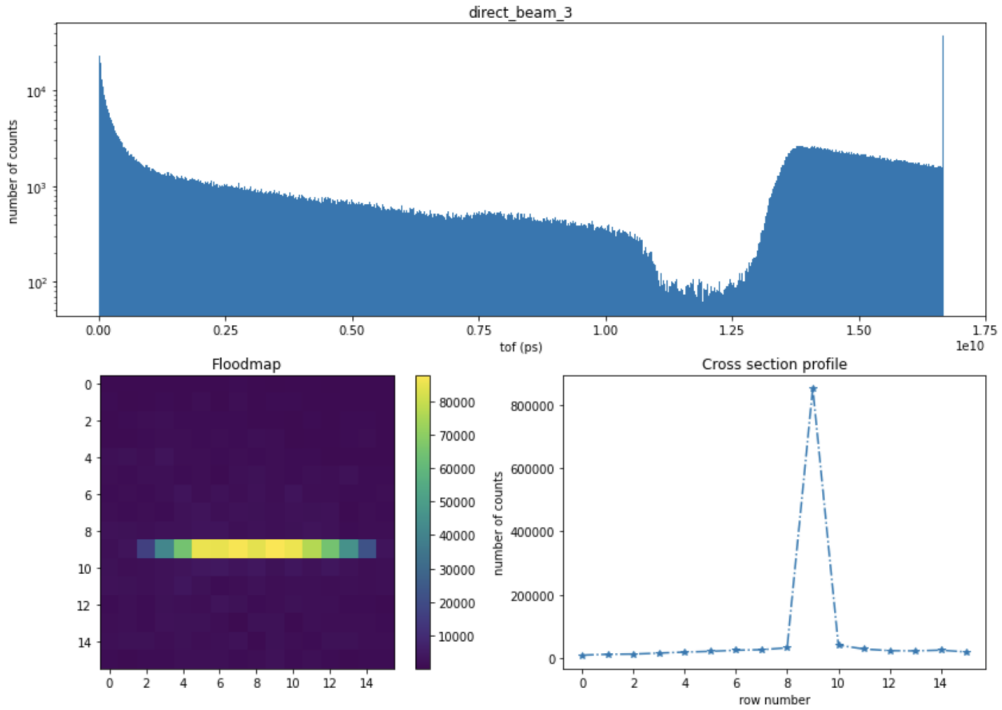


(a)

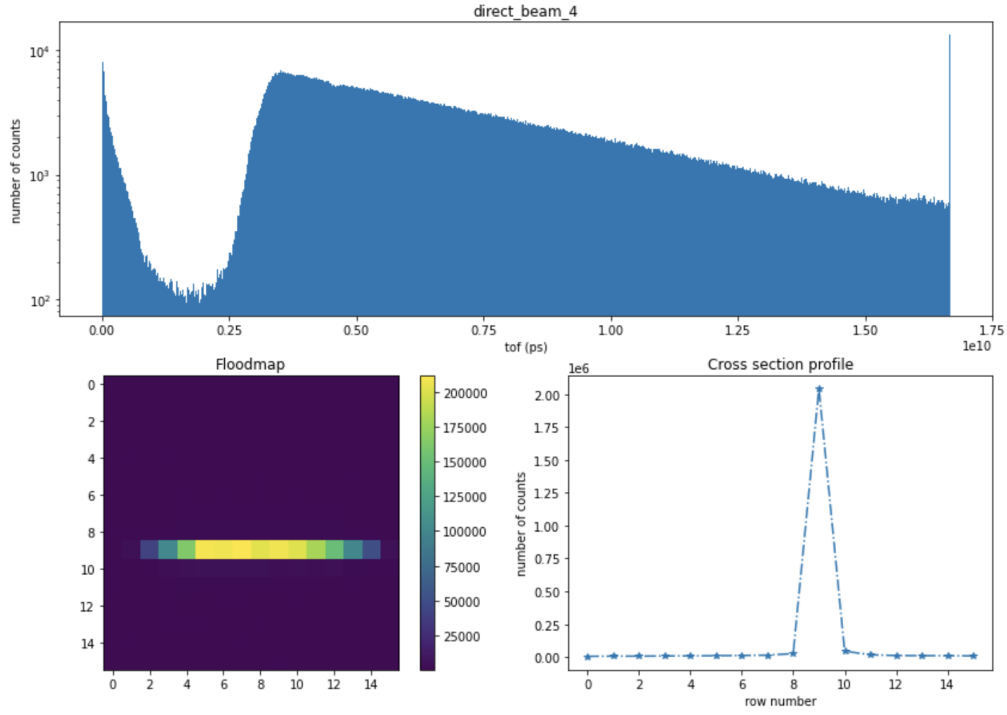


(b)

Figure B.1: Direct beam measurement: (a) run #1 and (b) run #2.

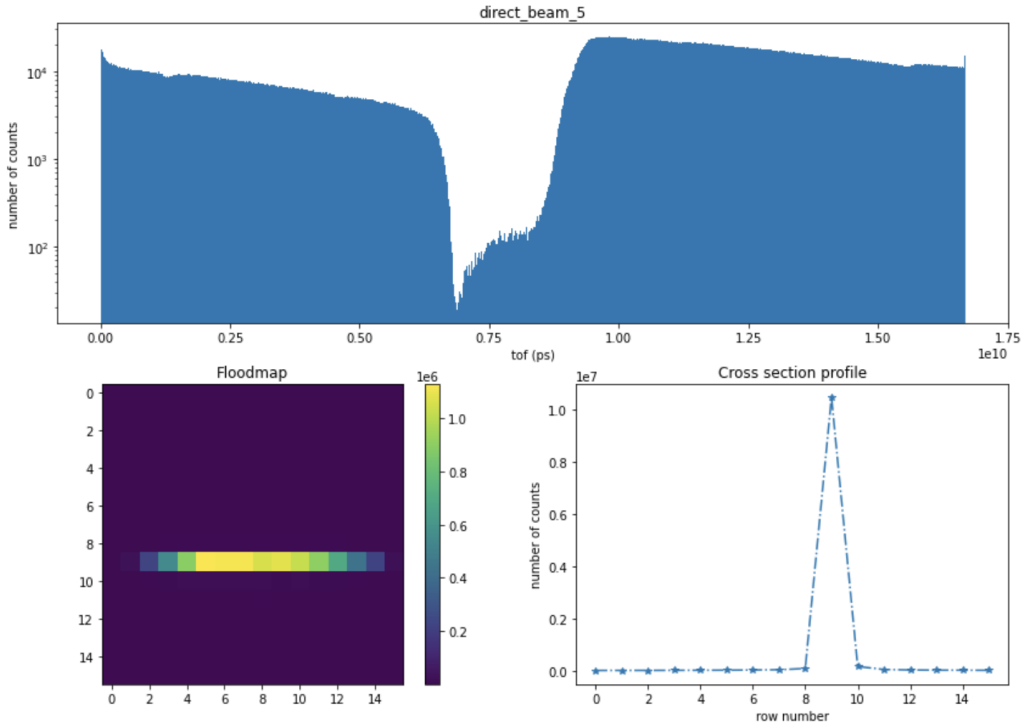


(a)

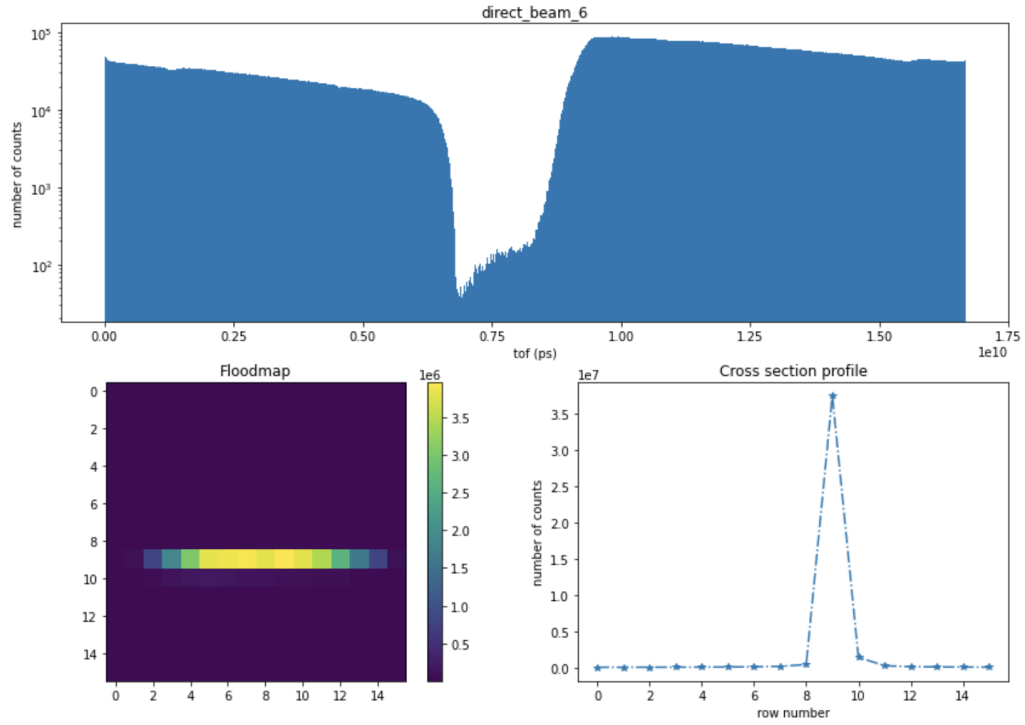


(b)

Figure B.2: Direct beam measurement: (a) run #3 and (b) run #4.



(a)



(b)

Figure B.3: Direct beam measurement: (a) run #5 and (b) run #6.

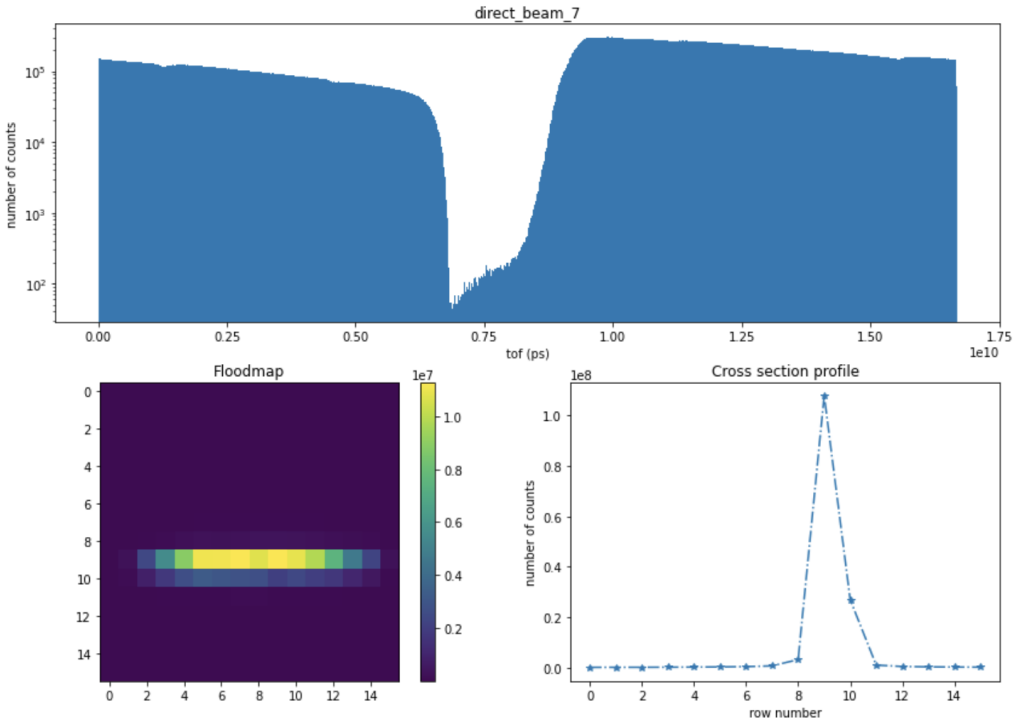
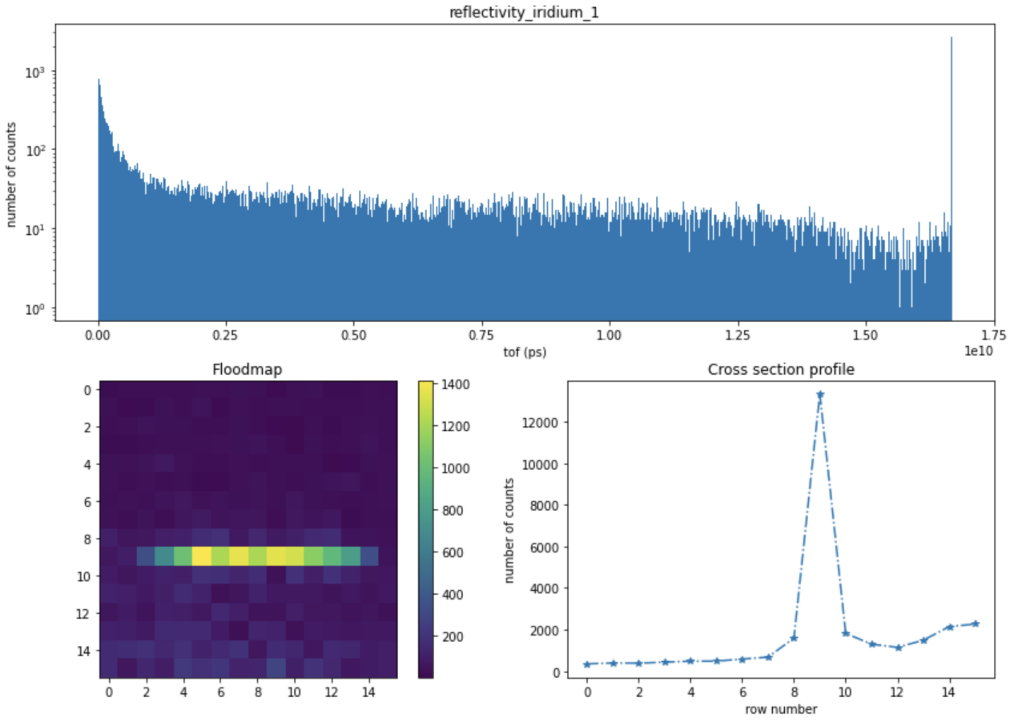
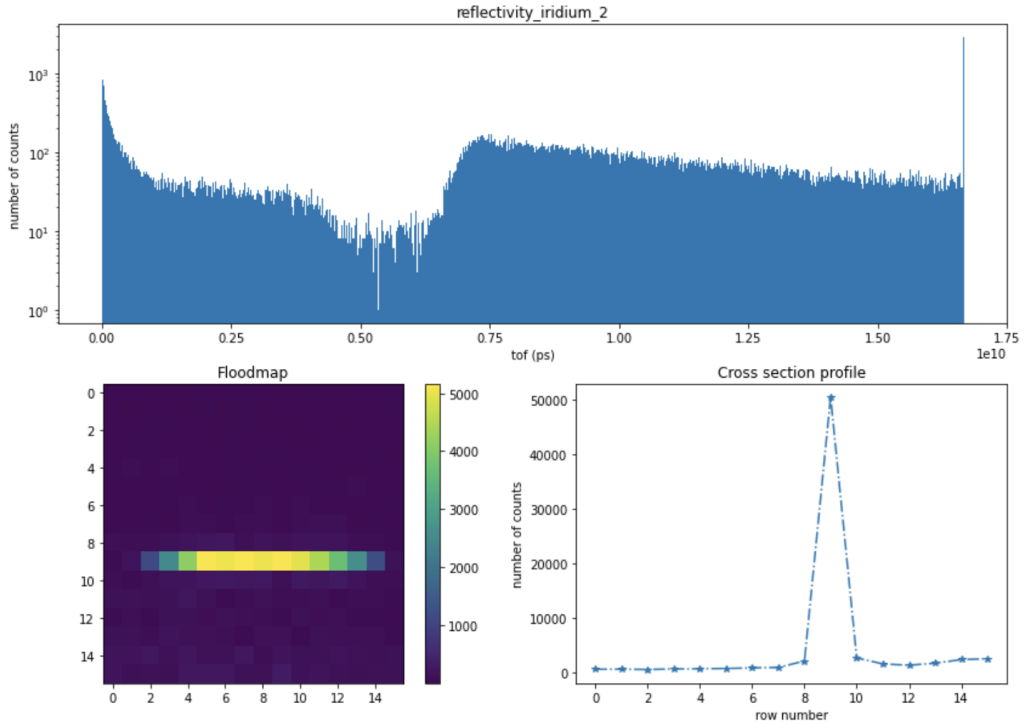


Figure B.4: Direct beam measurement: run #7.

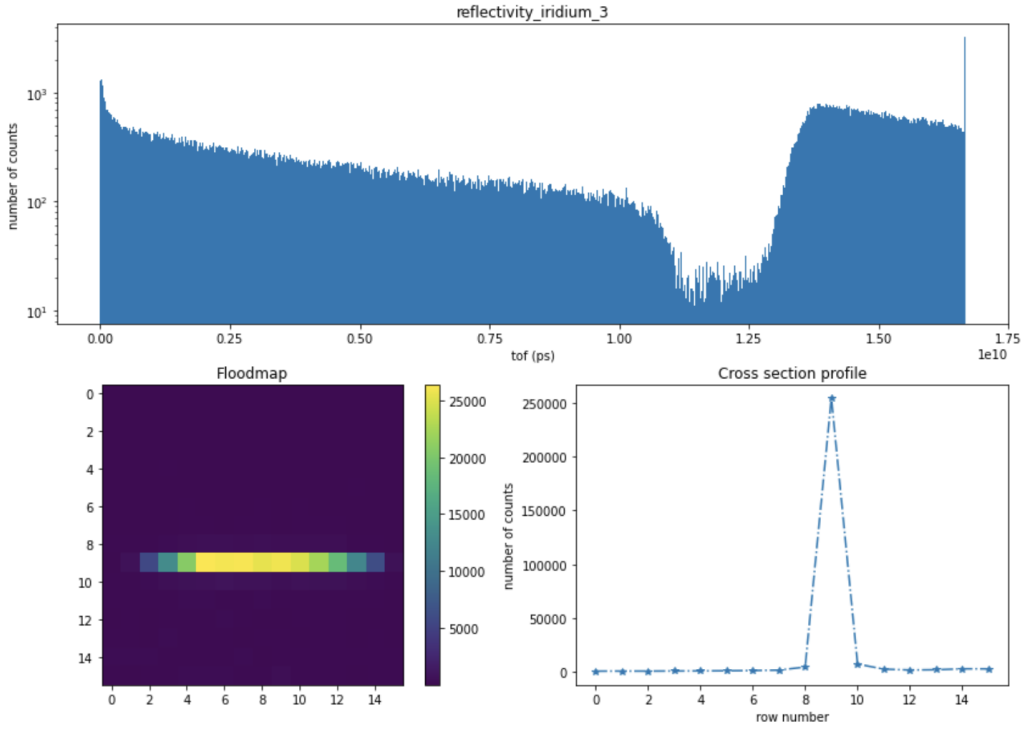


(a)

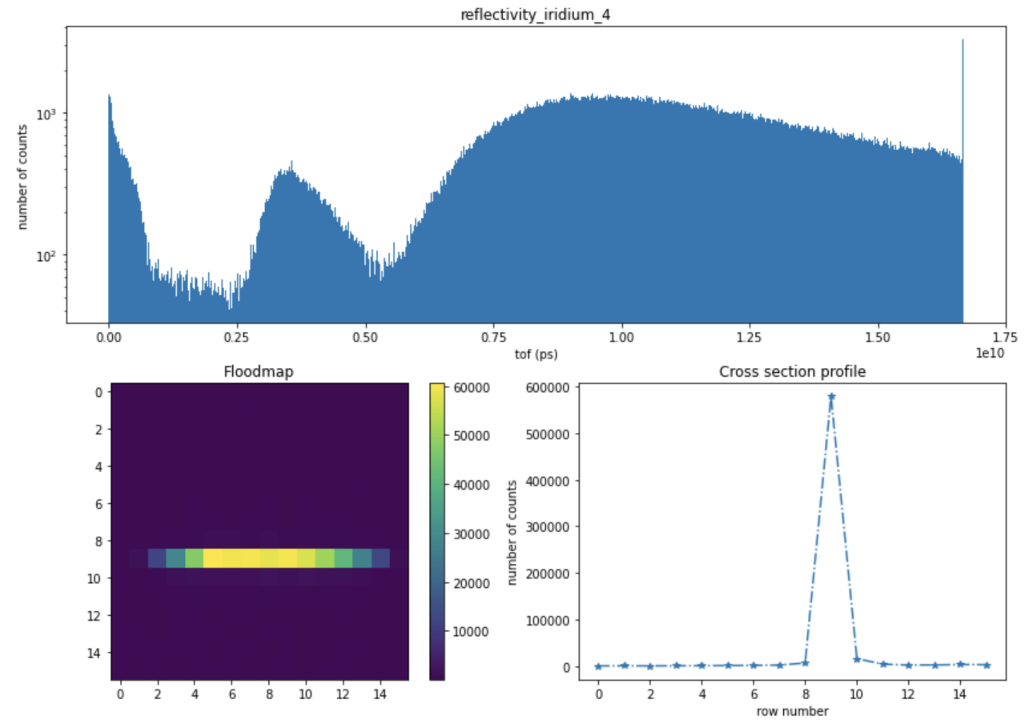


(b)

Figure B.5: Reflected beam measurement (iridium sample): (a) run #1 and (b) run #2.

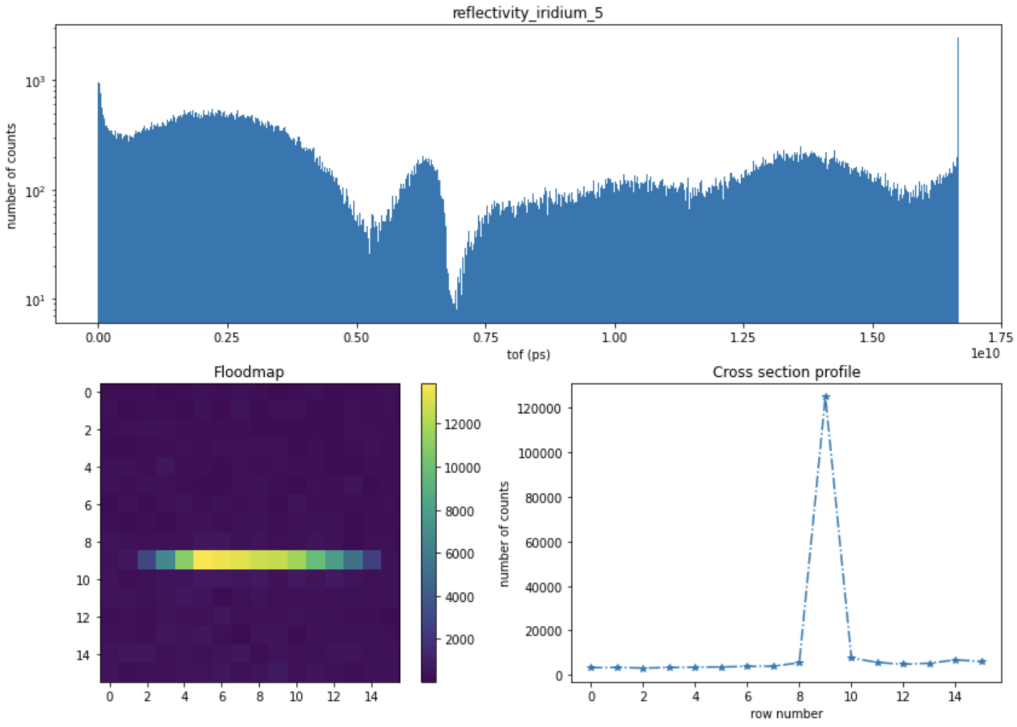


(a)

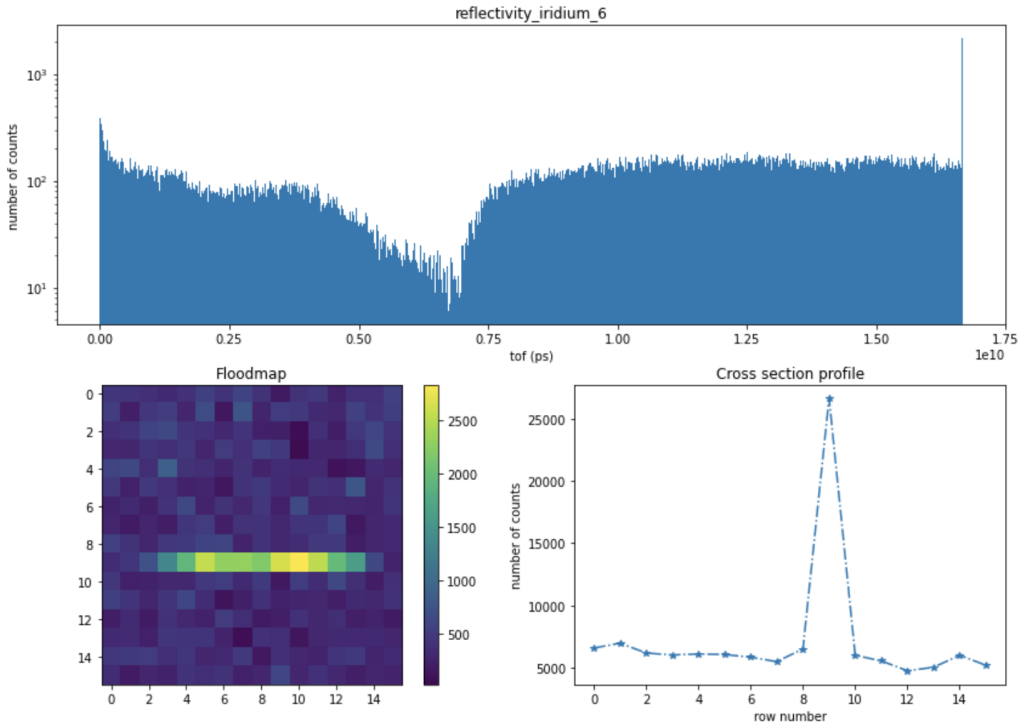


(b)

Figure B.6: Reflected beam measurement (iridium sample): (a) run #3 and (b) run #4.



(a)



(b)

Figure B.7: Reflected beam measurement (iridium sample): (a) run #5 and (b) run #6.

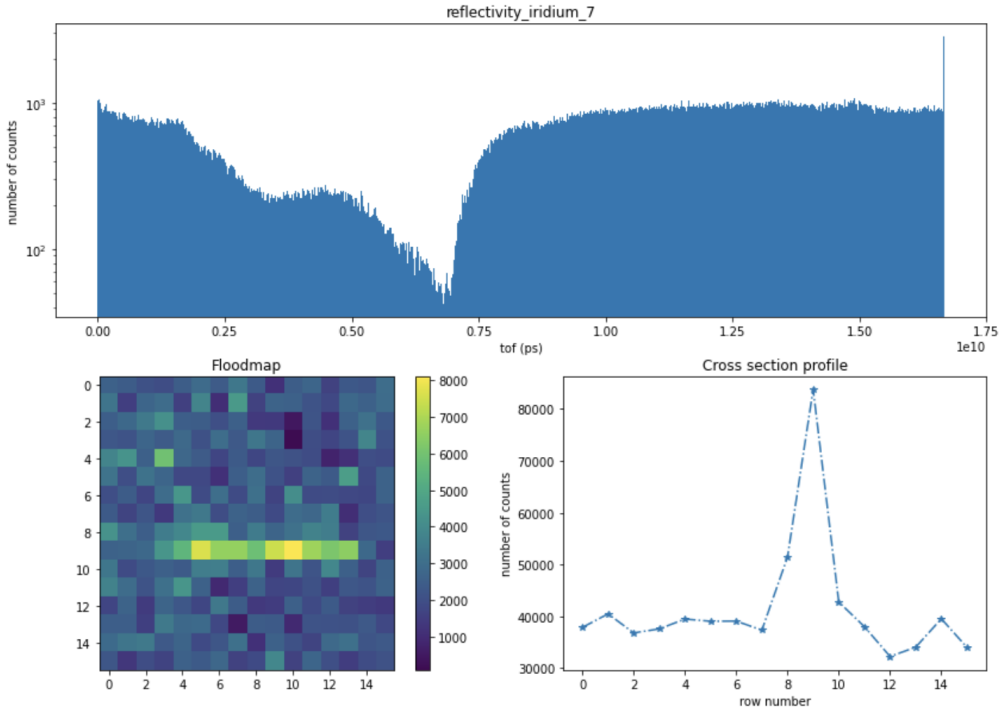


Figure B.8: Reflected beam measurement (iridium sample): run #7.

Vita

Su-Ann Chong was born in Penang, Malaysia. She moved to the United States to pursue her undergraduate studies. In 2016, she received her Bachelors of Art degree in Physics with a minor in Nuclear Engineering from University of California, Berkeley. During her time at Berkeley, she worked within the Bay Area Nuclear Data Group at the Lawrence Berkeley National Laboratory on a $^{35}C(n,p)^{35}S$ nuclear cross section measurement. The measurement of this work has a direct impact on the design of the molten chloride fast-spectrum advanced reactor. In 2017, she started her Ph.D. program in Nuclear Engineering at the University of Tennessee, Knoxville where she conducted her research work within the Detector Development Group at the Spallation Neutron Source, Oak Ridge National Laboratory. She spent her time at Oak Ridge developing a pixelated neutron detector for neutron reflectometry instruments. Her contribution in detector development is important in addressing the limitation in rate capability in existing detector technologies for current and upcoming spallation neutron sources. During her doctorate pursuit, she also earned a Master of Science in Computer Engineering from the University of Tennessee, Knoxville. She is expected to receive her Ph.D. in Nuclear Engineering in 2022.